DISSERTATION

APPLICATIONS OF ADVANCED SELF-CONSISTENT FIELD CALCULATIONS IN NANOSTRUCTURED POLYMERIC SYSTEMS

Submitted by

Dong Meng

Department of Chemical and Biological Engineering

In partial fulfillment of the requirements

For the Degree of Doctor of Philosophy

Colorado State University

Fort Collins, Colorado

Fall 2009

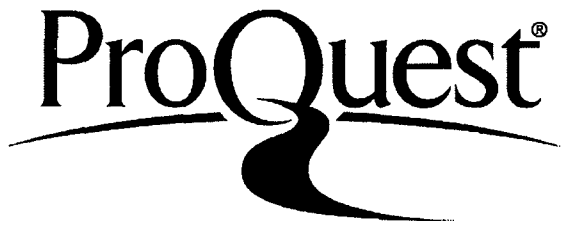

ProQuest LLC
789 East Eisenhower Parkway
P.O. Box 1346
Ann Arbor, MI 48106-1346

COLORADO STATE UNIVERSITY

October 8, 2009

WE HEREBY RECOMMEND THAT THE DISSERTATION PREPARED UNDER OUR SUPERVISION BY DONG MENG ENTITLED APPLICATIONS OF ADVANCED SELF-CONSISTENT FIELD CALCULATIONS IN NANOSTRUCTURED POLYMERIC SYSTEMS BE ACCEPTED AS FULFILLING IN PART REQUIREMENTS FOR THE DEGREE OF DOCTOR OF PHILOSOPHY.

Committee on Graduate Work

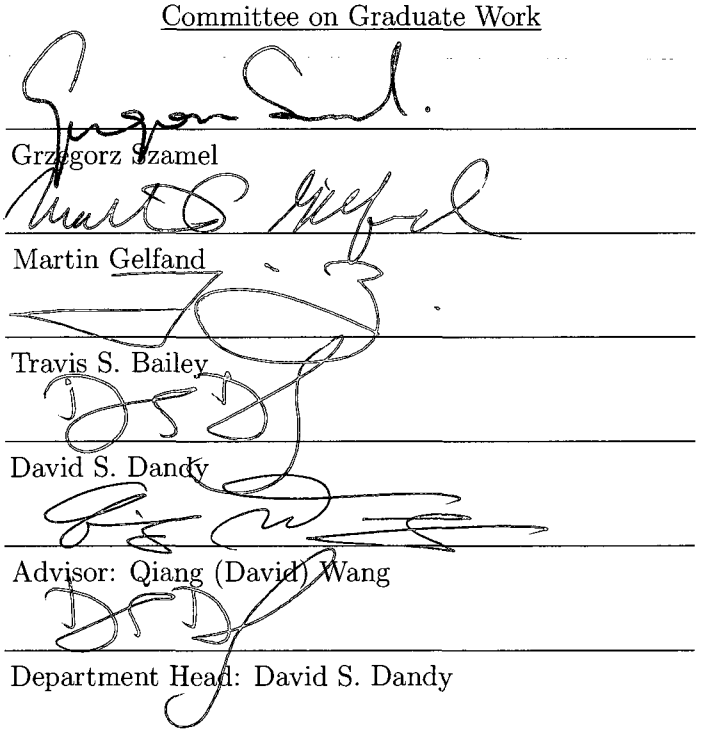

Grzegorz Szamel

Martin Gelfand

Travis S. Bailey

David S. Dandy

Advisor: Qiang (David) Wang

Department Head: David S. Dandy

ABSTRACT OF DISSERTATION

APPLICATIONS OF ADVANCED SELF-CONSISTENT FIELD CALCULATION IN NANOSTRUCTURED POLYMERIC SYSTEMS

The polymer self-consistent field (SCF) theory have gained great success in many systems, especially for the study of inhomogeneous nanostructured polymers. During my PhD study, I have applied real-space SCF calculations with high accuracy to mainly two categories of nanostructured polymers: The first part of this dissertation is focused on the study of self-assembled nanostructures of diblock copolymers (DBC) under nano-confinement. We first examined in detail the so-called "hard-surface" effects, originated from the impenetrable confining surfaces, on the phase behavior of confined DBC systems, where improving the numerical performance of SCF calculations with such effects is also discussed. We then studied in detail the self-assembled morphology of symmetric DBC confined between two homogeneous planner surfaces, where the effects of surface preference and film thickness are investigated and novel complex morphologies are found. Finally, we considered the directed assembly of DBC on topologically and chemically nano-patterned substrates, where well-ordered complex nanostructures can be obtained by controlling the substrate pattern.

In the second part of the dissertation, stimuli-response of polymer brushes (chains end-grafted onto a flat substrate) is investigated. We first studied the thermal response of poly-NIPAM brushes in water, and found that the

temperature where the largest thermal response occurs is governed by the chain-grafting density, while the magnitude of the thermal response is controlled by the polymer chain length. We then studied the solvent-response of uncharged DBC brushes and found that the copolymer composition is the key factor in switching the brush surface-layer composition by different solvent treatments; our SCF results agree well with available experimental measurements. Finally, we investigated the stimuli-response of charged DBC. Given the vast parameter space encountered here, we conducted our study based on the uncharged DBC brushes and explored the effects of charge fraction on polymer chains, solution pH and ionic strength, and applied electric fields on the brush surface-switching; this work reveals the complex interplay between different stimuli in such systems.

A list of all my published papers and manuscripts in preparation for publication is included at the end of this dissertation, where all the details of my SCF calculations can be found.

Dong Meng
Department of Chemical and Biological Engineering
Colorado State university
Fort Collins, CO 80523
Fall 2009

CONTENTS

LIST OF FIGURES

1. PREFACE

The study of polymeric systems has been among the most attractive research areas ever since polymers were first discovered. The interest in these systems arises not only in an effort to unveil the fundamentals, but also due to their wide range of technological applications. With significant advances in synthesis and characterization of polymers, the venerable polymer science has been constantly rejuvenated with new findings and innovative applications.

More recently, the study of block copolymers that undergo "micro-phase separation" to self-assemble into ordered structures[1–4] has received great attention. These self-assembled structures are usually on the length scale of tens of nanometers and thus have many useful and desirable properties. The potential applications of such polymeric systems span almost all industrial sectors, from semiconductor, pharmaceutical, energy to food industry. For example, nanostructures formed in block copolymer thin films can be used in semiconductor industry as nanolithographic masks to produce nanowires, high-density storage media, photonic band gaps, quantum dot or anti-dot arrays, to name a few. Surfaces coated or grafted with block copolymers can also change their properties in response to subtle changes in the environment, making such surfaces ideal for chemical sensors, self-cleaning materials, drug delivery carriers, protein-resistent surfaces, etc.

All these applications are centered around the nanostructures formed by block copolymers; fundamental understanding of the underlying physics that controls these self-assembled morphologies is therefore of critical importance. For this we resort to theory. There have been enormous efforts in developing theoretical and computational tools to model polymer systems. Most of them are "particle-based" models, either "atomistic" or "mesoscopic". The fundamental degrees of freedom in this type of models are particle positions and momenta, and as a result for systems of larger scales particle-based models become computationally very expensive. Not until the well celebrated work by Edwards,[5,6] an alternative, "field-based" model emerged and quickly became the common ground for modern polymer theories. In this statistical field theory, the fundamental degrees of freedom are no longer the particle positions and momenta, but rather one or more continuous field functions that vary with position.

There are a number of advantages using this field-based approach for studying polymer systems, especially for inhomogeneous systems. First of all, there is the flexibility of working with a field theory that originated from an atomic or a mesoscopic perspective. In addition, there is the flexibility in how the fields are represented and discretized, which leverages the large body of knowledge surrounding the numerical solution of partial differential equations. More importantly, the possibility of less field than particle degrees of freedom makes the field-based approach computationally advantageous, which translates into the possibility of working with systems at large length scales, for example, to simulate a block copolymer mesophase with domain features on hundreds of

nanometers.

Because of these important features and their inherent relevance to the study of nanostructured polymeric systems, the statistical field theory approach has since become the common foundation of many modern polymer theories. Among them the self-consistent field theory (SCFT) has demonstrated great success. SCFT is obtained by assuming that there is a single dominating field configuration that determines the properties of a system, known as the "mean-field" or "self-consistent field" approximation. SCFT avoids many approximations employed in other analytical field-based theories, and its "mean-field approximation" is well justified for concentrated polymer solutions and melts apart from the critical point. A nice example demonstrating the success of SCFT in describing inhomogeneous polymeric systems is the work done by Matsen in 1994,[7] where all the self-assembled morphologies of diblock copolymer melts observed in experiments were predicted in the correct sequence.

This work makes use of the success of the SCF calculations in the study of polymeric systems, and extend its applications to two systems that are of more practical interests, i.e., diblock copolymer under nano-confinement and stimuli responses of polymer brushes.

In the first part of the dissertation, we focus on the study of diblock copolymer under nano-confinement. We first examined in detail the so-called "hard-surface" effects, originated from the impenetrable confining surfaces, on the phase behavior of confined DBC systems, where improving the numerical performance of SCF calculations with such effects is also discussed. We then studied in

detail the self-assembled morphology of symmetric DBC confined between two homogeneous planer surfaces, where the effects of surface preference and film thickness are investigated and novel complex morphologies are found. Finally, we considered the directed assembly of DBC on topologically and chemically nano-patterned substrates, where well-ordered complex nanostructures can be obtained by controlling the substrate pattern.

In the second part of the dissertation, stimuli-response of polymer brushes (chains end-grafted onto a flat substrate) is investigated. We first studied the thermal response of poly-NIPAM brushes in water, and found that the temperature where the largest thermal response occurs is governed by the chain-grafting density, while the magnitude of the thermal response is controlled by the polymer chain length. We then studied the solvent-response of uncharged DBC brushes and found that the copolymer composition is the key factor in switching the brush surface-layer composition by different solvent treatments; our SCF results agree well with available experimental measurements. Finally, we investigated the stimuli-response of charged DBC. Given the vast parameter space encountered here, we conducted our study based on the uncharged DBC brushes and explored the effects of charge fraction on polymer chains, solution pH and ionic strength, and applied electric fields on the brush surface-switching; this work reveals the complex interplay between different stimuli in such systems.

BIBLIOGRAPHY

[1] F. S. Bates, and G.H. Fredrickson, Annu. Rev. Phys. Chem., **41**, 525 (1990)

[2] M.D. Whitmore and J.D. Vavasour, Acta Polymer., **46**, 341 (1995)

[3] M.W. Matsen and F.S. Bates, Macromolecules, **29**, 1091 (1996)

[4] K. Binder and M. Muller, Curr. Opin. Colloid Interf. Sci., **5**, 315 (2000)

[5] E. Helfand, Macromolecules, **8**, 552 (1975)

[6] E. Helfand and Z.R. Wasserman, Macromolecules, **9**, 879 (1976)

[7] M.W. Matsen and M. Schick, Phys. Rev. Lett., **72**, 2660 (1994)

Part I

DIBLOCK COPOLYMER UNDER NANO-CONFINEMENT

2. HARD-SURFACE EFFECTS IN POLYMER SELF-CONSISTENT FIELD CALCULATIONS

2.1 Introduction

Proposed over 40 years ago,[1] the self-consistent field (SCF) theory has been widely applied to various polymeric systems with great success, including the interface of polymer blends,[2–9] microphase separation of block copolymers,[10–12] polymers near surfaces,[13,14] etc. Advanced numerical methods[15–18] and parallelization[19] enable SCF calculations with high accuracy, providing a mature and powerful computational tool for the study of equilibrium behavior of polymeric systems at nano- to meso-scales. When applied to confined systems by impenetrable (hard) surfaces, however, SCF calculations encounter some numerical problems that have not been examined closely. To adequately represent the hard-surface confinement, the polymer density must vanish at the surface must vanish, requiring the once-integrated propagator $q(\mathbf{r}, s)$ be 0 there for all s (a variable denoting the segmental position along the chain contour). According to the modified diffusion equation $\partial q/\partial s = \nabla^2 q - \omega(\mathbf{r})q$, this leads to a diverging conjugate field $\omega(\mathbf{r})$ unless $\nabla^2 q$ is 0 for all s at the surface. Such a diverging ω-field may cause some numerical problems, not only in solving the SCF equations, but also in calculating the system free energy.

On the other hand, a vanishing polymer density at the surface is incompatible with the usually enforced incompressibility of total (normalized) polymer segmental density having a value of 1 inside the confined system (polymer melts). A common way to circumvent this is to replace unity in the incompressibility constraint by a function $\phi_0(\mathbf{r})$ that continuously vary from 0 to 1 over a short distance from the surface (the surface layer). The choice of $\phi_0(\mathbf{r})$ in the surface layer, however, has been arbitrary. While Matsen used a cosine-shaped profile,[20] Chen and Fredrickson adopted a linear profile;[21] Li et al. used a "step-function" profile,[22] which can be considered as a linear profile due to the spatial domain discretization. Because of the continuous Gaussian chain model commonly used in SCF theory, it cannot capture the polymer density oscillations near an impenetrable surface (which is due to the chain packing effects) as revealed, for example, by Monte Carlo simulations.[23] The choice of $\phi_0(\mathbf{r})$ should therefore be based on the numerical performance of SCF calculations, i.e., to make the calculations converge rapidly with refined discretization. Although it has been claimed that the detailed shape of $\phi_0(\mathbf{r})$ in the surface layer has little consequence, our results show that this is not the case in terms of the numerical performance of SCF calculations, as demonstrated with a model system of confined homopolymer melts in Sec. 2.3.

In addition to the above numerical problems, hard-surface confinement as modeled in SCF calculations influences the system in two different but related aspects: the decrease of polymer density near the surface and the change of chain conformations from the bulk counterparts (where $\phi_0(\mathbf{r}) = 1$); the latter is manifested by chain-end enrichment and middle-segment depletion near the surface. For the self-assembly of block copolymers under nano-confinement,

which has attracted great interest in recent years due to its potential applications in nanotechnology,[24–26] these influences correspond to energetic and entropic effects, respectively. The former has been referred to as the "surface-induced compatibilization" between different types of polymer segments, and considered as the dominant factor responsible for the interesting phenomenon that, when the film thickness is commensurate with the bulk lamellar period, perpendicular lamellae are more stable than parallel lamellae in thin films of symmetric diblock copolymers confined between two neutral surfaces.[20,23,27] Our results in Sec. 2.4 show, however, that the entropic effects are comparable in magnitude to this energetic effect and cannot be overlooked. In fact, Monte Carlo simulations have revealed that chain ends enrich near a hard surface and that diblock copolymer chains close to the surface orient parallel to it.[28,29] In the case of asymmetric diblock copolymer thin films, one of us further proposed that a neutral surface exhibits an entropic preference for the shorter block due to chain-end enrichment.[30]

From a theoretical point of view, it is of fundamental interest in polymer science to understand how an impenetrable surface affects the behavior of polymers near it. In this work, we present the first systematic study on the hard-surface effects in SCF calculations. Our models and numerical methods are summarized in Sec. 2.2. In Sec. 2.3 we identify two profiles of $\phi_0(\mathbf{r})$ in the surface layer that are suitable for high-accuracy SCF calculations of confined polymer melts. We then in Sec. 2.4 investigate both the energetic and entropic effects of hard-surface confinement on symmetric diblock copolymer thin films. These effects for cylinder-forming asymmetric diblock copolymer thin films are further examined in Sec. 2.5. The last Section is devoted to conclusions.

2.2 Models and Numerical Methods

Since the polymer self-consistent field (SCF) theory has been well developed, we only summarize our SCF equations and numerical methods here; readers are referred to, e.g., Ref. [31] for detailed derivation and explanation of this theory.

2.2.1 Confined Homopolymer Melts

The simplest case is to confine homopolymers A with a length N_A to a one-dimensional polymer segmental density (normalized by the density of polymer segments) profile $\phi_0(x)$, where $x \in [0, d]$ and $\phi_0(x = 0) = \phi_0(x = d) = 0$. The corresponding SCF equations are

$$\frac{\partial q}{\partial s} = \frac{\partial^2 q}{\partial x^2} - \eta(x) q \tag{2.1}$$

$$\phi_0(x) = \frac{\bar{\phi}_0 N}{Q N_A} \int_0^{\frac{N_A}{N}} \mathrm{d}s q(x, s) q(x, \frac{N_A}{N} - s) \tag{2.2}$$

Here $q(x, s)$ corresponds to the probability of finding the end-segment of a polymer chain of length sN at x, and $s \in [0, N_A/N]$ denotes a position along the chain contour. $\eta(x)$ is the (purely imaginary) pressure field enforcing the confinement, Eq. (2.2); note that $\eta(x)$ can be shifted by an arbitrary constant. The boundary conditions for the modified diffusion equation, Eq. (2.1), are $q(x = 0, s) = q(x = d, s) = 0$ for all s, and its initial condition is $q(x, s = 0) = 1$ for $0 < x < d$. In Eq. (2.2), $\bar{\phi}_0 \equiv \int_0^d \mathrm{d}x \phi_0(x)/d$, and the single-chain partition function $Q \equiv \int_0^d \mathrm{d}x q(x, N_A/N)/d$. Note that x is in units of the radius of gyration of a Gaussian chain of N segments, $R_g \equiv a\sqrt{N/6}$, where a denotes the statistical segmental length; for finite N_A, we set $N = N_A$ hereafter. Once the SCF equations are solved, the mean-field free energy per polymer segment is give

by

$$F_s = -\frac{1}{N}\left[\frac{1}{\bar{\phi}_0 d}\int_0^d \mathrm{d}x\eta(x)\phi_0(x) + \ln\bar{\phi}_0\right] \tag{2.3}$$

where we set $Q = \bar{\phi}_0$ to fix $\eta(x)$ during the solution.

To solve $\eta(x)$ for a given $\phi_0(x)$, we invoke the ground-state dominance approximation (GSDA), which gives $q(x,s) = \exp(-\eta_0 s)q_0(x)$ for $N_\mathrm{A} \to \infty$, where η_0 is the smallest eigenvalue of the operator $-\frac{\partial^2}{\partial x^2} + \eta(x)$, and $q_0(x)$ is the corresponding eigenfunction. Substituting it into the SCF equations, we obtain

$$\eta^{\mathrm{GSDA}}(x) = \frac{\phi_0''}{2\phi_0(x)} - \left[\frac{\phi_0'}{2\phi_0(x)}\right]^2 \tag{2.4}$$

where ϕ_0' denotes $\mathrm{d}\phi_0(x)/\mathrm{d}x$, and so on. Note that a constant is ignored in Eq. (2.4). As shown below, this relation can help us understand the behavior of $\eta(x)$ obtained by numerically solving the SCF equations.

To ensure the high accuracy of our numerical results, we use the newly proposed fourth-order implicit-explicit scheme[17] to solve the modified diffusion equations. The chain contour $[0,1]$ is uniformly discretized into n steps. To obtain the initial values for q required by this method, we use the second-order pseudo-spectral method[16] (instead of the first-order Euler method as proposed in Ref. [17]) combined with Richardson extrapolation.[32] In the x direction, we use fast sine transforms, consistent with the boundary conditions of the modified diffusion equation. The SCF equations are solved in real space by the Broyden method combined with a globally convergent strategy.[33] The interval $[0,d]$ is uniformly discretized into m subintervals, and the absolute residual error of

Eq. (2.2) at any collocation point is less than 10^{-10} in our calculations. Finally, we evaluate all integrals using Romberg integration.[34]

2.2.2 Confined Diblock Copolymer Melts

Here we consider diblock copolymers A-B of chain length N confined between two flat and impenetrable surfaces placed at $x = 0$ and d. Assuming that all polymer segments have the same statistical segmental length a, we can write the SCF equations as

$$\omega_{\mathrm{A}}(\mathbf{r}) = \chi N \phi_{\mathrm{B}}(\mathbf{r}) - H(x) + \eta(\mathbf{r}) \tag{2.5}$$

$$\omega_{\mathrm{B}}(\mathbf{r}) = \chi N \phi_{\mathrm{A}}(\mathbf{r}) + H(x) + \eta(\mathbf{r}) \tag{2.6}$$

$$\phi_{\mathrm{A}}(\mathbf{r}) = \frac{\bar{\phi}_0}{Q} \int_0^{f_{\mathrm{A}}} \mathrm{d}s q(\mathbf{r}, s) q^*(\mathbf{r}, 1-s) \tag{2.7}$$

$$\phi_{\mathrm{B}}(\mathbf{r}) = \frac{\bar{\phi}_0}{Q} \int_{f_{\mathrm{A}}}^1 \mathrm{d}s q(\mathbf{r}, s) q^*(\mathbf{r}, 1-s) \tag{2.8}$$

$$\phi_{\mathrm{A}}(\mathbf{r}) + \phi_{\mathrm{B}}(\mathbf{r}) = \phi_0(x) \tag{2.9}$$

Here $\phi_{\mathrm{A}}(\mathbf{r})$ and $\phi_{\mathrm{B}}(\mathbf{r})$ are the density fields of A and B segments, respectively, and $\omega_{\mathrm{A}}(\mathbf{r})$ and $\omega_{\mathrm{B}}(\mathbf{r})$ are the conjugate fields interacting these species. $\eta(\mathbf{r})$ enforces incompressibility, Eq. (2.9) in this case. $H(x)$ is a field representing the energetic surface preference for the two blocks: it is positive when the surface prefers A segments and negative when the surface prefers B segments; in most cases we use two neutral surfaces and set $H(x) = 0$. We also use χ to denote the Flory-Huggins interaction parameter between A and B segments, f_{A} the volume fraction of A block in the copolymer, and $s \in [0, 1]$ the segmental position along the chain contour. For diblock copolymers, $q(\mathbf{r}, s)$ corresponds to the probability of finding a copolymer chain of length sN that starts from the A-end (where

$s = 0$) anywhere in the system and ends at position $\mathbf{r}$, and satisfies

$$\frac{\partial q}{\partial s} = \begin{cases} \nabla^2 q - \omega_A(\mathbf{r}) q & \text{for } 0 \le s \le f_A \\ \nabla^2 q - \omega_B(\mathbf{r}) q & \text{for } f_A \le s \le 1 \end{cases} \tag{2.10}$$

Similarly, $q^*(\mathbf{r}, t)$ with $t \equiv 1 - s$ corresponds to the probability of finding a copolymer chain of length tN that starts from the B-end (where $s = 1$) anywhere in the system and ends at $\mathbf{r}$, and satisfies

$$\frac{\partial q^*}{\partial t} = \begin{cases} \nabla^2 q^* - \omega_B(\mathbf{r}) q^* & \text{for } 0 \le t \le 1 - f_A \\ \nabla^2 q^* - \omega_A(\mathbf{r}) q^* & \text{for } 1 - f_A \le t \le 1 \end{cases} \tag{2.11}$$

Two sets of boundary and initial conditions for the modified diffusion equations, Eqs. (2.10) and (2.11), are used in our calculations. For cases where $\phi_0(x = 0) = \phi_0(x = d) = 0$, we usually (unless otherwise specified) apply the Dirichlet boundary conditions of $q(\mathbf{r}, s) = q^*(\mathbf{r}, s) = 0$ at $x = 0$ and d for all s, together with the initial conditions of $q(\mathbf{r}, s = 0) = q^*(\mathbf{r}, t = 0) = 1$ at $0 < x < d$; while for all other cases, we apply the Neumann boundary conditions of $\partial q(\mathbf{r}, s)/\partial x = \partial q^*(\mathbf{r}, s)/\partial x = 0$ at $x = 0$ and d for all s, together with the initial conditions of $q(\mathbf{r}, s = 0) = q^*(\mathbf{r}, t = 0) = 1$ at all $\mathbf{r}$. For multi-dimensional calculations, periodic boundary conditions are applied in the y and z directions. In Eqs. (7.4) and (7.5), $Q \equiv \int \mathrm{d}\mathbf{r} q(\mathbf{r}, 1)/V$ and $\bar{\phi}_0 \equiv \int_0^d \mathrm{d}x \phi_0(x)/d$, where $V = l_y l_z d$ denotes the system volume with l_y and l_z being the system size along the y and z directions, respectively. Again, we have normalized all the distance by $R_g \equiv a\sqrt{N/6}$.

Once the SCF equations are solved, the mean-field free energy per chain

of length N is calculated as

$$F = \frac{1}{\bar{\phi}_0 V} \int \mathrm{d}\mathbf{r} \chi N \phi_{\mathrm{A}}(\mathbf{r}) \phi_{\mathrm{B}}(\mathbf{r}) - \omega_{\mathrm{A}}(\mathbf{r}) \phi_{\mathrm{A}}(\mathbf{r}) - \omega_{\mathrm{B}}(\mathbf{r}) \phi_{\mathrm{B}}(\mathbf{r}) - H(x)[\phi_{\mathrm{A}}(\mathbf{r}) - \phi_{\mathrm{B}}(\mathbf{r})] - \ln Q \tag{2.12}$$

As before, we use the fourth-order implicit-explicit scheme[17] to solve the modified diffusion equations. The chain contour $[0, 1]$ is uniformly discretized into n steps, and the interval $[0, d]$ (in the x direction) is uniformly discretized into m subintervals. We use the fast sine transforms in the x direction when the Dirichlet boundary conditions are applied, and the fast cosine transforms when the Neumann boundary conditions are applied. For multi-dimensional calculations, the system sizes along the y and z directions are uniformly discretized into m_y and m_z subintervals, respectively, and we use the fast Fourier transforms in these directions. For one-dimensional calculations, the Broyden method is used to solve the SCF equations and the maximum residual error at all collocation points $\mathbf{r}$, $\epsilon \equiv \max\{|\frac{\omega_{\mathrm{A}}(\mathbf{r})-\omega_{\mathrm{B}}(\mathbf{r})}{2\chi N} + \frac{\phi_0(x)}{2} - \phi_{\mathrm{B}}(\mathbf{r})|, |\frac{\omega_{\mathrm{B}}(\mathbf{r})-\omega_{\mathrm{A}}(\mathbf{r})}{2\chi N} + \frac{\phi_0(x)}{2} - \phi_{\mathrm{A}}(\mathbf{r})|\}$, is less than 10^{-11}; while for multi-dimensional calculations, the semi-implicit scheme[18] is used to iterate the SCF equations until ϵ is less than 10^{-4}; here, for given $\omega_{\mathrm{A}}(\mathbf{r})$ and $\omega_{\mathrm{B}}(\mathbf{r})$, Eqs. (7.4) and (7.5) are used to calculate $\phi_{\mathrm{A}}(\mathbf{r})$ and $\phi_{\mathrm{B}}(\mathbf{r})$ after the modified diffusion equations are solved. Since the conjugate fields can be shifted by an arbitrary constant without changing the density fields and the system free energy, we set $Q = \bar{\phi}_0/3n$ to obtain a unique solution. Finally, we evaluate all integrals using Romberg integration[34] when possible; the composite Simpson's formula is used otherwise.

2.3 Confined Homopolymers

2.3.1 Choice of $\phi_0(\mathbf{x})$

In the interior of confined polymer melts it is natural to set the (normalized) polymer segmental density $\phi_0(x) = 1$, while close to the confining surfaces $\phi_0(x)$ continuously decreases from 1 to 0 over a short distance denoted by τ (surface layer). Thus our goal here is to identify a form of $\phi_0(x)$ in the surface layer, denoted by $\phi_{0,sl}(x)$ with $x \in [0, \tau]$, that leads to good numerical performance of SCF calculations (i.e., makes the calculations converge rapidly with increasing m and n); for this purpose, we consider $\phi_0(x)$ to be symmetric about $x = d/2$.

Most SCF calculations reported in the literature used a linear profile of $\phi_{0,sl}(x) = x/\tau$ (referred to as P1); this includes the "step-function" case (i.e., $\phi_{0,sl}(x = 0) = 0$ and $\phi_{0,sl}(x > 0) = 1$)[22,35] due to the discretization in the x direction. Fig. 2.1 shows the obtained pressure field $\eta(x)$ for this P1 profile, where $d = 3.2$ and $\tau = 0.1$ are used with different values of m. Our calculation with $m = 32$ corresponds to the "step-function" case, while that with $m = 64$ corresponds to the profile used in Refs. [21, 36, 37]. Although these two cases are numerically well behaved, P1 is not a good choice in that further refinement with larger m quickly leads to large, problematic variations of $\eta(x)$ and poor accuracy of the calculated free energy F_s. We attribute the deep cusp at $x = \tau$ to the fact that ϕ_0' is discontinuous at this point; as indicated in Fig. 2.2(a) below, using larger m results in deeper cusp and wild oscillations of $\eta(x)$ around $x = \tau$. From Eq. (2.4) one can also see that $\eta^{\mathrm{GSDA}}(x)$ for P1 is discontinuous at $x = \tau$. Moreover, using $\eta^{\mathrm{GSDA}}(x)$ for P1 in Eq. (2.3) results in a diverging F_s.

That $\eta(x)$ seems to follow $\eta^{\mathrm{GSDA}}(x)$ in Fig. 2.1 leads to the following idea of reducing the variations of $\eta(x)$ in the surface layer: By setting $\eta^{\mathrm{GSDA}}(x) = 0$ in Eq. (2.4) and using the boundary conditions of $\phi_{0,sl}(x = 0) = 0$ and $\phi_{0,sl}(x = \tau) = 1$, we obtain a quadratic profile of $\phi_{0,sl}(x) = (x/\tau)^2$ (referred to as P2). The numerically determined $\eta(x)$ for P2 is shown in Fig. 2.2(a), where $d \approx 3.7237$ and $\tau = 0.3$ are used, to be consistent with the calculations below. Similar to the P1 case, the discontinuity of ϕ_0' at $x = \tau$ unfortunately leads to a deep cusp and wild oscillations of $\eta(x)$ around this point, thus poor accuracy of the calculated F_s. This is probably also responsible for the deviation of $\eta(x)$ from $\eta^{\mathrm{GSDA}}(x)$ in the surface layer. The oscillations of $\eta(x)$ very close to the surface can be alleviated by using larger n (data not shown).

Matsen used a cosine profile of $\phi_{0,sl}(x) = [1 - \cos(\pi x/\tau)]/2$ (referred to as COS),[20] which eliminates the discontinuity of ϕ_0' at $x = \tau$. Fig. 2.2(a) also shows the computed $\eta(x)$ for this profile. We see that COS is better than both P1 and P2 in that the variation of $\eta(x)$ is much smaller. However, $\eta^{\mathrm{GSDA}}(x)$ is discontinuous at $x = \tau$, which is probably responsible for the deviation of $\eta(x)$ from $\eta^{\mathrm{GSDA}}(x)$ in the surface layer. Nevertheless, COS allows converging free-energy calculations, as shown in Fig. 2.3. Our results also indicate that, as in the P2 case, the oscillations of $\eta(x)$ very close to the surface can be alleviated by using larger n (data not shown).

From these results, it seems critical that both ϕ_0' and $\eta^{\mathrm{GSDA}}(x)$ need to be continuous at $x = \tau$ to further improve the numerical performance of SCF calculations. Requiring $\phi_{0,sl}(x = 0) = \phi_{0,sl}'(x = 0) = 0$, $\phi_{0,sl}(x = \tau) = 1$, and $\phi_{0,sl}'(x = \tau) = \phi_{0,sl}''(x = \tau) = \phi_{0,sl}'''(x = \tau) = 0$ (the last condition

ensures the continuity of η' at $x = \tau$), we obtain a fifth-order polynomial of $\phi_{0,sl}(x) = -4(x/\tau)^5 + 15(x/\tau)^4 - 20(x/\tau)^3 + 10(x/\tau)^2$ (referred to as P5). Fig. 2.2(b) shows the numerically solved $\eta(x)$ for this profile; we see that smoothly varying $\eta(x)$, which closely follows $\eta^{\mathrm{GSDA}}(x)$, can be obtained by using large enough n. The free-energy calculation using P5 also has higher accuracy than using COS, as shown in Fig. 2.3; in particular, the error of F_s calculated using P5 decays nicely with $m^{-1.9}$.

Finally, we note that for confined homopolymer *solutions* $\nabla^2 q = 0$ for all s at the surfaces. Although we prefer not to introduce a small-molecule solvent into the system due to the complication of additional interaction parameters between the solvent and polymers, this property can be utilized to construct $\phi_0(x)$ that eliminates the divergence of $\eta^{\mathrm{GSDA}}(x)$ at $x = 0$. After some trials, we find that $\phi_{0,sl}(x) = \{\exp[4\tau x/(\tau^2 - x^2)] - 1\}^2/\{\exp[4\tau x/(\tau^2 - x^2)] + 1\}^2$ (referred to as EXP) gives so far the best numerical performance; Fig. 2.3 shows that the error of F_s calculated using EXP decays with $m^{-3.4}$ for $m \geq 128$. Fig. 2.2(c) shows the obtained $\eta(x)$ for this profile, where we see some oscillations of $\eta(x)$ very close to the surface (which can be alleviated by using larger n). We also see some deviation of $\eta(x)$ from $\eta^{\mathrm{GSDA}}(x)$ very close to the surface. Both of these, however, do not affect its superior numerical performance.

2.3.2 Segmental Distributions

It is well known that polymer chains close to an impenetrable (hard) surface lose entropy, and that chain ends lose less entropy than middle segments when close to the surface. We therefore expect the enrichment of chain ends and depletion of middle segments near a hard surface. To quantify this, we define the reduced

distribution function of the $(sN)^{\text{th}}$ segment as

$$\rho(\mathbf{r}, s) = \frac{\bar{\phi}_0 q(\mathbf{r}, s) q(\mathbf{r}, 1-s)}{Q \phi_0(x)} \tag{2.13}$$

such that a constant $\rho(\mathbf{r}, s)$ indicates a uniform distribution of the segment.

Fig. 2.4 shows the end-segment and the middle-segment distributions, $\rho(x, s = 0)$ and $\rho(x, s = 0.5)$, respectively, for homopolymer melts confined by either EXP ($\tau \approx 0.5303$) or P5 profile ($\tau = 0.6$) with $d \approx 3.7237$; the corresponding results of using COS profile ($\tau = 0.4$) are hardly distinguishable from those of using EXP, thus not shown. In all cases, we see that chain ends are enriched near hard surfaces and that $\rho(x, s = 0)$ is inversely proportional to the distance to a surface as the surface is approached. This can be understood by invoking the ground-state dominance approximation (GSDA), which leads to $\rho(x, s) \propto \phi_0^{-1/2}(x)$ for $s = 0$ or 1; note that $\phi_{0,sl}(x) \sim O(x^2)$ as $x \rightarrow 0$ for EXP, P5 and COS profiles. On the other hand, the middle segments are depleted from hard surfaces, and GSDA gives $\rho(x, s) \sim O(1)$ for $0 < s < 1$. Comparing Figs. 2.4(a) with 2.4(b), we see that the range of middle-segment depletion is larger than that of chain-end enrichment.

Although we study in this Section the simplest system of confined homopolymer melts, the above hard-surface effects are generic for all confined polymeric systems. For example, the influence of $\phi_0(x)$ on ω-fields near the surfaces in the case of confined diblock copolymers A-B is the same as that in the homopolymer case (data not shown). The chain-end enrichment and middle-segment depletion in the diblock copolymer case, however, are further

complicated by A-B repulsion (thus microphase separation between A and B) and copolymer composition f_A, as revealed below.

2.4 Confined Symmetric Diblock Copolymer Melts

2.4.1 Surface-Induced Compatabilization

For confined diblock copolymer melts, the decrease of $\phi_{0,sl}(x)$ from 1 reduces the A-B repulsion in the surface layer; this is referred to as the "surface-induced A-B compatibilization" or "negative line tension".[20] This energetic effect therefore favors the morphology where more A-B interfaces (which contribute the most to the A-B repulsion) present in the surface layer. In the case of symmetric diblock copolymers, this has been considered as the dominant factor responsible for the interesting phenomenon that, when the film thickness d is commensurate with the bulk lamellar period l_0, perpendicular lamellae are more stable than parallel lamellae in thin films confined between two neutral surfaces.[20,23,27]

By defining the reduced A-segmental density $\tilde{\phi}_A(\mathbf{r}) \equiv \phi_A(\mathbf{r})/\phi_0(x)$, the A-B interaction energy per chain can be written as

$$F_{AB} \equiv \frac{\chi N}{\bar{\phi}_0 V} \int d\mathbf{r} \phi_A(\mathbf{r}) \phi_B(\mathbf{r}) = \frac{\chi N}{\bar{\phi}_0 V} \int d\mathbf{r} \tilde{\phi}_A(\mathbf{r}) \left[1 - \tilde{\phi}_A(\mathbf{r})\right] \phi_0^2(x) \qquad (2.14)$$

where Eq. (2.9) is used. To quantify the surface-induced compatibilization, we consider the difference in F_{AB} between the parallel and perpendicular lamellae (denoted by $\parallel$ and $\perp$, respectively), $\Delta F_{AB} \equiv F_{AB}^{\parallel} - F_{AB}^{\perp}$, confined between two neutral surfaces. Here we set $\chi N = 15$ and $d = l_0 \approx 3.7237$, and use $\phi_{0,sl}(x) = 1 - [1 + \cos(\pi x/\tau)]\delta/2$ with $\tau = 0.2$ in our calculations such that adjusting δ

from 0 to 1 changes $\phi_{0,si}(x)$ from 1 to COS profile. For both morphologies, if we assume that introducing the hard-surface confinement does not change the *reduced* density, i.e., $\tilde{\phi}_{\mathrm{A}}(\mathbf{r}) = \phi_{\mathrm{A},b}(\mathbf{r})$ with $\phi_{\mathrm{A},b}(\mathbf{r})$ being the density profile under the bulk condition of $\phi_0(x) = 1$, ΔF_{AB} can then be approximated by

$$\Delta F_{\mathrm{AB},b} = \frac{\chi N}{V} \int \mathrm{d}\mathbf{r} \left[\frac{\phi_0^2(x)}{\bar{\phi}_0} - 1 \right] \left\{ \phi^{\parallel}_{\mathrm{A},b}(\mathbf{r}) \left[1 - \phi^{\parallel}_{\mathrm{A},b}(\mathbf{r}) \right] - \phi^{\perp}_{\mathrm{A},b}(\mathbf{r}) \left[1 - \phi^{\perp}_{\mathrm{A},b}(\mathbf{r}) \right] \right\} \tag{2.15}$$

which can be calculated from the bulk structure and $\phi_0(x)$.

Fig. 2.5 shows that, under the bulk condition ($\delta = 0$), lamellae of different orientations degenerate. As δ increases from 0, ΔF_{AB} monotonically increases, indicating that the surface-induced compatibilization favors perpendicular lamellae over parallel ones. The difference between ΔF_{AB} and $\Delta F_{\mathrm{AB},b}$, although small, suggests the change of chain conformations from the bulk counterparts. This is clearly indicated by the large difference between ΔF_{AB} and $\Delta F \equiv F^{\parallel} - F^{\perp}$; the latter even exhibits a maximum at $\delta \approx 0.7$. This leads to the entropic effects of hard-surface confinement, which has been overlooked in previous studies.[20,23,27]

2.4.2 Surface-Induced Entropy Loss

The entropic contribution of the copolymer chains to the system free energy is given by

$$F_{el} \equiv -\frac{1}{\bar{\phi}_0 V} \int \mathrm{d}\mathbf{r} [\omega_{\mathrm{A}}(\mathbf{r})\phi_{\mathrm{A}}(\mathbf{r}) + \omega_{\mathrm{B}}(\mathbf{r})\phi_{\mathrm{B}}(\mathbf{r})] - \ln Q \tag{2.16}$$

As shown in Fig. 2.5, $\Delta F_{el} \equiv F^{\parallel}_{el} - F^{\perp}_{el}$ monotonically decreases with increasing δ, indicating that the entropic effects actually favor parallel lamellae over

perpendicular ones. Fig. 2.5 further indicates that both the energetic and entropic effects have about the same magnitude, and that the competition between them gives rise to the maximum in ΔF.

The reduced distribution function of the $(sN)^{\text{th}}$ segment on a copolymer chain is given by

$$\rho(\mathbf{r}, s) = \frac{\bar{\phi}_0 q(\mathbf{r}, s) q^*(\mathbf{r}, 1-s)}{Q\phi_0(x)} \tag{2.17}$$

Again, a constant $\rho(\mathbf{r}, s)$ indicates a uniform distribution of the segment. Fig. 2.6 shows the reduced distributions of A-ends and A-B joints, $\rho(x, s = 0)$ and $\rho(x, s = 0.5)$, respectively, in parallel lamellae of 1.5 periods confined between two neutral surfaces separated at $d = 1.5l_0$, where we compare the case of hard-surface confinement (EXP profile with $\tau = 0.4$) with that under the bulk condition ($\phi_0(x) = 1$). We clearly see in Fig. 2.6(a) the chain-end enrichment near both surfaces (the B-end distribution can be obtained by the symmetry between A and B), as well as the effects of microphase separation between A and B on the chain-end enrichment. The hard-surface effects on the joint-segment distribution, as shown in Fig. 2.6(b), are more interesting: While A-B joints are "squeezed" towards the interior of the film as expected, $\rho(x, s = 0.5)$ exhibits small increase in the vicinity of the surfaces in comparison to the minima in the interior of the film. Such increase, although entropically unfavorable, is due to the surface-induced A-B compatibilization.

Fig. 2.7 shows $\rho(x, s = 0)$ and $\rho(x, s = 0.5)$ in perpendicular lamellae (microphase-separated along the y direction) confined between two neutral surfaces separated at $d = 1.5l_0$, where we again compare the case of hard-surface

confinement (EXP profile with $\tau = 0.4$) with that under the bulk condition ($\phi_0(x) = 1$). To highlight the influence of microphase separation, two y-values are chosen: For A-end distribution shown in Fig. 2.7(a), we choose the center of A-rich domains (where $\phi_A(y)$ reaches a maximum value of 0.9403) and that of B-rich domains (where $\phi_A(y)$ reaches a minimum value of 0.0597); for A-B joints shown in Fig. 2.7(b), we choose the center of either A- or B-rich domains and the A-B interface (where $\phi_A(y) = \phi_B(y)$). As in the parallel lamellae case, in Fig. 2.7(a) we clearly see the chain-end enrichment near hard surfaces and the effects of microphase separation on the enrichment. In Fig. 2.7(b), we see the depletion of joint segments from the surfaces when their density is high (e.g., at A-B interfaces), while the surface-induced A-B compatibilization causes some increase of joint segments in the vicinity of the surfaces when their density is low (e.g., at the center of A- or B-rich domains). Comparing Figs. 2.6 and 2.7, we see that, overall, there are more chain ends and less joint segments near surfaces in parallel lamellae than in perpendicular lamellae; the entropic effects therefore favor parallel lamellae, consistent with ΔF_{el} shown in Fig. 2.5. We note that the chain-end effect on lamellar orientation was analyzed by Pickett and co-workers.[38,39]

2.4.3 *Influence of $\phi_0(\mathbf{x})$ on Phase Behavior*

To quantify the influence of various functional forms of $\phi_0(x)$ and the τ-values on the phase behavior of confined diblock copolymers, we consider symmetric diblock copolymers ($\chi N = 15$) confined between two identical surfaces preferring A block separated at $d = l_0$. Here we use a surface field symmetric about $x = d/2$, $H(x) = \Lambda[1 + \cos(\pi x/\tau)]/2$ in the surface layer and 0 elsewhere (with $\Lambda > 0$ denoting the strength of surface preference), and focus on how Λ at

the phase boundary between parallel lamellae of one period and perpendicular lamellae, Λ_0, changes with different choices of $\phi_{0,si}(x)$ and τ.

We obtain $\Lambda_0 \approx 1.89$ for EXP profile with $\tau = 0.4$, and $\Lambda_0 \approx 2.06$ for COS profile with $\tau \approx 0.3017$ (which gives the same $\bar{\phi}_0$ as the EXP profile). The functional forms of $\phi_0(x)$ therefore only have minor influence on the phase behavior, and hence can be chosen based on the numerical performance of SCF calculations. On the other hand, using EXP profile with $\tau = 0.2$ changes Λ_0 to 0.64; the influence of τ is therefore more significant, as expected.

Although depending on the functional form of $H(x)$, these Λ_0-values can be compared with that of χN, indicating that the hard-surface effects are weak in practice. Therefore, although these effects exist in all confined polymeric systems, they are manifested only when the surfaces are nearly neutral. This validates the idea of ignoring hard-surface effects for stronger surface preference, where one can use the bulk condition of $\phi_0(x) = 1$ (thus the Neumann boundary conditions) for confined systems to avoid large m-values needed to resolve the surface layer.

2.5 Confined Asymmetric Diblock Copolymers

For symmetric diblock copolymers confined between two identical surfaces, the hard surfaces affect A and B segments equally due to the symmetry between them. This is not the case for confined asymmetric diblock copolymers. Both dynamic density-functional calculations[40] and lattice Monte Carlo simulations[30] have shown an entropic preference of a hard surface for the shorter block. We

therefore investigate the hard-surface effects on cylinder-forming asymmetric diblock copolymers in this Section.

2.5.1 Hard-Surface Effects

Fig. 2.8 shows the free-energy difference between parallel and perpendicular cylinders, as well as its energetic and entropic components, for cylinder-forming asymmetric diblock copolymers ($\chi N = 25$) confined by EXP profile ($\tau = 0.4$) between two neutral surfaces separated at $d = \sqrt{3}l_0$, where l_0 here represents the smallest inter-cylinder distance in the bulk. Interestingly, we see that the surface-induced entropy loss favoring parallel cylinders now outweighs the surface-induced A-B compatibilization favoring perpendicular cylinders. Without further calculations, however, one should not generalize this result to other values of χN and f_A.

For the case of $f_A = 0.22$, Fig. 2.9 shows in solid curves the A-B interfaces (where $\phi_A(\mathbf{r}) = \phi_B(\mathbf{r})$) in these two morphologies; corresponding results under the bulk condition ($\phi_0(x) = 1$) are also shown in dots. We see enlargement of A-rich regions near the hard surfaces, which results in the shrinkage of A-cylinders in the interior of the film in the case of parallel cylinders and the undulation of A-B interfaces in the case of perpendicular cylinders. The neutral, hard surfaces indeed exhibit preference for the shorter (A) block.

To examine the change in chain conformations due to the hard-surface confinement, Fig. 2.10 shows the reduced distributions of A-ends, B-ends and A-B joints in these two morphologies. As in the case of confined symmetric diblock copolymers, we clearly see chain-end enrichment near hard surfaces and

the effects of microphase separation between A and B on the enrichment. For parallel cylinders, Fig. 2.10(c) further shows the depletion of joint segments from the surfaces when their density is high (e.g., at A-B interfaces), while the surface-induced A-B compatibilization causes small increase of joint segments in the vicinity of the surfaces when their density is low (e.g., at the center of B-rich domains). For perpendicular cylinders, we note that the overall enrichment of joint segments near hard surfaces is caused not only by the surface-induced A-B compatibilization, but also by the entropic preference of the surfaces for the shorter block. Overall (data not shown), there are more chain ends near surfaces in parallel cylinders than in perpendicular cylinders; the entropic effects therefore favor parallel cylinders, consistent with ΔF_{el} shown in Fig. 2.8.

Comparing A- with B-ends, however, we see that the chain-end enrichment is more pronounced for the shorter (A) block. This is the case not only for cylinder-forming asymmetric diblock copolymers as shown in Fig. 2.10, but also for lamellae-forming asymmetric diblock copolymers (e.g., $f_{\mathrm{A}} = 0.4$ and $\chi N = 15$; data not shown). This phenomenon is caused by A-B repulsion ($\chi > 0$), since for confined homopolymers (effectively $\chi = 0$) both chain ends enrich equally. The entropic preference of a hard surface for the shorter block was explained in Ref. [30] based on chain-end enrichment and chain connectivity (i.e., the shorter block is on average closer to a chain end than the longer block); it occurs even for equal enrichment of A- and B-ends. A-B repulsion therefore enhances this entropic preference.

2.5.2 Effectively Neutral Surface

As shown in Fig. 2.9(b), the undulation of A-B interfaces in perpendicular cylinders is a manifestation of the entropic preference of hard surfaces for the shorter block. To quantify this entropic preference, we introduce an energetic preference of the surfaces for the longer (B) block, i.e., $\Lambda < 0$, and characterize the undulation by

$$A_u \equiv \frac{1}{l_y l_z} \int \mathrm{d}y\mathrm{d}z \frac{\phi_{\mathrm{A}}(x = \frac{d}{m}, y, z)}{\phi_0(x = \frac{d}{m})} - f_{\mathrm{A}} \tag{2.18}$$

At $\Lambda = \Lambda_0$, A_u vanishes and we have effectively neutral surfaces, near which both chain ends are equally enriched (data not shown).

For perpendicular cylinders ($\chi N = 25$) confined by EXP profile ($\tau = 0.4$) between two identical surfaces separated at $d = \sqrt{3} l_0$, we obtain $\Lambda_0 \approx -2.72$ and -1.51 for $f_{\mathrm{A}} = 0.22$ and 0.3, respectively. As expected, the entropic preference is stronger for more asymmetric diblock copolymers. Similar to the hard-surface effects for confined symmetric diblock copolymers, however, such entropic preference is weak in practice.

2.6 Conclusions

We have investigated several effects resulting from the confinement of polymer melts by impenetrable (hard) surfaces using self-consistent field (SCF) calculations. To adequately represent such confinement, a total (normalized) polymer density profile ($\phi_0(x)$) is usually imposed, which continuously decreases from 1 in the interior of confined melts (bulk condition) to 0 at the surfaces over a short distance (surface layer). The choice of this profile in the surface layer,

$\phi_{0,sl}(x)$, strongly influences the numerical performance of the self-consistent field calculations. We have identified two profiles (P5 and EXP) of $\phi_{0,sl}(x)$, which make the calculations converge rapidly with refined discretization.

Hard-surface confinement also changes chain conformations from the bulk counterparts, leading to the enrichment of chain ends and depletion of middle segments near the surfaces. For confined diblock copolymers A-B, these entropic effects favor parallel morphologies where chains orient mainly perpendicular to the surfaces. They are, however, further complicated by A-B repulsion (thus microphase separation between A and B) and copolymer composition f_{A}. The decrease of polymer density from 1 reduces A-B repulsion and favors morphologies with more A-B interfaces near the surfaces. Such surface-induced A-B compatibilization (energetic effect) therefore acts against the depletion of A-B joints from the surfaces. In the case of symmetric diblock copolymers confined between two neutral surfaces, when the film thickness is commensurate with the bulk lamellar period, the energetic effect favoring perpendicular lamellae outweighs the entropic effects. The latter, however, are comparable in magnitude to the former and cannot be overlooked. For confined asymmetric diblock copolymers, the chain-end enrichment results in an entropic preference of a neutral surface for the shorter block, which is enhanced by A-B repulsion.[30]

Our calculations also show that different functional forms of $\phi_{0,sl}(x)$ only have minor influence on the phase behavior of confined diblock copolymers, and hence can be chosen based on the numerical performance of SCF calculations. After all, the hard-surface effects are weak in practice and are manifested only when the surfaces are nearly neutral. This validates the idea of ignoring

hard-surface effects for stronger surface preference, where one can use the bulk condition of $\phi_0(x) = 1$ (thus the Neumann boundary conditions) for confined systems to avoid the large number of collocation points needed to resolve the surface layer.

List of Figures

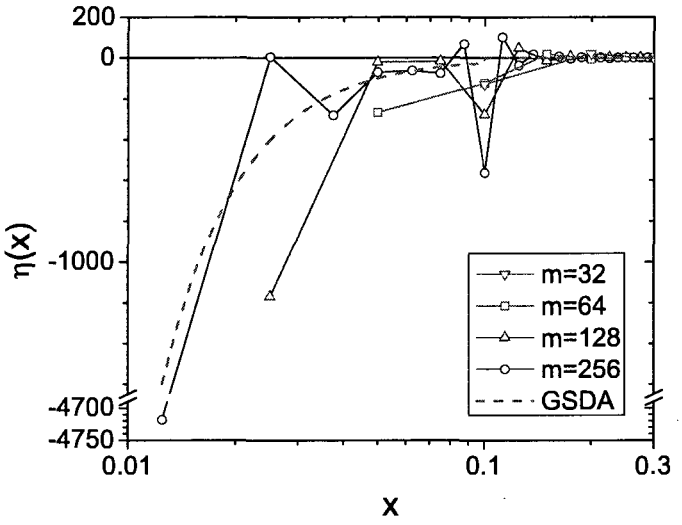

Fig. 2.1: Pressure field $\eta(x)$ for confined homopolymer melts, with the linear profile P1 used in the surface layer. $d = 3.2$, $\tau = 0.1$, and $n = 2048$.

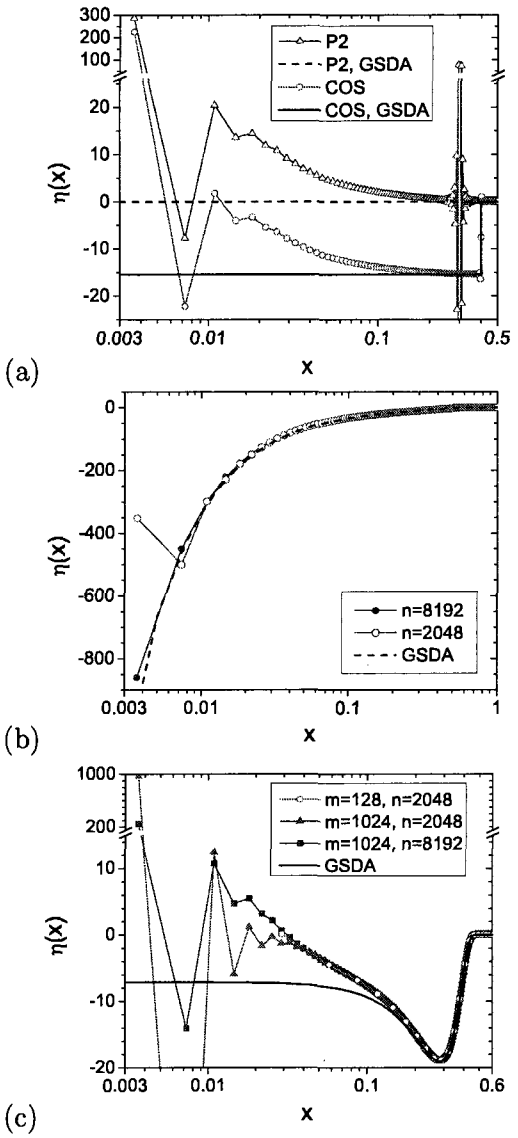

Fig. 2.2: Pressure field $\eta(x)$ for confined homopolymer melts, where $d \approx 3.7237$ and the τ-values are chosen to give the same $\bar{\phi}_0$ in all cases: (a) The quadratic profile P2 ($\tau = 0.3$) and the cosine profile COS ($\tau = 0.4$) are used in the surface layer, respectively. $m = 1024$ and $n = 2048$. In the P2 case, two data points located around $x = \tau$ with η-values less than -500 are not shown. (b) The fifth-order polynomial P5 ($\tau = 0.6$) is used in the surface layer. $m = 1024$. (c) The profile EXP ($\tau \approx 0.5303$) is used in the surface layer. For the case of $m = 1024$ and $n = 2048$, a minimum located around $x \approx 7.3 \times 10^{-3}$ with η-value about -73 is not shown.

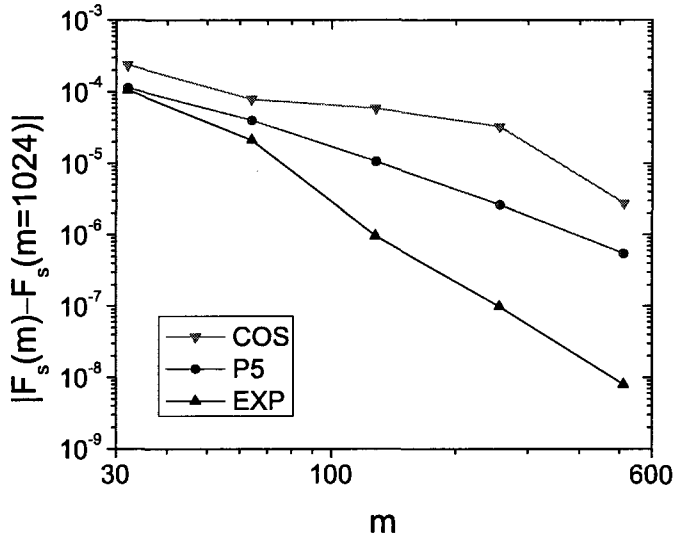

Fig. 2.3: Influence of spatial-domain discretization on the accuracy of free-energy calculations for confined homopolymers. $d \approx 3.7237$ and $n = 2048$. The τ-values are given in the caption of Fig. 2.2. Here we approximate the exact value of F_s (obtained when $m \to \infty$) by that calculated with the largest m, $F_s(m = 1024)$.

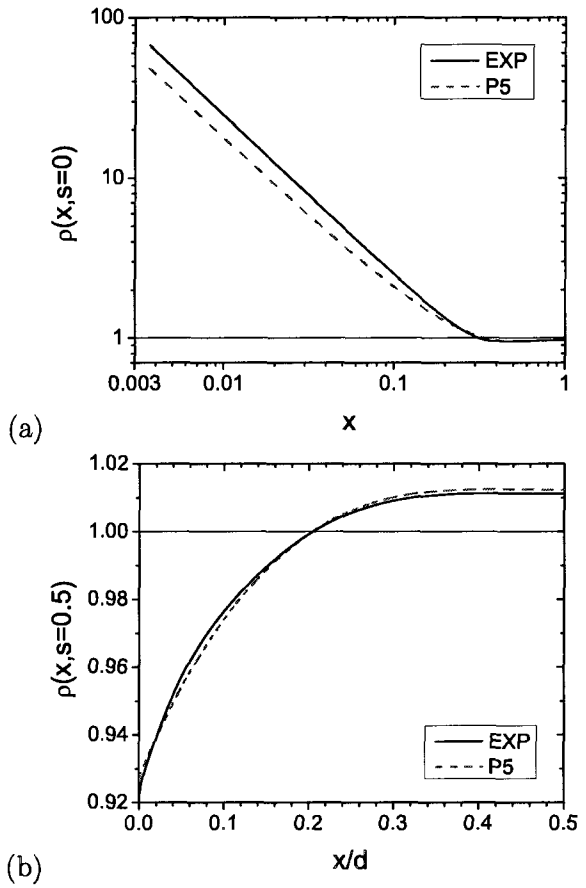

Fig. 2.4: Reduced distributions of (a) the end-segments and (b) the middle-segments in confined homopolymer melts, where $d \approx 3.7237$, $m = 1024$ and $n = 8192$. The τ-values are given in the caption of Fig. 2.2. The results of using COS profile are hardly distinguishable from those of using EXP, thus not shown. In the log-log plot shown in part (a), the curves approach a slope of -1 as $x \to 0$. In part (b), the curves are symmetric about $x = d/2$. Under the bulk condition ($\phi_0(x) = 1$) a constant value of 1 is expected for these distributions.

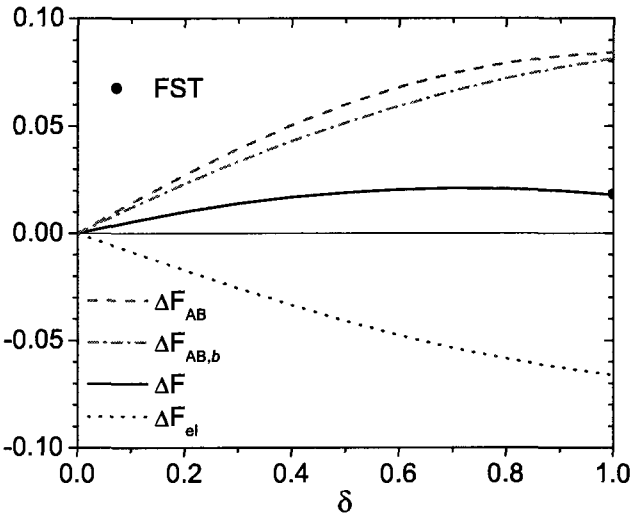

Fig. 2.5: Free-energy differences between parallel and perpendicular lamellae of symmetric diblock copolymers ($f_A = 0.5$ and $\chi N = 15$) between two neutral surfaces separated at $d = l_0 \approx 3.7237$. Here we use $\phi_{0,sl}(x) = 1 - [1 + \cos(\pi x/\tau)]\delta/2$ (with $\tau = 0.2$) such that adjusting δ from 0 to 1 changes $\phi_{0,sl}(x)$ from 1 to COS profile, and accordingly the Neumann boundary conditions in the x direction. The dot at $\delta = 1$ represents ΔF calculated using the Dirichlet boundary conditions where the fast sine transform (FST) is used accordingly.

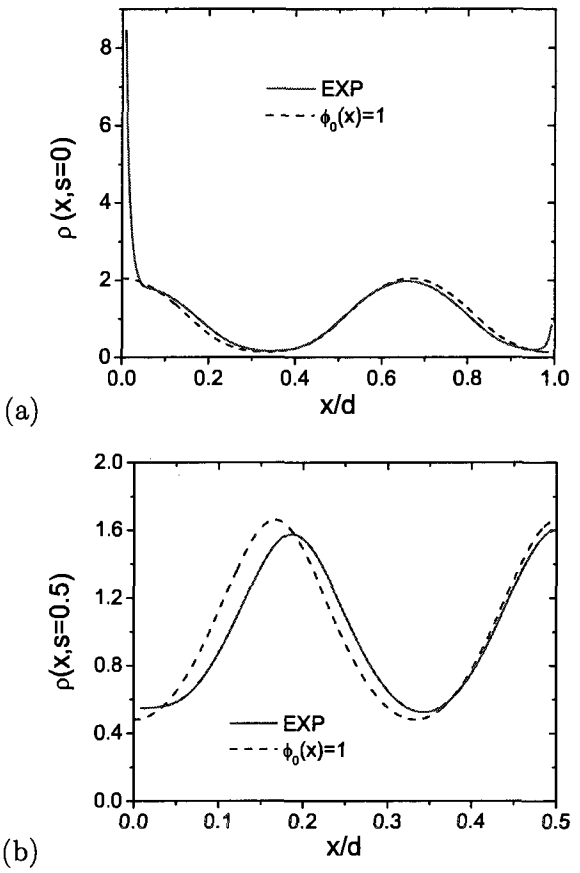

Fig. 2.6: Reduced distributions of (a) A-ends and (b) A-B joints in parallel lamellae of symmetric diblock copolymers ($f_A = 0.5$ and $\chi N = 15$) of 1.5 periods confined between two neutral surfaces separated at $d = 1.5l_0 \approx 5.5856$. Here we compare the case of hard-surface confinement (EXP profile with $\tau = 0.4$) with that under the bulk condition ($\phi_0(x) = 1$). The B-end distribution can be obtained by the symmetry between A and B.

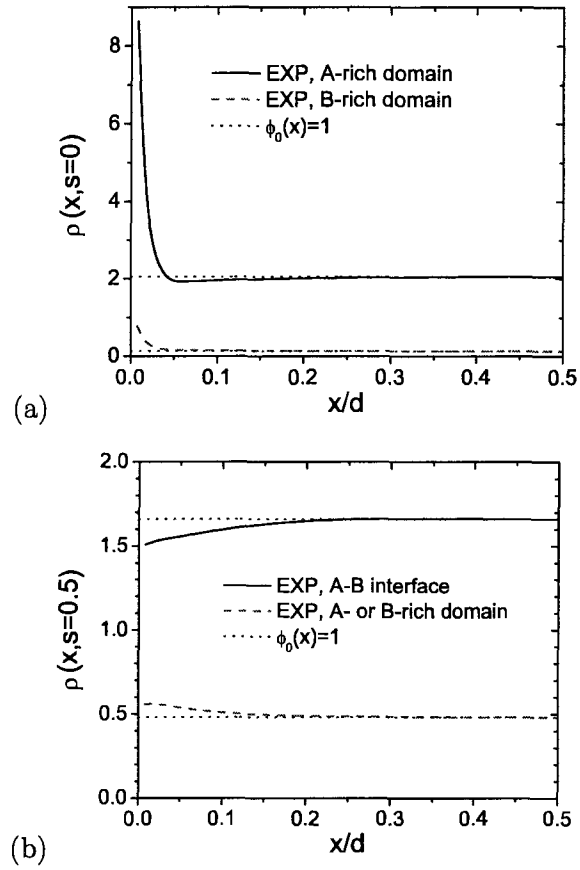

Fig. 2.7: Reduced distributions of (a) A-ends and (b) A-B joints in perpendicular lamellae of symmetric diblock copolymers ($f_A = 0.5$ and $\chi N = 15$, microphase-separated along the y direction) confined between two neutral surfaces separated at $d = 1.5l_0 \approx 5.5856$. Here we compare the case of hard-surface confinement (EXP profile with $\tau = 0.4$) with that under the bulk condition ($\phi_0(x) = 1$). The B-end distribution can be obtained by the symmetry between A and B. In the legend, the A-rich domain corresponds to a y-value where $\phi_A(y)$ reaches a maximum of 0.9403, the B-rich domain corresponds to a y-value where $\phi_A(y)$ reaches a minimum of 0.0597, and the A-B interface is where $\phi_A(y) = \phi_B(y)$.

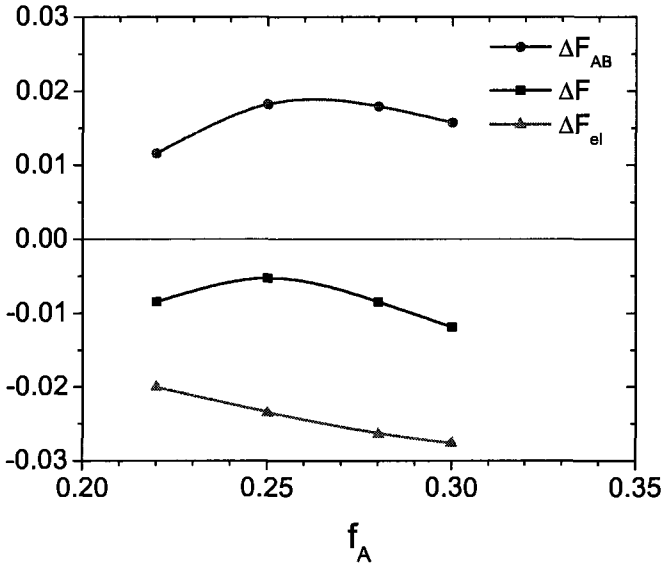

Fig. 2.8: Free energy differences between parallel and perpendicular cylinders of asymmetric diblock copolymers ($\chi N = 25$) confined by EXP profile ($\tau = 0.4$) between two neutral surfaces separated at $d = \sqrt{3}l_0$. $l_0 \approx 3.9266$, 4.1266, 4.2832, and 4.4068 for $f_A = 0.22$, 0.25, 0.28, and 0.3, respectively. The data points are actual calculations, and the curves are guide to eyes only. $l_y = l_0$ and $l_z = \sqrt{3}l_0$ (for perpendicular cylinders) are used in our calculations.

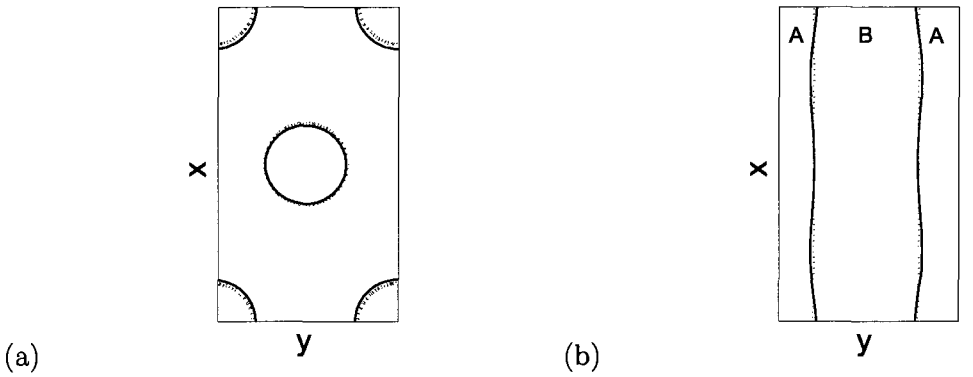

Fig. 2.9: A-B interfaces (where $\phi_A(\mathbf{r}) = \phi_B(\mathbf{r})$) in (a) parallel cylinders (whose axis is along the z direction) and (b) perpendicular cylinders of asymmetric diblock copolymers ($f_A = 0.22$ and $\chi N = 25$) confined between two neutral surfaces separated at $d = \sqrt{3}l_0 \approx 6.8010$. The solid curves show the results under confinement by EXP profile ($\tau = 0.4$), and the dotted curves show corresponding results under the bulk condition ($\phi_0(x) = 1$). $l_y = l_0$ and $l_z = \sqrt{3}l_0$ (for perpendicular cylinders) are used in our calculations.

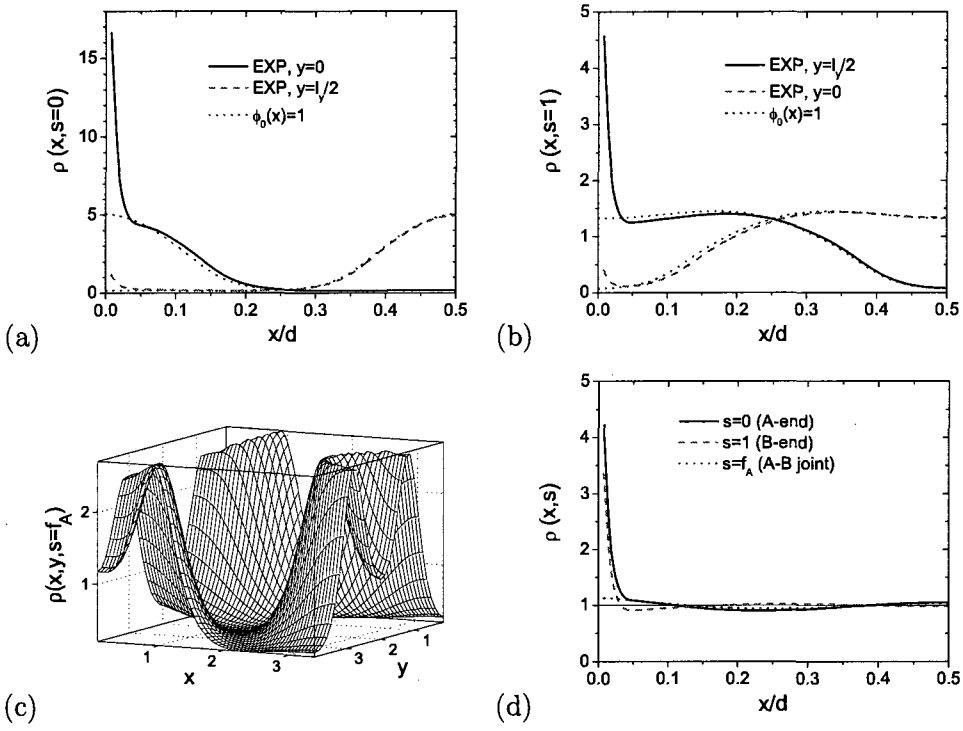

Fig. 2.10: Reduced distributions of (a) A-ends, (b) B-ends and (c) A-B joints in parallel cylinders of asymmetric diblock copolymers ($f_A = 0.22$ and $\chi N = 25$) confined between two neutral surfaces separated at $d = \sqrt{3}l_0 \approx 6.8010$. In parts (a) and (b) we compare the case of hard-surface confinement (EXP profile with $\tau = 0.4$) with that under the bulk condition ($\phi_0(x) = 1$), and use two y-values corresponding to Fig. 2.9(a). In part (c) only the results of hard-surface confinement are shown for clarity. Part (d) shows these distributions in perpendicular cylinders, where under the bulk condition a constant value of 1 is expected for these distributions. In all cases, the distributions are symmetric about $x = d/2$, and $l_y = l_0$ and $l_z = \sqrt{3}l_0$ (for perpendicular cylinders) are used in our calculations.

BIBLIOGRAPHY

[1] S. F. Edwards, Proc. Phys. Soc., **85**, 613 (1965).

[2] E. Helfand and Y. Tagami, J. Polym. Sci., Part B: Polym. Lett., **9**, 741 (1971).

[3] E. Helfand and Y. Tagami, J. Chem. Phys., **56**, 3592 (1972); **57**, 1812 (1972).

[4] E. Helfand and A. M. Sapse, J. Chem. Phys., **62**, 1327 (1975).

[5] K. M. Hong and J. Noolandi, Macromolecules, **14**, 736 (1981).

[6] J. Noolandi and K. M. Hong, Macromolecules, **15**, 482 (1982).

[7] J. Noolandi and K. M. Hong, Macromolecules, **17**, 1531 (1984).

[8] K. R. Shull and E. J. Kramer, Macromolecules, **23**, 4769 (1990).

[9] K. R. Shull, Macromolecules, **26**, 2346 (1993).

[10] M. D. Whitmore and J. D. Vavasour, Acta Polym., **46**, 341 (1995).

[11] M. W. Matsen and F. S. Bates, Macromolecules, **29**, 1091 (1996).

[12] M. W. Matsen, J. Phys.: Condens. Matter, **14**, R21 (2002).

[13] G. J. Fleer, M. A. Cohen Stuart, J. M. H. M. Scheutjens, T. Cosgrove, and B. Vincent, Polymers at Interfaces, Chapman & Hall: London, 1993.

[14] G. J. Fleer and F. A. M. Leermakers, Curr. Opin. Colloid Interface Sci., **2**, 308 (1997).

[15] M. W. Matsen and M. Schick, Phys. Rev. Lett., **72**, 2660 (1994).

[16] G. Tzeremes, K. O. Rasmussen, T. Lookman, and A. Saxena, Phys. Rev. E, **65**, 041806 (2002).

[17] E. W. Cochran, C. J. Garcia-Cervera, and G. H. Fredrickson, Macromolecules, **39**, 2449 (2006); **39**, 4264 (2006).

[18] H. D. Ceniceros and G. H. Fredrickson, Multiscale Model. Simul., **2**, 452 (2004).

[19] S. W. Sides and G. H. Fredrickson, Polymer, **44**, 5859 (2003).

[20] M. W. Matsen, J. Chem. Phys., **106**, 7781 (1997).

[21] H. Y. Chen and G. H. Fredrickson, J. Chem. Phys., **116**, 1137 (2002).

[22] W. H. Li, R. A. Wickham, and R. A. Garbary, Macromolecules, **39**, 806 (2006).

[23] T. Geisinger, M. Muller, and K. Binder, J. Chem. Phys., **111**, 5241 (1999).

[24] I. W. Hamley, Nanotechnology, **14**, R39 (2003).

[25] M. Lazzari and M. A. Lopez-Quintela, Adv. Mater., **15**, 1583 (2003).

[26] C. Park, J. Yoon, and E. L. Thomas, Polymer, **44**, 6725 (2003).

[27] W. H. Tang, Macromolecules, **33**, 1370 (2000).

[28] J. U. Sommer, A. Hoffmann, and A. Blumen, J. Chem. Phys., **111**, 3728 (1999).

[29] Q. Wang, Q. L. Yan, P. F. Nealey, and J. J. de Pablo, J. Chem. Phys., **112**, 450 (2000).

[30] Q. Wang, P. F. Nealey, and J. J. de Pablo, Macromolecules, **34**, 3458 (2001).

[31] G. H. Fredrickson, The Equilibrium Theory of Inhomogeneous Polymers, Oxford University Press, 2006.

[32] Chapter 16.4 in W. H. Press, S. A. Teukolsky, W. T. Vetterling, and B. P. Flannery, Numerical Recipes in C: the Art of Scientific Computing, 2nd ed. Cambridge University Press, 2002.

[33] Chapter 9.7 in W. H. Press, S. A. Teukolsky, W. T. Vetterling, and B. P. Flannery, Numerical Recipes in C: the Art of Scientific Computing, 2nd ed. Cambridge University Press, 2002.

[34] Chapter 4.3 in W. H. Press, S. A. Teukolsky, W. T. Vetterling, and B. P. Flannery, Numerical Recipes in C: the Art of Scientific Computing, 2nd ed. Cambridge University Press, 2002.

[35] W. H. Li and R. A. Wickham, Macromolecules, **39**, 8492 (2006).

[36] K. O. Rasmussen, J. Polym. Sci.: Part B: Polym. Phys., **42**, 3695 (2004).

[37] Y. Z. Yang, F. Qiu, H. D. Zhang, and Y. L. Yang, Polymer, **47**, 2205 (2006).

[38] G. T. Pickett, T. A. Witten, and S. R. Nagel, Macromolecules, **26**, 3194 (1993).

[39] G. T. Pickett and A. C. Balazs, Macromolecules, **30**, 3097 (1997).

[40] H. P. Huinink, J. C. M. Brokken-Zijp, M. A. van Dijk, and G. J. A. Sevink, J. Chem. Phys., **112**, 2452 (2000).

3. COMPLEX MORPHOLOGIES IN THIN FILMS OF SYMMETRIC DIBLOCK COPOLYMERS

3.1 Introduction

Block copolymers possess great potential for applications in nanotechnology because of their ability to self-assemble into well ordered nanostructures under certain conditions and the direct control of these structures by copolymer synthesis.[1] While the phase behavior of bulk block copolymers have been extensively studied by both experiment and theory,[1–3] many applications of block copolymers require thin-film geometries, such as in surface coating, nano-membrane, nano-lithography, and high-density storage media, where the self-assembly of block copolymer is strongly affected by the presence of confining surfaces.[4,5] It is therefore of both fundamental and practical interest to understand how nano-confinement changes the self-assembly of block copolymers, and further use it to control the nanostructures obtained.

In this work, we consider the simplest system of symmetric diblock copolymer melts A-B, which form one-dimensional (1D) lamellar structures in the bulk with a characteristic period L_0, under 1D confinement between two parallel, homogeneous and impenetrable (hard) surfaces. The confining surfaces have three effects on the thin-film morphology: First, a surface generally exhibits

energetic preference for one of the two blocks, due to the difference in surface-block interactions. This results in lamellae oriented parallel to the surfaces to reduce surface-block interaction energy.[4–18] Second, the two surfaces have a confining effect. When the surface separation D is incommensurate with the bulk lamellar period L_0 (i.e., when D/L_0 is not an integer in the case of two surfaces preferring the same type of segments, or not half an odd integer in the case of two surfaces preferring different types of segments), such frustration forces the copolymers to change their lamellar period to be different from L_0,[5–10,15,17–19] or even to adopt a different (perpendicular) lamellar orientation to restore L_0 when the frustration is large at the cost of increasing the surface-block interaction energy.[5,9,10,15,17,18,20–29]

While these two effects are well understood, the third effect, referred to as the "hard-surface effect",[10,19] is that a neutral, hard surface induces the formation of perpendicular lamellae.[10,11,15,17,18,22,23,27,28,30–33] This is due to the impenetrability of the confining surface (i.e., polymer density at the surface must be zero), and have both energetic and entropic aspects. The decrease of polymer density near the surface (from that in the interior of the confined melts) reduces the A-B repulsion, and thus favors perpendicular lamellae with more A-B interfaces (which contribute the most to the A-B repulsion) near the surfaces, known as the "surface-induced A-B compatibilization".[15] On the other hand, the enrichment of chain ends and depletion of middle segments near the hard surface favor parallel lamellae where chains orient mainly perpendicular to the surface. In the case of symmetric diblock copolymers confined between two neutral surfaces, when D is commensurate with L_0, our recent study shows that the energetic aspect outweigh the entropic one.[19]

By fine tuning the surface-block interactions and the thickness of the confined film, one can therefore obtain parallel lamellae, perpendicular lamellae, and complex morphologies (mixed lamellae) of parallel orientation near one surface and perpendicular orientation near the other.[10,21,22,29–32,34,35] However, the detailed structures and formation mechanisms of these complex morphologies, even their existence, have been controversial in the past, and are therefore the focus of this work.

Some publications[21,29,31,34,35] have reported the existence of mixed lamellae for symmetric diblock copolymer thin films in addition to the parallel and perpendicular lamellae. Huang and co-workers[31] concluded that the formation of mixed lamellae is more due to surface preference effect than the confining effect because the existence of the pependicular orientation in mixed lamellae alleviates the incommensurability of thin film thickness with the natural period. Koneripalli and co-workers[21] examined the commensurability effect on the thin film morphology using two dissimilar surfaces (i.e., two surfaces preferring different blocks). Mixed lamellae were observed when film thickness is close to the natural period of lamellae, and disappeared upon the removal of one confining surface.

The Monte Carlo simulations done by Kikuchi and Binder[9] with symmetric surfaces shows a similar commensurability effect with Koneripalli's work but later was proved to be a result of the mismatch between the size of natural period of lamellae and the size of simulation box.[9] Wang's simulation[36] using dissimilar surfaces and thick films shows the existence of mixed lamellae,but the simulation with film thickness close to natural lamellae period did not produce

a well developed morphology.

Recently SCF calculations were also applied to the study of mixed lamellae. Matsen[15] used SCF calculation in continuum to search for the mixed lamellae for symmetric diblock copolymer system. But his work was limited to the case of symmetric surfaces based on the hypothesis that it is the region where mixed lamellae will be mostly favored. But symmetric diblock copolymers can only exhibit symmetric morphologies under symmetric surface preferences, which is actually contradictory to the asymmetric character of the mixed lamellae morphologies reported from experiments. Thus the mixed lamellae are preferred in the region with symmetric surface preferences and as the result his work concluded mixed lamellae to be unstable. In other efforts to search for the mixed lamellae, Fasolka[29] and Tang[28] separately carried out lattice SCF calculations with diblock copolymer being confined between dissimilar surfaces. Fasolka's work suggested a stable mixed lamellae phase, with the same method however Tang's work gave an opposite answer. This contradiction partly is due to the low accuracy of the lattice model. Also all these calculations are two dimensional SCF calculations which exclude the possibility of formation of three dimensional structures.

In this study, we use the SCF method in a continuum to study a symmetric diblock copolymer system under planer confinement. Our goal is to find mixed lamellae and to locate the stable region of this morphology by systematically varying the system parameters such as surface preferences and film thickness D.

3.2 Models and Numerical Methods

3.2.1 Self-Consistent Field Calculations

Here we consider symmetric diblock copolymers A-B of chain length N confined between two flat and impenetrable surfaces placed at $x = 0$ and D. Assuming that all polymer segments have the same statistical segmental length a, the SCF equations stays the same as Eq. (2.5)~(2.9).

$\phi_{\mathrm{A}}(\mathbf{r})$ and $\phi_{\mathrm{B}}(\mathbf{r})$ are the density fields of A and B segments, respectively, and $\omega_{\mathrm{A}}(\mathbf{r})$ and $\omega_{\mathrm{B}}(\mathbf{r})$ are the conjugate fields interacting these species. We use χ to denote the Flory-Huggins interaction parameter between A and B segments and $\chi N = 15$ is used in our calculations, which gives the bulk lamellar period $L_0 = 3.714R_g$, with $R_g \equiv a\sqrt{N/6}$.

$H(\mathbf{r})$ is a field representing the energetic surface preference for the two blocks: it is positive when the surface prefers A segments and negative when the surface prefers B segments. In this section we set

$$H(\mathbf{r}) = \begin{cases} \Lambda_l(1 - \frac{x}{\tau}) & \text{for } 0 \le x \le \tau \\ 0 & \text{for } \tau \le x \le D - \tau \\ \Lambda_u(1 - \frac{D-x}{\tau}) & \text{for } D - \tau \le x \le D \end{cases} \tag{3.1}$$

with $\tau = 0.2R_g$, where Λ_l and Λ_u denote the strength of preference for the lower and upper surfaces, respectively; a positive Λ-value corresponds to an A-preferential surface, and a negative Λ-value for a B-preferential surface. $\eta(\mathbf{r})$ is the (purely imaginary) conjugate field enforcing the generalized incompressibility condition, Eq. (2.9). According to our previous work,[19] for the two impenetrable

surfaces we use the EXP profile, i.e.,

$$\phi_0(\mathbf{r}) = \begin{cases} \frac{\exp[4\tau x/(\tau^2-x^2)]-1^2}{\exp[4\tau x/(\tau^2-x^2)]+1^2} & \text{for } 0 \le x \le \tau \\ 1 & \text{for } \tau \le x \le D-\tau \\ \frac{\exp[4\tau (D-x)/(\tau^2-(D-x)^2)]-1^2}{\exp[4\tau (D-x)/(\tau^2-(D-x)^2)]+1^2} & \text{for } D-\tau \le x \le D. \end{cases} \tag{3.2}$$

which ensures good numerical performance of our SCF calculations with the hard-surface effect. For comparison, we also perform SCF calculation without the hard-surface effect, where we set $\phi_0(\mathbf{r}) = 1$. In either case, $\bar{\phi}_0 \equiv \int d\mathbf{r}\phi_0(\mathbf{r})/V$ with $V \equiv L_y L_z D$ being the system volume. Here, we have normalized all the distance by $R_g \equiv a\sqrt{N/6}$.

In Eq. (7.4), $f_A = 1/2$ denotes the volume fraction of the A block in the copolymer, $s \in [0,1]$ is a variable denoting the segmental position along the chain contour, and the propagator $q(\mathbf{r}, s)$ corresponds to the probability of finding a partial copolymer chain of length sN that starts from $s = 0$ (the A end) anywhere in the system and ends at position $\mathbf{r}$, which satisfies the modified diffusion equation (MDE) Eq. (6.8). Similarly, $q^*(\mathbf{r}, t)$ with $t \equiv 1 - s$ corresponds to the probability of finding a copolymer chain of length tN that starts from the B-end (where $s = 1$) anywhere in the system and ends at $\mathbf{r}$, and satisfies Eq. (2.11).

Two sets of boundary and initial conditions for MDEs, Eqs. (2.10) and (2.11), are used in our calculations: For calculations with the hard-surface effect, i.e., where Eq. (3.2) is used, we apply the Dirichlet boundary conditions of $q(\mathbf{r}, s) = q^*(\mathbf{r}, s) = 0$ at $x = 0$ and D for all s, together with the initial

conditions of $q(\mathbf{r}, s = 0) = q^*(\mathbf{r}, t = 0) = 1$ at $0 < x < D$; for calculations without hard-surface effects, i.e., where $\phi_0(\mathbf{r}) = 1$, we apply the Neumann boundary conditions of $\partial q(\mathbf{r}, s)/\partial x = \partial q^*(\mathbf{r}, s)/\partial x = 0$ at $x = 0$ and D for all s, together with the initial conditions of $q(\mathbf{r}, s = 0) = q^*(\mathbf{r}, t = 0) = 1$ at all $\mathbf{r}$. For multi-dimensional calculations, periodic boundary conditions are applied in the y and z directions. Finally, the single-chain partition function $Q \equiv \int \mathrm{d}\mathbf{r} q(\mathbf{r}, s = 1)/V$.

With the Dirichlet boundary condition (i.e., with the hard-surface effect), we perform two-dimensional calculations and solve MDEs, Eqs. (2.10) and (2.11), using the fourth-order implicit-explicit scheme;[37] in such cases, the confined dimension is uniformly discretized into 64 subintervals with the fast sine transforms (FST) being applied. With the Neumann boundary condition (i.e., without the hard-surface effect), we perform three-dimensional calculations and solve MDEs using the split-step pseudo-spectral method;[38] in such cases, all the three dimensions are uniformly discretized into 64 subintervals, and the fast cosine transforms (FCT) are used in the confined dimension. In all cases, the fast Fourier transforms (FFT) are used in the unconfined dimension(s), the chain contour length is uniformly discretized into 256 steps, and the recently proposed semi-implicit scheme[39] is used to iterate the SCF equations, Eqs. (2.5)$\sim$(2.9), till the the maximum residual error at all collocation points $\mathbf{r}$, $\max\{|[\omega_\mathrm{A}(\mathbf{r}) - \omega_\mathrm{B}(\mathbf{r})]/(2\chi N) + \phi_0(x)/2 - \phi_\mathrm{B}(\mathbf{r})|, |[\omega_\mathrm{B}(\mathbf{r}) - \omega_\mathrm{A}(\mathbf{r})]/(2\chi N) + \phi_0(x)/2 - \phi_\mathrm{A}(\mathbf{r})|\}$, is less than ϵ; we take $\epsilon = 10^{-5}$ in all calculations. We also evaluate all integrals using the Romberg integration.[40] These give an accuracy of $< 10^{-3}$ in our f_c. Finally, we minimize f_c with respect to the unconfined dimension(s) in each calculation.

Once the SCF equations are solved, the mean-field free energy (of mixing) per chain of length N can be calculated as $f_c = f_{el} + f_{AB} + f_{sf}$. Here the elastic energy per chain associated with chain conformational entropy is given by

$$f_{el} = -\frac{1}{\bar{\phi}_0 V}\int d\mathbf{r}[\omega_A(\mathbf{r})\phi_A(\mathbf{r}) + \omega_B(\mathbf{r})\phi_B(\mathbf{r})] - \ln Q \tag{3.3}$$

the A-B repulsion per chain is

$$f_{AB} = \frac{\chi N}{\bar{\phi}_0 V}\int d\mathbf{r}\phi_A(\mathbf{r})\phi_B(\mathbf{r}) \tag{3.4}$$

and the surface energy per chain is $f_{sf} = -\Lambda_l S_l - \Lambda_u S_u$, where the surface area per segment at the lower surface

$$S_l = \frac{1}{\bar{\phi}_0 V}\int_0^{\tau} dx \int_0^{L_y} dy \int_0^{L_z} dz \left(1 - \frac{x}{\tau}\right)\phi_0(\mathbf{r})[2\tilde{\phi}_A(\mathbf{r}) - 1] \tag{3.5}$$

and that at the upper surface

$$S_u = \frac{1}{\bar{\phi}_0 V}\int_{D-\tau}^{D} dx \int_0^{L_y} dy \int_0^{L_z} dz \left(1 - \frac{D-x}{\tau}\right)\phi_0(\mathbf{r})[2\tilde{\phi}_A(\mathbf{r}) - 1] \tag{3.6}$$

with the reduced segmental density field of A segments $\tilde{\phi}_A(\mathbf{r}) \equiv \phi_A(\mathbf{r})/\phi_0(\mathbf{r})$; note that a positive S-value corresponds to an A-dominant surface and a negative S-value for a B-dominant surface. The balance among f_{AB}, f_{el} and f_{sf} (in order to minimize f_c) determines the stability of various morphologies obtained.

We further define the reduced A-B interfacial area per segment as

$$\tilde{S}_{\mathrm{AB}} = \frac{1}{\bar{\phi}_0 V} \int \mathrm{d}\mathbf{r} \tilde{\phi}_{\mathrm{A}}(\mathbf{r})[1 - \tilde{\phi}_{\mathrm{A}}(\mathbf{r})] \tag{3.7}$$

and quantify the surface-induced A-B compatibilization by $f_{\mathrm{AB}} - \chi N \tilde{S}_{\mathrm{AB}} \leq 0$. According to our previous study,[19] for confined symmetric diblock copolymers, the surface-induced A-B compatibilization is opposite and comparable in magnitude to the entropic aspect (enrichment of chain ends and depletion of middle segments near a hard surface) of the hard-surface effect.

3.2.2 Chain-End Distribution

We define the distribution function of the $(sN)^{\mathrm{th}}$ segment of a diblock copolymer chain as

$$\rho(\mathbf{r}, s) = \frac{\bar{\phi}_0 q(\mathbf{r}, s) q(\mathbf{r}, 1-s)}{Q \phi_0(x)} \tag{3.8}$$

and $\rho(\mathbf{r}, 0)$ and $\rho(\mathbf{r}, 1)$ give the A-end and B-end distribution respectively, that can be calculated after the SCF equations are solved.

3.3 L_0-Thick Film Between Dissimilar Surfaces

In this Section, we first present our 2D SCF calculations for symmetric diblock copolymers confined between two dissimilar surfaces (i.e., preferring different blocks) separated at $D = L_0$ with the hard surface effect, where several mixed morphologies are found as the surface preferences are varied. We then compare them with 3D SCF calculations without the hard surface effect, where a novel 3D mixed morphology is obtained.

3.3.1 Results with Hard-Surface Effect

Stable Morphologies

Six stable morphologies have been found using our 2D SCF calculations with the hard surface effect, as shown in Fig. 3.1(a). We use the symbol $\|$ to represent perpendicular lamellae, which retains the bulk period L_0. Note that the A-B interfaces in $\|$ are not flat (except when $\Lambda_l = \Lambda_u = 0$) but undulated due to the surface preference.[15,23] $=(1)$ and $=(1.5)$ denote parallel lamellae with 1 and 1.5 periods, respectively. T_1 represents the mixed lamellae with one A-B interface parallel to the surfaces, where the B-rich region is continuous with isolated A-domains near the upper surface. This morphology has been observed in experiments and lattice SCF calculations by Fasolka et al.[29] as a stable phase. Fig. 3.2(a) shows that the lateral period of T_1 is slightly larger than L_0 and decreases with increasing upper surface preference for the B block; Λ_l has little effects on the lateral period of T_1 (data not shown).

T_0 represents another type of mixed lamellae where the A-B interface parallel to the surfaces in T_1 is now absent; that is, the A-rich region is continuous in T_0 with isolated B-domains. T_0 was referred to as the "full capping" perpendicular morphology by Morkved and Jaeger,[35] who used the strong-stretching theory to study the stability of various morphologies in symmetric diblock copolymer thin films (unfortunately not T_0); the energy cost of forming the "full capping" was estimated by Witten using the strong stretching theory.[35] Using SCF calculations in reciprocal space, Masten[15] searched for T_0 between identical surfaces and concluded that it is unstable. Fasolka et al.[29] obtained T_0 as a stable phase between similar surfaces preferring the same block at $D \leq L_0/2$.

We also obtain the morphology of "double mixed lamellae" represented by 2T, which has parallel lamellar orientation near both surfaces but perpendicular in the middle of the film. In this morphology, the A-rich and B-rich regions are bicontinuous and separated by one A-B interface. 2T can be considered as two T_0 structures pieced together, and has not been reported before. Finally, both T_0 and 2T retain the bulk period L_0.

Phase Diagram

Figure 3.1(b) shows our phase diagram for symmetric diblock copolymers confined between two homogeneous, parallel and impenetrable surfaces separated at $D = L_0$, where the upper surface prefers the B block and the lower surface prefers the A block (i.e., $\Lambda_l \geq 0$ and $\Lambda_u \leq 0$). The origin corresponds to two neutral surfaces, and the diagonal line represents the antisymmetric surfaces preferring different blocks with the same strength. The phase diagram is symmetric about the diagonal line and thus only the upper part is shown.

As the surface preference increases, more segments preferred by the surface are drawn to it; the A-B interface close to the surface is therefore changed accordingly. This intuitive argument can be used to qualitatively understand the occurrence of various morphologies in the phase diagram. For example, as both surface preferences increase (e.g., along the direction of the diagonal line in Fig. 3.1(b)), the undulation of the A-B interfaces in $\|$ becomes larger; the A-B interfaces are eventually connected and depart from the surfaces, resulting in the morphological transitions of $\| \rightarrow T_0$ (in the case of asymmetric surfaces where $\Lambda_l \neq -\Lambda_u$) $\rightarrow$ 2T, which are of the second order as elaborated in detail

below. With further increase of (either or both) surface preference, the highly tortuous A-B interface in 2T is squeezed further to the interior of the film and finally transformed to three flat interfaces, leading to the formation of =(1.5). On the other hand, at a strong lower surface preference for the A block Λ_l (e.g., along the vertical line at $\Lambda_l = 25$ in Fig. 3.1(b)), with increasing upper surface preference for the B block the protrusion of B segments through the upper A-rich layer results in the transition of $=(1) \rightarrow T_1$. With further increase of the upper surface preference, which pushes the isolated A-domains towards the lower surface, the A-rich regions are eventually connected, resulting in the transition of $T_1 \rightarrow T_0$. Finally, the transitions of $T_0 \rightarrow 2T \rightarrow =(1.5)$ along this path are similar to those along the diagonal path.

The above intuitive explanation, however, is not quantitative and unambiguous. In the following, we compare the free energies and their components of these morphologies along several paths in the phase diagram to quantitatively elaborate the transitions among various morphologies.

At Constant Upper Surface Preference

Between two neutral surfaces ($\Lambda_l = \Lambda_u = 0$), $\parallel$ is more stable than =(1) in the L_0-thick film due to the surface-induced A-B compatibilization,[15,19] i.e., the decrease of polymer density near the impenetrable surfaces reduces the A-B repulsion and thus favors $\parallel$ with more A-B interfaces near the surfaces over =(1). As Λ_l increases (with $\Lambda_u = 0$), =(1) becomes stable for $\Lambda_l \gtrsim 1.4$ due to its favorable surface energy at the lower surface. This small Λ_l-value at the transition indicates that the hard-surface effect is fairly weak; our previous study shows that it is on the order of a few percent of k_BT per chain.[19] The surface-induced

A-B compatibilization therefore cannot maintain the perpendicular orientation of A-B interfaces near the upper neutral surface when an A-rich parallel layer forms near the lower preferential surface. In other words, for L_0-thick films between one neutral and another preferential surfaces, mixed lamellae with different orientations of A-B interfaces are not stable due to the large free-energy penalty at the T-junction where the different orientations meet.

As the upper surface preference for the B block increases from 0 (i.e., at $\Lambda_u < 0$), in addition to the surface-induced A-B compatibilization, $\|$ further has lower surface energy at the upper surface than $=(1)$. This requires larger Λ_l at the transition and explains the negative slope of the phase boundary between $\|$ and $=(1)$ as shown in Fig. 3.1(b). Due to the increased undulation of A-B interfaces with increasing Λ_l, the A-B interfaces are eventually connected and depart from the lower surface, leading to the formation of T_0 before the transition to $=(1)$ occurs. This is the case around $\Lambda_u = -7$ as shown in Fig. 3.1(b), where T_0 appears as a stable phase in a small window between $\|$ and $=(1)$.

Fig. 3.3 compares the free energies and their components of $\|$, T_0 and $=(1)$ at $\Lambda_u = -7$. We see that $=(1)$ has the lowest elastic energy per chain f_{el} associated with chain conformational entropy, but the highest surface energy per chain f_{sf} due to the unfavorable surface-copolymer interactions at the upper surface. $\|$ has lower A-B repulsion per chain f_{AB} than $=(1)$ due to the surface-induced A-B compatibilization. The inset of Fig. 3.3(b) shows the reduced A-B interfacial area per segment $\tilde{S}_{\mathrm{AB}}$ for these morphologies. In contrary to the perception of strong stretching theory, $\tilde{S}_{\mathrm{AB}}$ for $=(1)$ varies (decreases) with increasing Λ_l, and $\|$ can have smaller $\tilde{S}_{\mathrm{AB}}$ than $=(1)$ (for $\Lambda_l \lesssim 9.4$) despite of its

undulated A-B interfaces. Even when $\|$ has larger $\tilde{S}_{AB}$, its f_{AB} is still smaller than $=(1)$ due to the surface-induced A-B compatibilization. As Λ_l increases, the stronger segregation of A segments to the lower surface (data not shown) leads to the decreased f_{AB} and increased f_{el} in $=(1)$, as well as the decreased f_{sf} in all the morphologies. On the other hand, the increased f_{AB} in $\|$ and T_0 with increasing Λ_l is due to the increased $\tilde{S}_{AB}$ as shown in the inset of Fig. 3.3(b), and their decreased f_{el} is mainly due to the depletion of A-B joints from the lower surface, the distribution of which closely following the A-B interfaces (data not shown).

Finally, as shown in Fig. 3.1(b), there exists a limiting value of $\Lambda_u \approx -7.2$; at stronger preference of the upper surface for the B block, $=(1)$ is no longer the stable morphology no matter how strong the (short-ranged) lower surface preference for the A block is. This is explained below as we discuss the T_1 morphology.

Between Antisymmetric Surfaces

Figure 3.4 compares the free energies of various morphologies ($\|$, 2T, and $=(1.5)$) found between antisymmetric surfaces (i.e., $\Lambda_l = -\Lambda_u$). This case can be compared with that shown in Fig. 3.3. As expected, $=(1.5)$ has the highest f_{AB} due to its large $\tilde{S}_{AB}$, but the lowest f_{el} mainly due to its small lamellar period (chain-stretching) and the lowest f_{sf} due to its favorable surface-copolymer interactions at both surfaces. Similar to the results shown in Fig. 3.3, as the surface preferences increase, the stronger segregation of A and B segments to the corresponding surfaces leads to the decreased f_{AB} in $=(1.5)$ and decreased f_{sf} in all the morphologies (data not shown), as well as the increased f_{el} in both

=(1.5) and 2T (for $\Lambda_l = -\Lambda_u \gtrsim 14.5$). On the other hand, the increased $f_{\rm AB}$ in $\|$ and 2T with increasing surface preferences (data not shown) is due to the increased A-B interfacial area $\tilde{S}_{\rm AB}$ (i.e., undulation of A-B interfaces), and their decreased $f_{\rm el}$ (up to $\Lambda_l = -\Lambda_u \approx 14.5$) is mainly due to the depletion of A-B joints from the surfaces. Overall, the delicate balance among A-B repulsion, chain conformational entropy and surface energy determines the stable regions of these morphologies. In particular, the stability of 2T over =(1.5) (for $12.5 \lesssim \Lambda_l = -\Lambda_u \lesssim 19.8$) is due to its smaller $\tilde{S}_{\rm AB}$. This is different from the case shown in Fig. 3.3, where the lower $f_{\rm sf}$ of $\rm T_0$ is critical to its stability over =(1).

Fig. 3.5 shows the A-B interfaces in $\|$, 2T, and $\rm T_0$. The A-B interfaces in $\|$ (e.g., at $\Lambda_l = -\Lambda_u = 10$) are antisymmetrically undulated due to the surface preferences, and the undulation becomes larger with increasing surface preferences. At $\Lambda_l = -\Lambda_u \approx 12.5$, the two A-B interfaces are connected right at the surfaces. With stronger surface preferences (e.g., at $\Lambda_l = -\Lambda_u = 15$), the connected A-B interface departs from both surfaces forming the 2T morphology. The transition between $\|$ and 2T is therefore of the second order, as indicated by their free energies shown in Fig. 3.4.

From the critical point $\Lambda_l = -\Lambda_u \approx 12.5$, as the upper surface preference for the B block decreases (e.g, at $\Lambda_l = 12.5$ and $\Lambda_u = -11$), the connected A-B interface breaks and intersects the upper surface. Interestingly, the A-B interface near the lower surface remains connected and departs from it, resulting in the $\rm T_0$ morphology. This indicates that the A-B interfaces near the two surfaces are correlated, and explains the negative slope of the phase boundary between $\|$ and $\rm T_0$ shown in Fig. 3.1(b); the transition between these two morphologies is of the

second order, as indicated by their free energies shown in Fig. 3.3. The same applies to the transition between T_0 and 2T, i.e., increasing the lower surface preference for the A block from the critical point also leads to the formation of T_0. Our data indicate that, at the critical point, the phase boundary between $\|$ and T_0 and that between T_0 and 2T shown in Fig. 3.1(b) both have a slope of about -1.

At Constant Lower Surface Preference $\Lambda_l = 25$

Figure 3.6 compares the free energies of various morphologies at $\Lambda_l = 25$, where all the morphologies except $\|$ are obtained as the upper surface preference for the B block is increased from 0. $=(1)$ forms at a neutral or weak upper surface preference due to its favorable surface energy at the lower surface; this morphology also retains the bulk lamellar period at the (small) cost of unfavorable surface energy at the upper surface (when $\Lambda_u < 0$).

At a stronger upper surface preference for the B block (i.e., $\Lambda_u \lesssim -7.2$), T_1 replaces $=(1)$ as the stable phase. This morphology has some B segments present near the upper surface, while maintaining an A-rich parallel layer near the lower surface due to its strong preference for the A block. On the other hand, this A-rich layer effectively screens the strong preference of the lower surface; the phase boundary between T_1 and $=(1)$ is therefore almost independent of Λ_l, as shown in Fig. 3.1(b). This also explains why Λ_l has little effects on the lateral period of T_1. We further note that the parallel A-B interface in T_1 is not perfectly flat, as shown in Fig. 3.1(a), due to the shape of the isolated A-domains near the upper surface. From the free-energy components of T_1 and $=(1)$ shown in Figs. 3.6(b)$-$3.6(d), we see that f_{AB} of both morphologies increase and f_{el}

decrease with increasing upper surface preference $|\Lambda_u|$, due to the increased A-B mixing as more B segments are drawn to the upper surface. On the other hand, while $f_{\rm sf}$ of $\rm T_1$ decreases with increasing $|\Lambda_u|$, that of =(1) exhibits a maximum at $\Lambda_u \approx -9.75$. The inset of Fig. 3.6(d) shows how the surface area per segment at the upper surface S_u varies with Λ_u; clearly, for =(1) the more rapid decrease of S_u with increasing $|\Lambda_u|$ at larger $|\Lambda_u|$ leads to the maximum in its $f_{\rm sf} = -\Lambda_l S_l + |\Lambda_u| S_u$ (S_l is almost independent of Λ_u for both morphologies). Overall, the stability of $\rm T_1$ over =(1) is mainly due to its smaller S_u.

As the upper surface preference for the B block further increases, $\rm T_1$ is replaced by $\rm T_0$ at $\Lambda_u \lesssim -12.7$. Fig. 3.6(e) shows how the free-energy differences between these two morphologies vary with Λ_u. $\rm T_0$ has more B segments present near both surfaces than $\rm T_1$ (i.e., $\rm T_0$ has lower S_u and S_l; data not shown), and the difference $\Delta f_{\rm sf} \equiv f_{\rm sf}^{\rm T_0} - f_{\rm sf}^{\rm T_1}$ is negative and almost constant; the balance between chain elastic energy $f_{\rm el}$ and A-B repulsion $f_{\rm AB}$ therefore determines their stability. While $\rm T_0$ has smaller $\tilde{S}_{\rm AB}$ (data not shown) and thus lower $f_{\rm AB}$ than $\rm T_1$, it has higher $f_{\rm el}$. Overall, however, the difference in $f_{\rm c}$ between these two morphologies is fairly small (less than 0.0092 $k_B T$ per chain in all of our calculations).

The B-rich region near the upper surface in $\rm T_0$ enlarges with increasing upper surface preference for the B block. At $\Lambda_u \approx -15.0$, the adjacent A-B interfaces are connected and depart from the upper surface, and $\rm T_0$ continuously transforms into 2T, as discussed above. Finally, at $\Lambda_u \lesssim -16.8$, =(1.5) becomes more stable than 2T due to its lower $f_{\rm el}$ and $f_{\rm sf}$. We note that the difference in $f_{\rm c}$ between 2T and =(1.5) is also fairly small (less than 0.0109 $k_B T$ per chain in all of our calculations).

3.3.2 Results without Hard-Surface Effect

Phase Diagram

Figure 3.7 shows our phase diagram obtained from 3D calculations without the hard-surface effect (i.e., $\phi_0(\mathbf{r}) = 1$). Several differences are found between this phase diagram and that shown in Fig. 3.1(b): First, the stable region of perpendicular lamellae, which are stabilized mainly by the surface-induced A-B compatibilization, shrinks significantly in Fig. 3.7. Without the hard-surface effect, $\|$ is no longer stable at $\Lambda_u = 0$, except between two neutral surfaces where it degenerates with =(1). As shown in Fig. 3.7, $\|$ is stable only when the two surfaces are nearly antisymmetric with weak preferences.

Second, the absence of the hard-surface effect also makes 2T and T_0 unstable in Fig. 3.7. As indicated in Figs. 3.4 and 3.6, the free-energy differences between 2T, T_0 and =(1.5) are fairly small (less than 0.0263 k_BT per chain) and comparable to the hard-surface effect.[19] Therefore, although 2T and T_0 are obtained in our calculations without the hard-surface effect, they are no longer stable over =(1.5) as explained in detail below.

Third, the Λ-values in Fig. 3.7 are different from those in Fig. 3.1(b), due to the different functional forms of $\phi_0(\mathbf{r})$ used. The surface energy per chain can be re-written as $f_{sf} = -\int d\mathbf{r} H(\mathbf{r})\phi_0(\mathbf{r})[2\tilde{\phi}_A(\mathbf{r}) - 1]/\bar{\phi}_0 V$, from which the effects of different choices of $\phi_0(\mathbf{r})$ on the Λ-values are clear: Under the assumption that the reduced density field of A segments $\tilde{\phi}_A(\mathbf{r})$ remains unchanged for the same morphology, a larger Λ-value is needed in Fig. 3.1(b) (where Eq. (3.2) is used for the hard-surface effect) in order to achieve the same f_{sf} as that in

Fig. 3.7 (without the hard-surface effect); the exact correspondence between the Λ-values in these two cases also depends on $\tilde{\phi}_{\rm A}(\mathbf{r})$ (i.e., the morphology).

The most important difference between our 2D and 3D calculations, however, is that a 3D structure of mixed lamellae, T_1(3D) as shown in Fig. 3.8(b), is found to be stable; accordingly, we refer to the T_1 morphology obtained in our 2D calculations as T_1(2D) hereafter. Similar to T_1(2D), T_1(3D) has a parallel A-B interface near the lower surface, and B segments in the middle of the film also protrude through the upper A-rich layer to reach the upper surface preferring B segments. In T_1(3D), however, these protrusions form hexagonally packed, circular B-domains near the upper surface, instead of B-stripes in T_1(2D) as shown in Fig. 3.8(a). We have not found the similar morphology with circular A-domains near the upper surface.

In our 3D calculations without the hard-surface effect, both T_1(2D) and T_1(3D) are stable phases as shown in Fig. 3.7, where the dotted line represents the phase boundary between T_1(2D) and =(1). We therefore see that T_1(3D) replaces and even enlarges most of the stable region of T_1(2D). Finally, since the A-rich parallel layer near the lower surface effectively screens the lower surface preference, all the phase boundaries between the mixed morphologies (T_1(2D) and T_1(3D)) and the parallel lamellae (=(1) and =(1.5)) are nearly independent of Λ_l. Unlike T_1(2D), the lateral period of T_1(3D) is significantly larger than L_0 as shown in Fig. 3.2(b), which is nearly independent of Λ_l.

Free-Energy Comparisons

Here we quantitatively compare the free energies and their components for various morphologies obtained along three paths in the phase diagram shown in Fig. 3.7.

Fig. 3.9 compares the free energies of ||, =(1), =(1.5) and 2T between antisymmetric surfaces ($\Lambda_l = -\Lambda_u$). =(1) is unstable due to its larger S_u than ||; in other words, the undulation of A-B interfaces in || makes it stable over =(1). As the surface preferences increase, the phase transition of ||→ 2T is still of the second order as discussed above. =(1.5), however, replaces || as the stable phase before this transition occurs. The stability of || and 2T over =(1.5) is solely due to their lower A-B repulsion per chain f_{AB}. Without the surface-induced A-B compatibilization, however, this advantage is not enough to compensate for their higher f_{sf} and elastic energy per chain f_{el} as the surface preferences increase. Effectively, the f_c-curve for || and 2T in Fig. 3.4(a) is shifted upwards (relative to that of =(1.5)) when the hard-surface effect is absent; 2T is therefore no longer stable against =(1.5) in Fig. 3.9. While the hard-surface effect is weak (only a few percent of k_BT per chain), it is comparable to the free-energy difference between 2T and =(1.5) and can thus affect their relative stability.

Similarly, the hard-surface effect can also affect the relative stability of T_0 and =(1.5). Fig. 3.10 compares the free energies of =(1), =(1.5), T_1(2D) and T_0 at $\Lambda_l = 9$. Again, the absence of surface-induced A-B compatibilization effectively shifts the f_c-curves for T_1(2D) and T_0 in Fig. 3.6(a) upwards (relative to those of =(1) and =(1.5)); T_0 is therefore no longer stable over =(1.5) in

Fig. 3.10. As the upper surface preference for the B block increases to $|\Lambda_u| = 8$, T_0 is continuously transformed into 2T, which is also unstable against =(1.5) as explained above.

Finally, Fig. 3.11 compares the free energies of =(1), =(1.5), T_1(2D) and T_1(3D) at $\Lambda_l = 15$. As discussed above, f_{AB} of =(1) and both mixed morphologies increase and f_{el} decrease with increasing upper surface preference $|\Lambda_u|$, due to the increased A-B mixing as more B segments are drawn to the upper surface. In the case of =(1.5), however, A-B mixing is actually reduced as more B segments are drawn to the upper surface, and we thus see the opposite trends. The behaviors of f_{sf} of these morphologies are similar to those shown in Fig. 3.6(d) and can be understood accordingly. On the other hand, the mixed morphologies exhibit intermediate values between =(1) and =(1.5) in all three free-energy components, indicating that their formation is due to the subtle balance among these factors. In particular, the stability of T_1(2D) and T_1(3D) over =(1.5) is due to their smaller $\tilde{S}_{AB}$, while their stability over =(1) is mainly due to their smaller S_u. Furthermore, the stability of T_1(3D) over T_1(2D) is due to its smaller $\tilde{S}_{AB}$. To the best of our knowledge, T_1(3D) has not been reported before.

3.4 *Effects of Film Thickness*

In the previous section, we have examined in detail the structure and stability of various morphologies in L_0-thick films confined between dissimilar surfaces. In particular, while the formation of 2T and T_0 is affected by the hard-surface effect, T_1(2D) and T_1(3D) are not. We therefore investigate in this Section

the effects of film thickness on various morphologies of symmetric diblock copolymers confined between dissimilar surfaces, with a strong preference of the lower surface for the A block (i.e., $\Lambda_l = 15$) and without the hard-surface effect.

Figure 3.12 shows the phase diagram as a function of upper surface preference for the B block $\Lambda_u \leq 0$ and the film thickness D. As D increases from L_0, the stable regions of $=(1)$ and mixed morphologies (T_1(3D) and T_1(2D)) shrink while that of $=(1.5)$ grows, and at $D \gtrsim 1.22L_0$ $=(1.5)$ becomes the only stable morphology. Fig. 3.13 shows how the free energies and their components for the parallel lamellae ($=(1)$ and $=(1.5)$) and mixed morphologies vary with D at $\Lambda_u = -3.3$, where T_1(2D) is unstable. As in the case of $D = L_0$ discussed above, the mixed morphologies have intermediate values between $=(1)$ and $=(1.5)$ in all the free-energy components, indicating that their formation is due to the subtle balance among these factors. In both parallel lamellae, increasing D leads to stronger segregation between A and B segments (thus decreasing A-B repulsion per chain f_{AB}) and stronger chain-stretching (thus increasing elastic energy per chain f_{el}). While the upper surface-copolymer interfacial area per substrate area S_uD in $=(1)$ slightly increases with increasing D due to the stronger A-B segregation (thus more A segments present near the upper surface), S_uD in $=(1.5)$ decreases due to more B segments present near the upper surface. The latter also occurs more noticeably in both T_1(2D) and T_1(3D) as shown in Fig. 3.13(d), due to the alleviated frustration (thus decreased f_{el}) in the mixed morphologies with increasing D, which *effectively* makes the upper surface more preferential to the B block in the mixed morphologies; the transitions of $=(1)\rightarrow T_1$(3D) and T_1(3D)$\rightarrow T_1$(2D) therefore occur at smaller $|\Lambda_u|$ with increasing D, as shown in Fig. 3.12.

As D further increases towards $2L_0$, =(1.5) is replaced by =(2) at small $|\Lambda_u| \lesssim 2.25$ and by =(2.5) at large $|\Lambda_u| \gtrsim 6.1$. Compared to =(1.5), =(2) has lower $f_{\rm el}$ but higher $f_{\rm AB}$ and $f_{\rm sf}$. The unfavorable surface energy at the upper surface in =(2) makes it less stable as the upper surface preference for the B block $|\Lambda_u|$ increases; the phase boundary between =(1.5) and =(2) shown in Fig. 3.12 therefore has a negative slope. On the other hand, the phase boundary between =(1.5) and =(2.5) (at $D \approx 1.925L_0$) is virtually independent of Λ_u, because their $f_{\rm sf}$ are almost identical and their difference in $f_{\rm AB}$ is nearly constant; D (i.e., $f_{\rm el}$) is therefore the only factor determining their relative stability.

At intermediate upper surface preference for the B block (i.e., $2.25 \lesssim |\Lambda_u| \lesssim 6.1$), =(1.5) is replaced by T_1(2D) as D increases towards $2L_0$. This T_1(2D) structure shown in Fig. 3.8(f), compared to that at $D \approx L_0$ shown in Fig. 3.8(a), has prolonged perpendicular A-B interfaces in the film, which help to alleviate the frustration in the mixed morphology. As shown in Fig. 3.2(a), the period of T_1(2D) at $D = 2L_0$ is closer to the bulk lamellar period L_0 than that of T_1(2D) at $D = L_0$. This is because the free-energy penalty at the end-cap of the T-junction in T_1(2D) is alleviated with increasing D; the upper part of the film therefore resembles more like the perpendicular lamellae with L_0. Some undulations of perpendicular A-B interfaces, however, are still seen near the upper surface due to its preference for the B block.

While T_1(2D) is the only stable mixed morphology we have found at $D \approx 2L_0$, T_2(2D), T_3(2D) and T_3(3D) were also obtained in our calculations, as shown

in Figs. 3.8(g)~3.8(i) respectively, and their lateral periods are shown in Fig. 3.2. T_2(2D) has two parallel A-B interfaces in the lower part of the film and continuous A-domains in the upper part of the film, while T_3(2D) has three parallel A-B interfaces in the lower part of the film and continuous B-domains in the upper part of the film. T_3(3D) has three parallel A-B interfaces in the lower part of the film, and hexagonally packed circular B-rich domains protruding through the upper A-rich layer to reach the upper surface preferring B segments. The upper half of T_3(2D) and T_3(3D) is very similar to T_1(2D) and T_1(3D), respectively, found at $D \approx L_0$.

Figure 3.14 shows how the free energies and their components for the parallel lamellae (=(2) and =(2.5)) and four mixed morphologies (T_1(2D), T_2(2D), T_3(2D) and T_3(3D)) vary with Λ_u at $D = 2L_0$. These results are analogous to those in the $D = L_0$ case shown in Fig. 3.11 and can be understood accordingly. Overall, the stability of T_1(2D) over =(2.5) is due to its smaller $\tilde{S}_{AB}$, while its stability over =(2) is mainly due to its smaller S_u, as in the $D = L_0$ case. However, T_2(2D), T_3(2D) and T_3(3D) are all found to be unstable at $D = 2L_0$. In particular, the advantage of the 3D mixed morphology T_3(3D) in f_{AB} over T_1(2D) shown in Fig. 3.14(b) is less significant than that of T_1(3D) in the $D = L_0$ case shown in Fig. 3.11(b), since there are three parallel A-B interfaces in T_3(3D). Similarly, within the stability window of T_1(2D) at $D = 2L_0$ ($3.05 \lesssim |\Lambda_u| \lesssim 3.55$), T_2(2D) and T_3(2D) have higher f_{AB} than T_1(2D). Finally, T_1(2D) has the additional advantage in S_u over other mixed morphologies, due to its prolonged perpendicular A-B interfaces which alleviate the free-energy penalty of the T-junctions.

3.5 $1.5L_0$-Thick Film Between Similar Surfaces

As shown in Fig. 3.12, =(1.5) is the only stable morphology in thin films confined between two dissimilar surfaces separated at $D \approx 1.5L_0$. For such film thickness, it would be more interesting to investigate the phase behavior of symmetric diblock copolymer thin films confined between two similar surfaces preferring the same block. In this Section we set $D = 1.5L_0$ and $\Lambda_l = 15$, and vary the upper surface preference for the A block $\Lambda_u \geq 0$.

In addition to parallel lamellae of =(1.5) and =(2), three mixed morphologies (T_1(2D), T_2(2D), and T_2(3D)) as shown in Fig. 3.8(c)~3.8(e) are found in our calculations. Figure 3.15 shows how the free energies and their components for these morphologies vary with Λ_u. These results are again analogous to those in the $D = L_0$ case shown in Fig. 3.11, except that =(1) and =(1.5) in that case are replaced by, respectively, =(1.5) and =(2) here due to the different film thicknesses and the upper surface preferences for different blocks. Accordingly, T_1(3D) in that case is replaced by T_2(3D) here. Comparing Figs. 3.11(a) and 3.15(a), we see that the overall stable region of mixed morphologies shrinks as D increases, consistent with the phase diagram shown in Fig. 3.12. In addition, the stable region of T_2(3D) is much smaller than that of T_1(3D), giving way to T_1(2D). This is again consistent with Fig. 3.12. On the other hand, T_2(2D) is found to be unstable against T_1(2D) due to its higher f_{AB} (one more parallel A-B interface) and f_{sf} (more B segments present near the upper surface because the T-junctions are closer to it). This is consistent with the T_1(2D) and T_2(2D) shown in Fig. 3.14.

Finally, we note that the mixed morphologies at different D are closely related. For example, as shown in Fig. 3.8, T_2(2D) at $D = 1.5L_0$ can be regarded as adding a parallel A-B lamella to the lower part of T_2(2D) at $D = L_0$, then with the A and B in the entire structure switched to comply with the strong lower surface preference for the A block; repeating this one more time results in T_3(2D) at $D = 2L_0$. We further note that the lateral periods of these three morphologies are close to each other, as shown in Fig. 3.2(a). The same applies to the group of T_1(2D) at $D = 1.5L_0$ and T_2(2D) at $D = 2L_0$, and that of all the 3D mixed morphologies shown in Fig. 3.8.

3.6 Conclusion

We have conducted a comprehensive study on the phase behavior of symmetric diblock copolymers under planer confinement. With the so-called hard-surface effect considered, our two-dimensional calculations show that mixed lamellae T_1(2D), T_0 and 2T can be stable under certain conditions. Our study unveils the intricate interplay of A-B repulsion, surface preference and chain entropy. Each stable morphology results from delicate balance among these effects. While the T_1(2D) structure was also reported by Fasolca et al., T_0 and 2T are new morphologies not reported by other and deserve a closer study by both experiments and molecular simulations. The formation of these two structures is due to the hard-surface effects preferring more A-B mixing near the surfaces. But the hard-surface effects are only profound when the confining surfaces are neutral or have weak preference. This means that with stronger surface preference the two structures become less stable. This trend can be seen from Figure 3.1(a), where the stable regions of T_0 and 2T shrink to the right of the diagram. Quite oppositely,

the stable region of $T_1(2D)$ expands as Λ_A becomes even more mismatched with Λ_B, and this tells that the formation of $T_1(2D)$ structure has nothing to do with the hard-surface effects but instead due to the mismatch of the two surface preferences. We therefore also performed 3D calculations without the hard-surface effects, where novel three-dimensional structures corresponding to the $T_1(2D)$ in the 2D calculations are found.

List of Figures

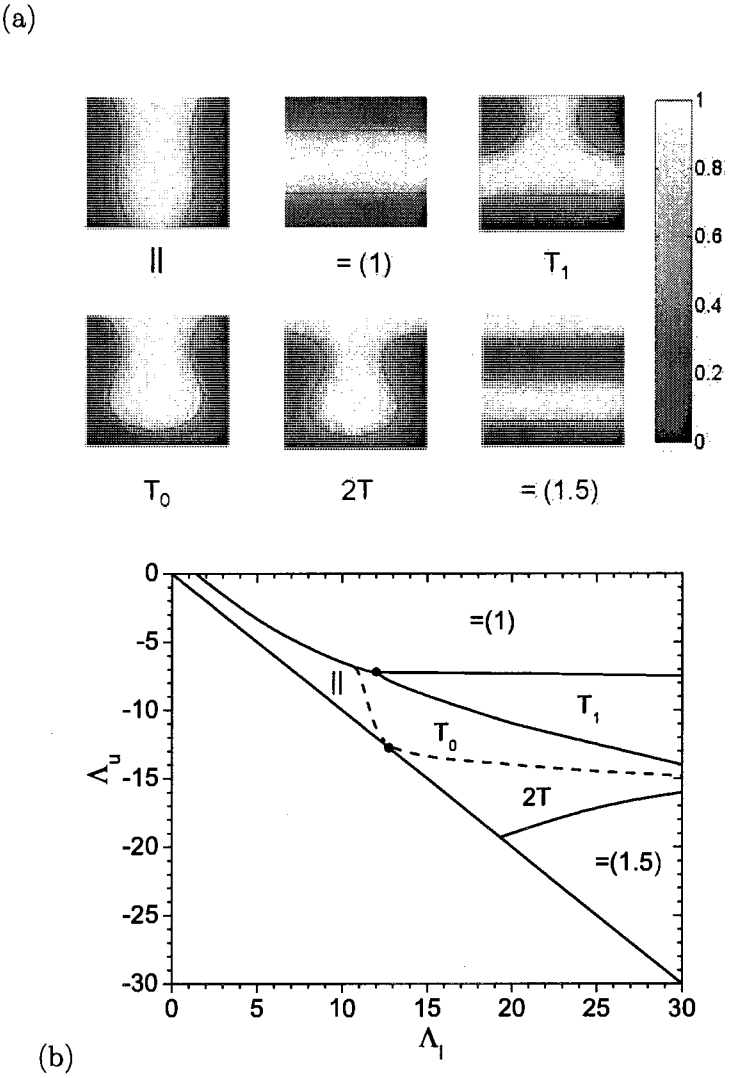

Fig. 3.1: (a) Phase diagram for symmetric diblock copolymers confined between two parallel and impenetrable surfaces, at $\chi N = 15$ and $D = L_0$, obtained from 2D Dirichlet B.C. calculations. The lower surface prefers A and the upper surface prefers B. (b) Typical density profiles of various morphologies at different surface preference. $\|$ $(\Lambda_l = 5, \Lambda_u = -5)$; $=(1)$ $(\Lambda_l = 10, \Lambda_u = -10)$; T_1 $(\Lambda_l = 20, \Lambda_u = -10)$; T_0 $(\Lambda_l = 15, \Lambda_u = -10)$; $2T$ $(\Lambda_l = 17, \Lambda_u = -17)$; $=(1.5)$ $(\Lambda_l = 25, \Lambda_u = -25)$. The scale bar corresponds to $\phi_B(\mathbf{r})/\phi_0(\mathbf{r})$, and the solid curves mark the A-B interfaces (where $\phi_A(\mathbf{r}) = \phi_B(\mathbf{r})$) in each morphology. See text for details.

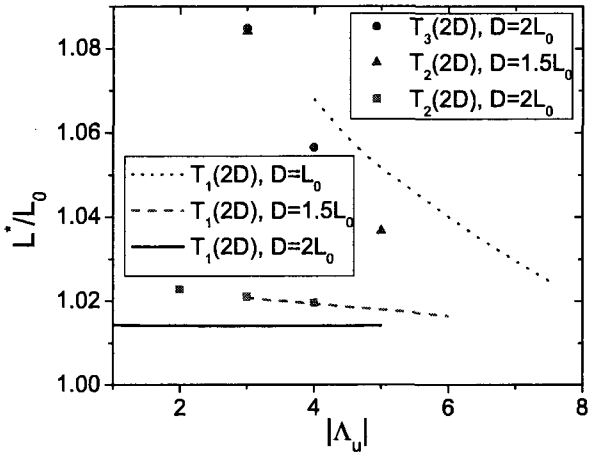

(a)

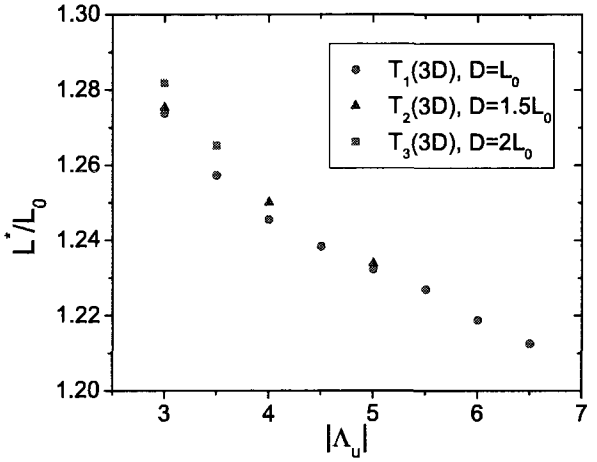

(b)

Fig. 3.2: (a) The periods of two dimensional mixed morphologies are slightly larger than the bulk lamellar period L_0 and vary with the preferential strength of the surfaces. (b) The periods of three dimensional morphologies are significantly larger than the bulk lamellar period L_0, same as in two dimensional mixed morphologies they also vary with the preferential strength of the surfaces.

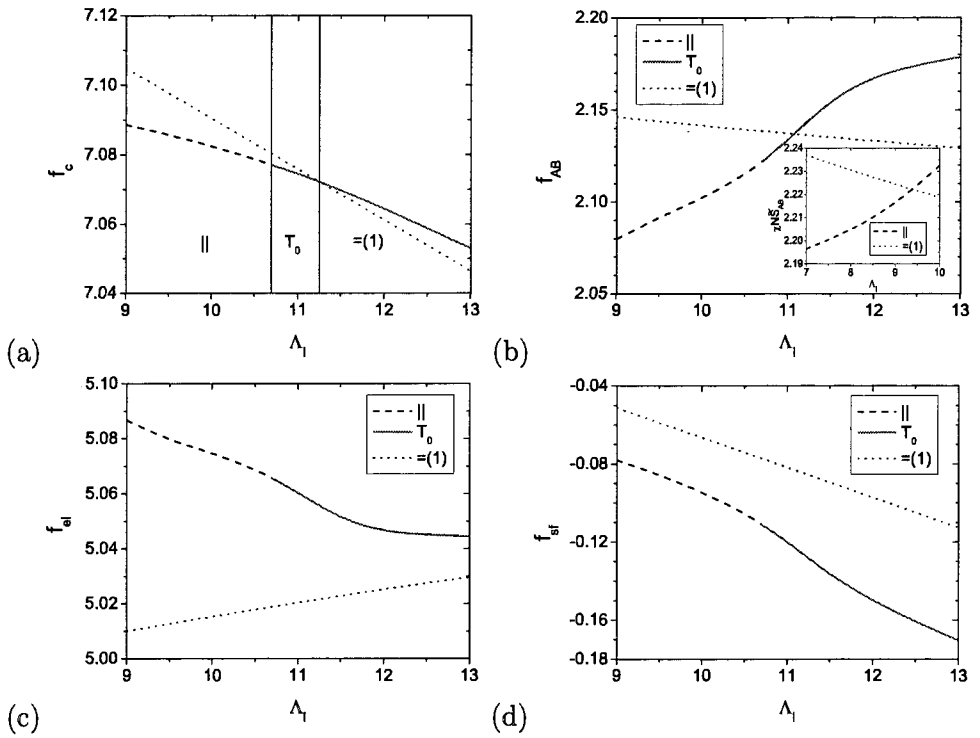

Fig. 3.3: (a) Free energies and their components comparison of $\|$, T_0 and $=(1)$ at $\Lambda_u = -7$. The vertical line represents the phase boundary, and the stable morphology (having the lowest free energy) is indicated in each region.

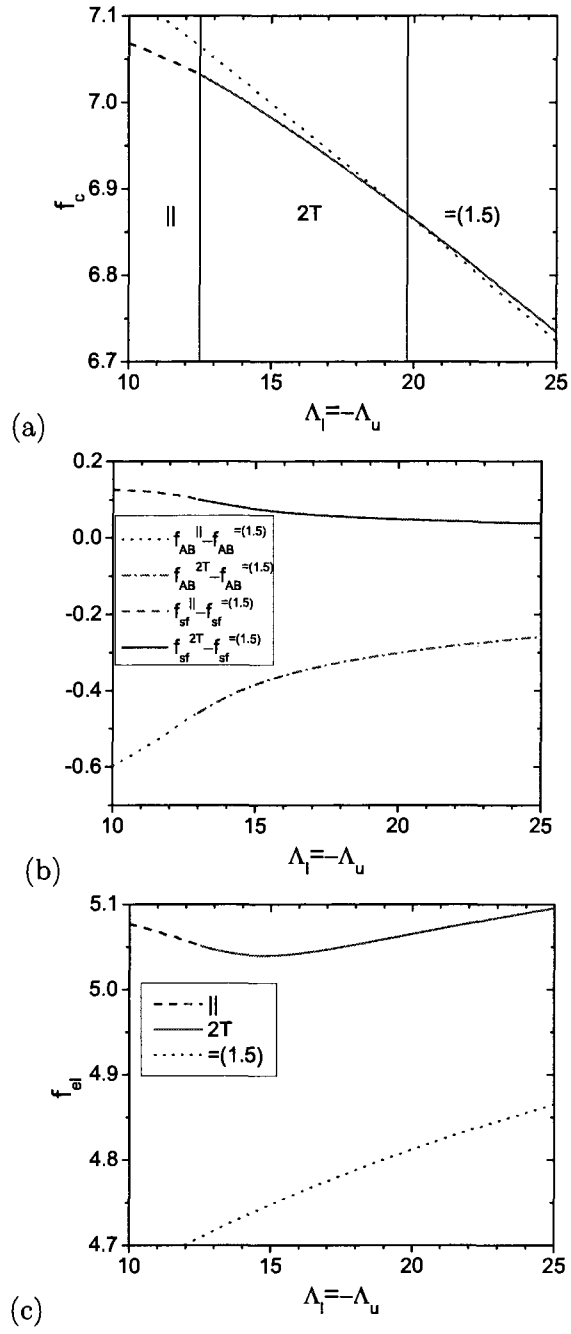

Fig. 3.4: (a) Free energies and their components of ||, 2T and = (1.5) between antisymmetric surfaces. The vertical line represents the phase boundary, and the stable morphology (having the lowest free energy) is indicated in each region.

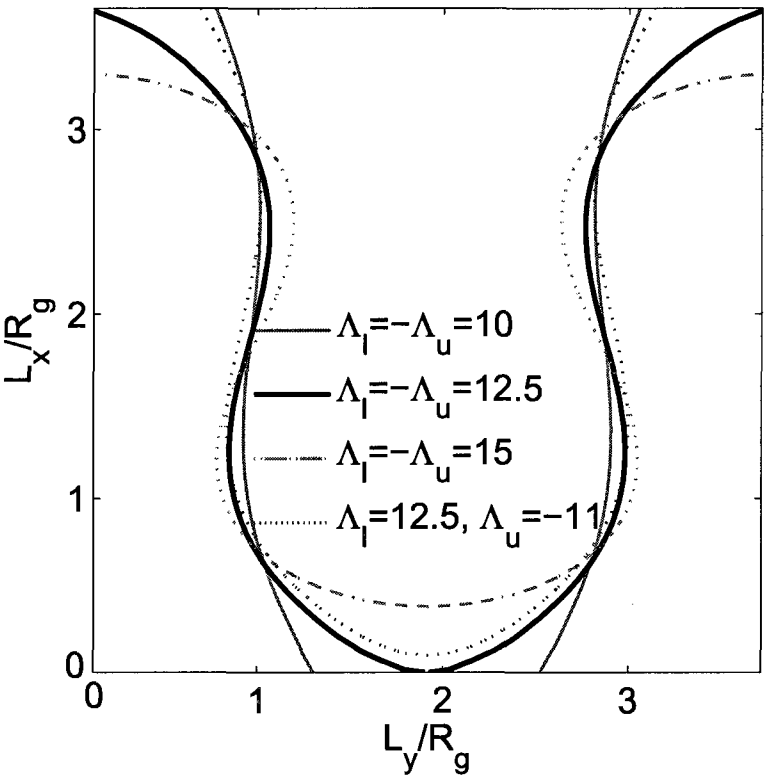

Fig. 3.5: A-B interfaces near the critical point at $\Lambda_l = -\Lambda_u = 12.5$ (corresponding to the solid curve).

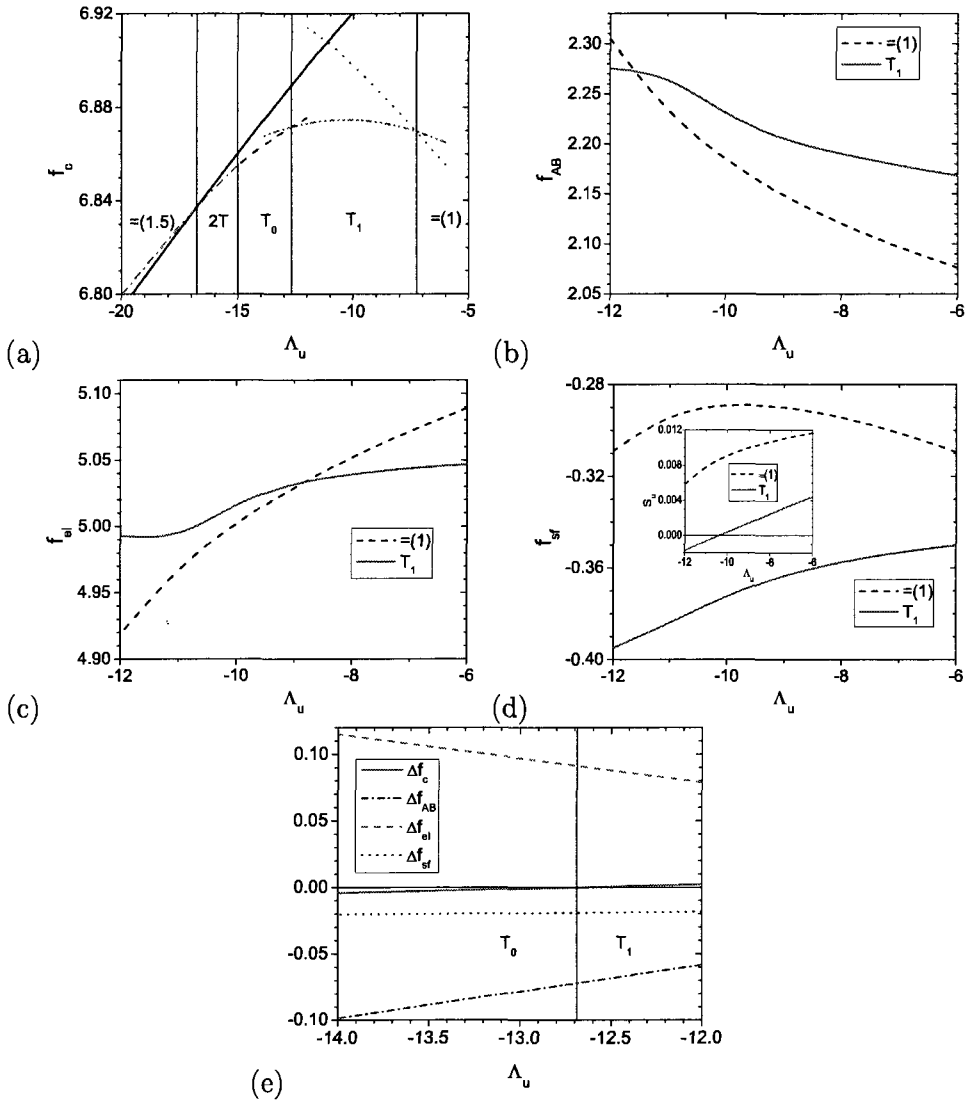

Fig. 3.6: (a) Free energy comparison of various morphologies obtained at $\Lambda_l = 25$. The vertical line represents the phase boundary, and the stable morphology (having the lowest free energy) is indicated in each region. (b),(c), (d) Comparison of free energy components between = (1) and T_1 (e) Contributions from chain entropy (Δf_{el}), A-B interactions (Δf_{AB}) and block-surface interactions (Δf_{surf}) to the free-energy difference between the T_1 and T_0 morphologies ($\Delta f_c \equiv f_c^{T_0} - f_c^{T_0}$) at $\Lambda_l = 25$. The vertical line represents the phase boundary.

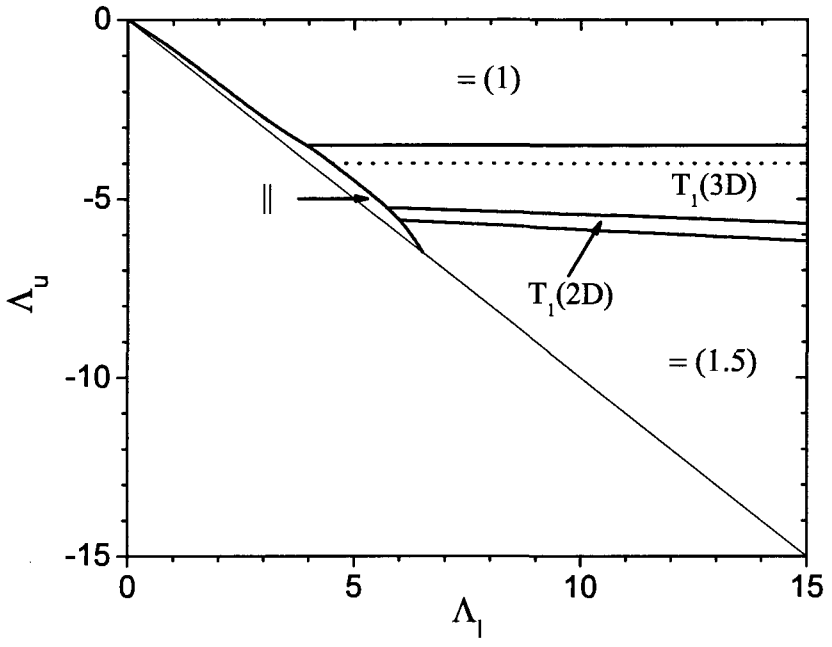

Fig. 3.7: Phase diagram for symmetric diblock copolymers confined between two parallel and impenetrable surfaces, at $\chi N = 15$ and $D = L_0$, obtained from three dimensional calculations without considering the hard-surface effects. The lower surface prefers A and the upper surface prefers B.

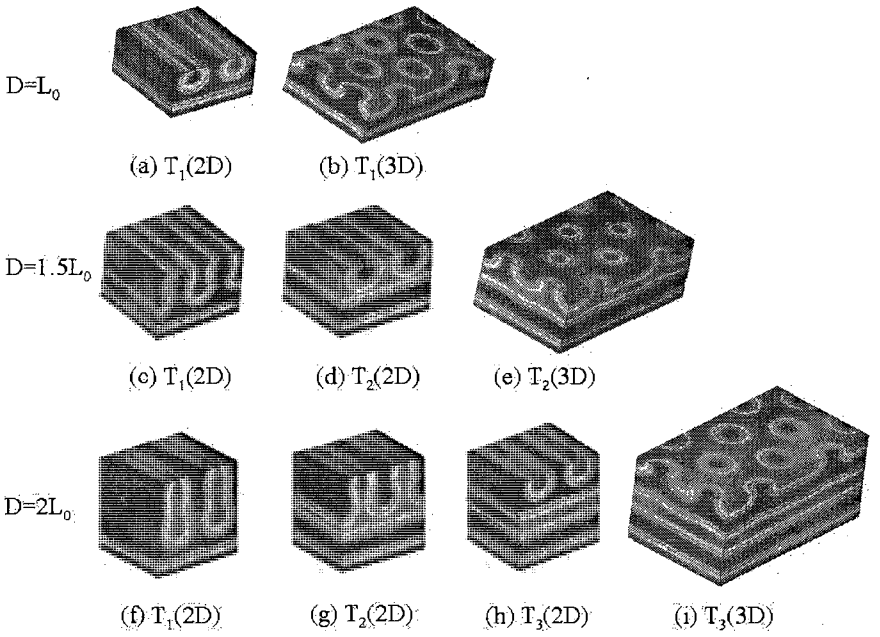

Fig. 3.8: Density profiles of the mixed morphologies found from three dimensional calculations without hard-surface effects: (a) $\Lambda_l = 15, \Lambda_u = -6$ (b) $\Lambda_l = 15, \Lambda_u = -5$ (c) $\Lambda_l = 15, \Lambda_u = 4$ (d) $\Lambda_l = 15, \Lambda_u = 3$ (e) $\Lambda_l = 15, \Lambda_u = 3$ (f) $\Lambda_l = 15, \Lambda_u = -3$ (g) $\Lambda_l = 15, \Lambda_u = -3$ (h) $\Lambda_l = 15, \Lambda_u = -3$ (i) $\Lambda_l = 15, \Lambda_u = -3$.

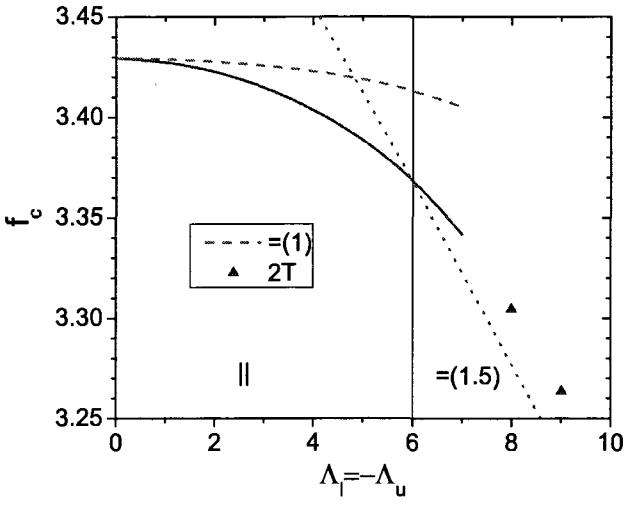

Fig. 3.9: Free energies of = (1), || and 2T between antisymmetric surfaces.

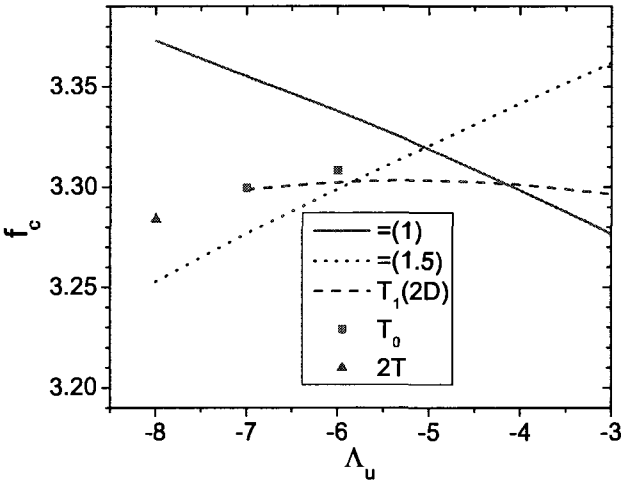

Fig. 3.10: Free energies of morphologies obtained with $\Lambda_l = 9$ where T_0 and 2T are observed but no longer stable.

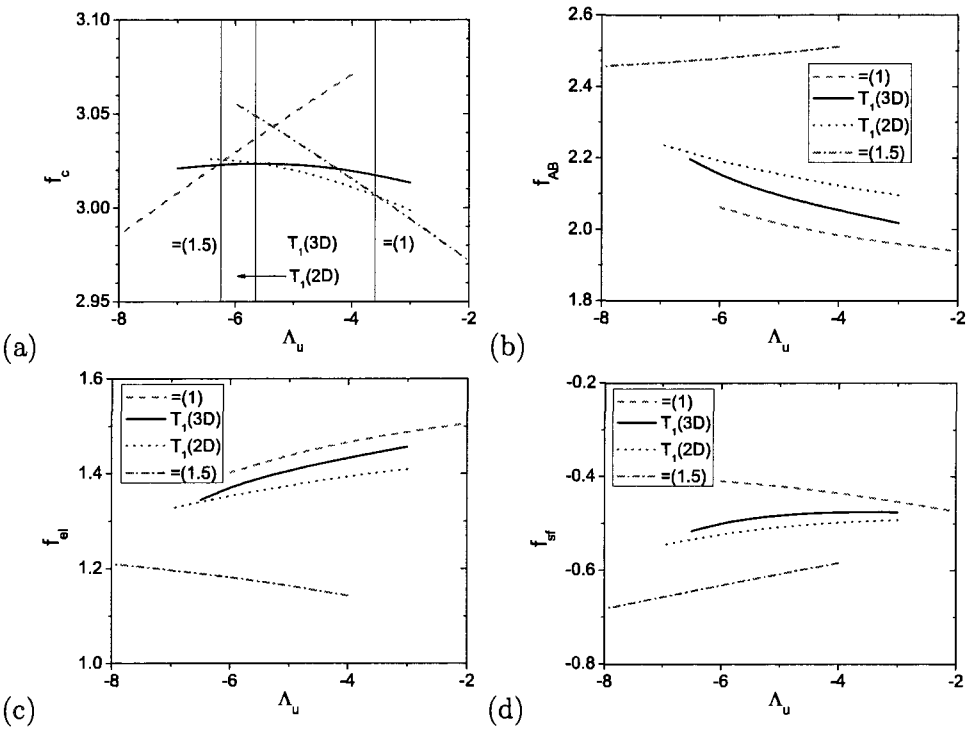

Fig. 3.11: (a) Free energy comparison of various morphologies obtained at $\Lambda_l = 15$. The vertical line represents the phase boundary, and the stable morphology (having the lowest free energy) is indicated in each region. (b), (c), (d) Compares the free energy components f_{AB}, f_{el} and f_{sf} of different morphologies obtained at $\Lambda_l = 15$.

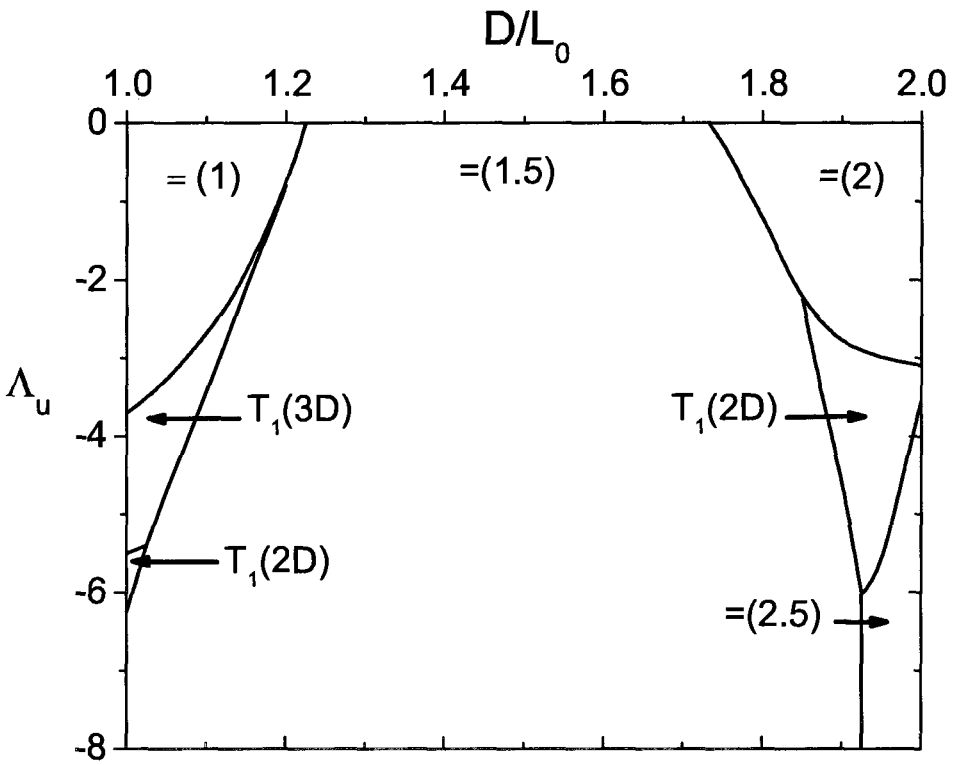

Fig. 3.12: Phase diagram for symmetric diblock copolymers confined between two parallel and impenetrable surfaces, at $\chi N = 15$ and $\Lambda_l = 15$, obtained from three dimensional calculations without hard-surface effects. The lower surface prefers A and the upper surface prefers B.

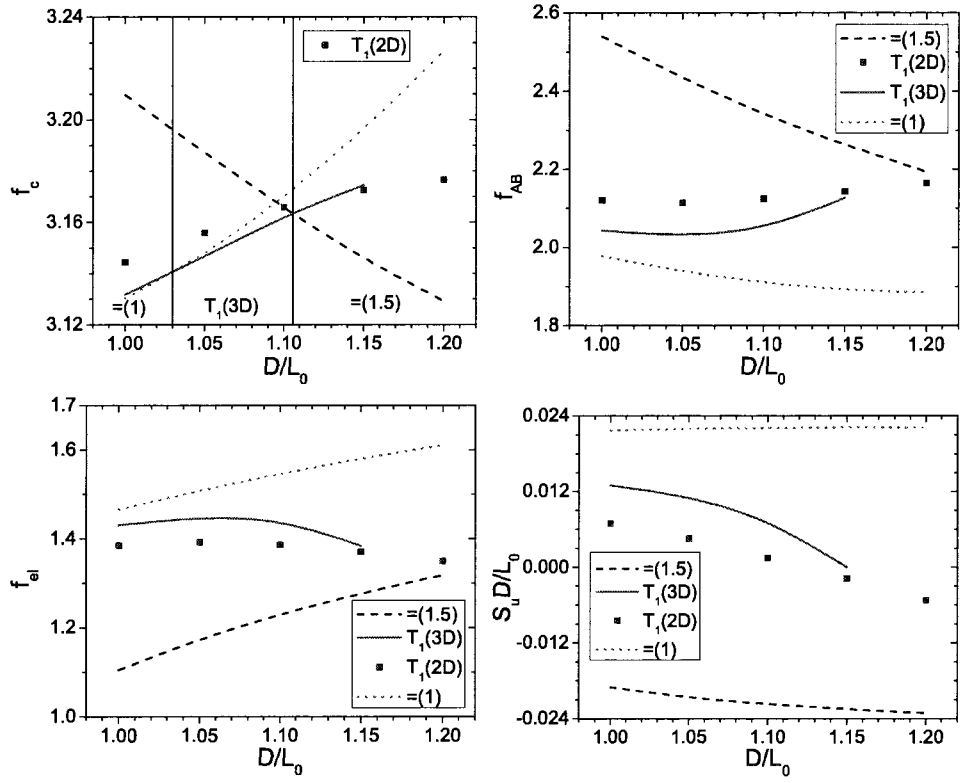

Fig. 3.13: (a) Free energy comparison of various morphologies obtained at $\Lambda_l = 15$, $\Lambda_u = -3.3$ with film thickness varied from L_0 to $1.2L_0$. The vertical line represents the phase boundary, and the stable morphology (having the lowest free energy) is indicated in each region. (b), (c) compares free energy components f_{AB}, f_{el}. (d) shows the surface area per segment near the upper surface.

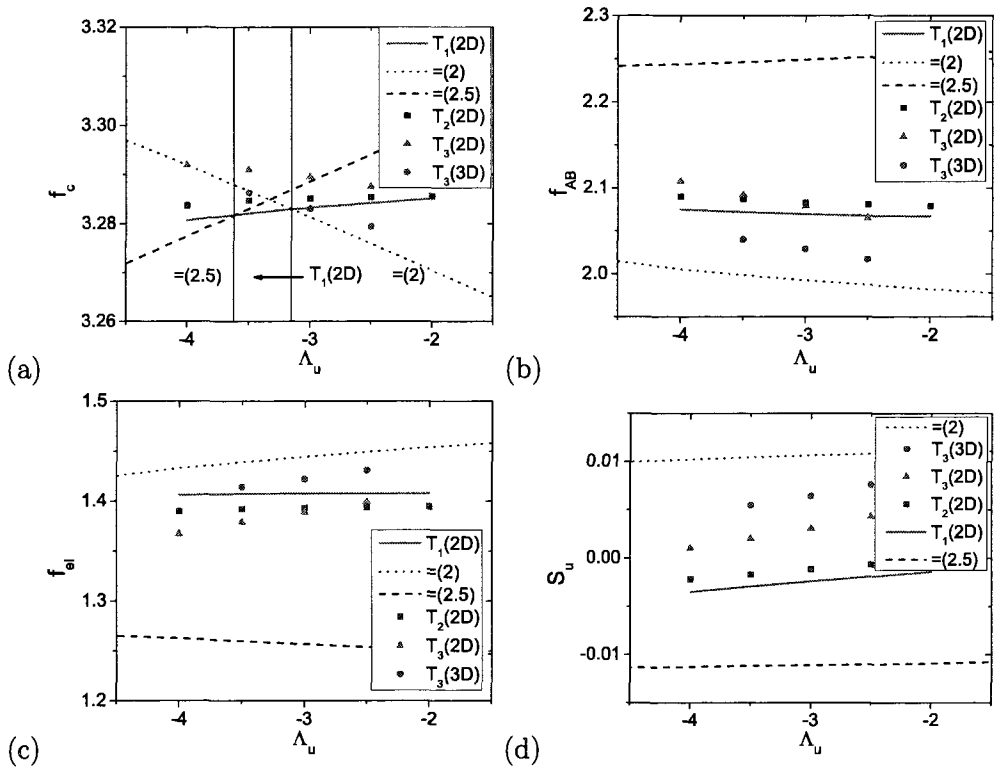

Fig. 3.14: (a) Free energy comparison of various morphologies obtained at $\Lambda_l = 15$, $D = 2L_0$. The vertical line represents the phase boundary, and the stable morphology (having the lowest free energy) is indicated in each region. (b), (c), (d) compares free energy components f_{AB}, f_{el} and f_{sf} of these morphologies. (e) shows the surface area per segment near the upper surface

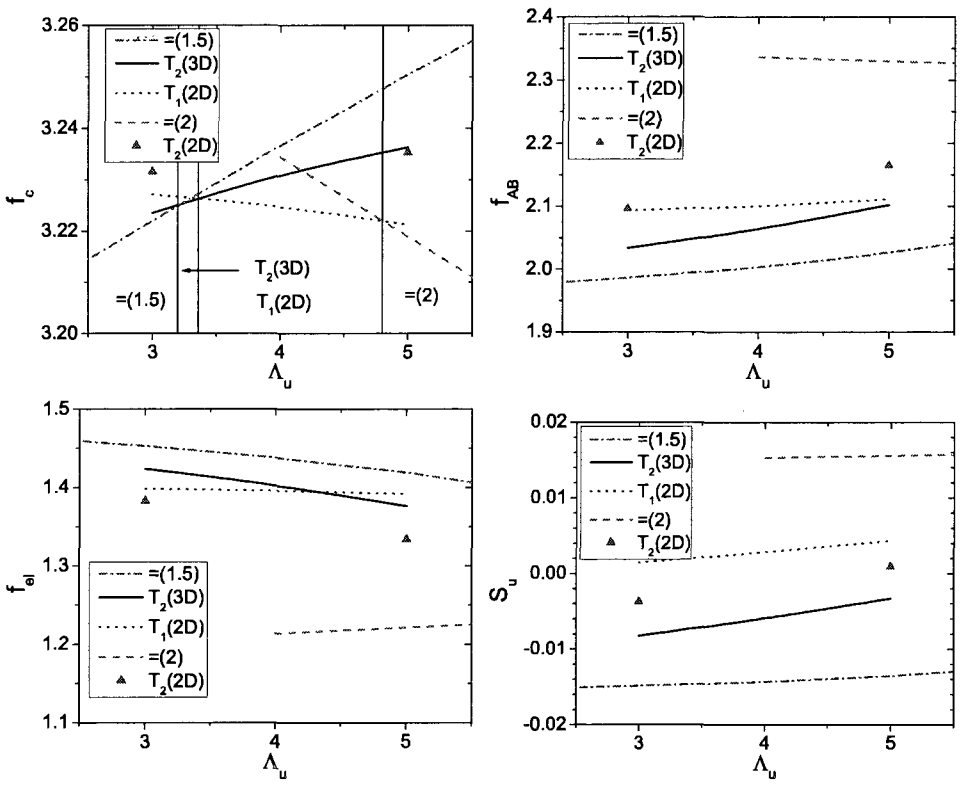

Fig. 3.15: (a) Free energy comparison of various morphologies obtained at $\Lambda_l = 15$, $D = 1.5L_0$. The vertical line represents the phase boundary, and the stable morphology (having the lowest free energy) is indicated in each region. (b), (c), (d) compares free energy components f_{AB}, f_{el} and f_{sf} of these morphologies.

BIBLIOGRAPHY

[1] F. S. Bates and G. H. Fredrickson, Annu. Rev. Phys. Chem., **41**, 525 (1990).

[2] F. S. Bates and G. H. Fredrickson, Phys. Today, **52**, 32 (1999).

[3] M. W. Matsen and M. Schick, Phys. Rev. Lett., **72**, 2660 (1994).

[4] M. S. Turner, Phys. Rev. Lett., **69**, 1788 (1992).

[5] D. G. Walton, G. J. Kellogg, A. M. Mayes, P. Lambooy and T. P. Russell, Macromolecules, **27**, 6225 (1994).

[6] P. Lambooy, T. P. Russell, G. J. Kellogg, A. M. Mayes, P. D. Gallagher and S. K. Satija, Phys. Rev. Lett., **72**, 2899(1994).

[7] T. P. Russell, P. Lambooy, G. J. Kellogg and A. M. Mayes, Physica B, **213**, 22 (1995).

[8] N. Koneripalli, N. Singh, R. Levicky, F. S. Bates, P. D. Gallagher and S. K. Satija, Macromolecules, **28**, 2897 (1995).

[9] M. Kikuchi and K. J. Binder, Chem. Phys., **101**, 3367 (1994).

[10] Q. Wang, Q. L. Yan, P. F. Nealey and J. J. de Pablo, J. Chem. Phys., **112**, 450 (2000).

[11] J. Feng, H. L. Liu and Y. Hu, Macromol. Theory Simul., **11**, 549 (2002).

[12] J. Feng, H. L. Liu, Y. Hu and J. M. Prausnitz, J. M. Chem. Eng. Sci., **59**, 1701 (2004).

[13] K. R. Shull, Macromolecules, **25**, 2122 (1992).

[14] K. Y. Wong, M. Trache and W. E. McMullen, J. Chem. Phys., **101**, 5372 (1994).

[15] M. W. Matsen, J. Chem. Phys., **106**, 7781 (1997).

[16] W. A. M. Morgado, S. Martins, M. Bahiana and M. S. O. Massunaga, Physica A, **283**, 208 (2000).

[17] Y. Tsori and D. Andelman, Eur. Phys. J. E, **5**, 605 (2001).

[18] A. L. Frischknecht, J. G. Curro, and L. J. D. Frink, J. Chem. Phys., **117**, 10398 (2002).

[19] D. Meng and Q. Wang, J. Chem. Phys., **126**, 234902 (2007).

[20] G. J. Kellogg, D. G. Walton, A. M. Mayes, P. Lambooy, T. P. Russell, P. D. Gallagher and S. K. Satija, Phys. Rev. Lett., **76**, 2503 (1996).

[21] N. Koneripalli, R. Levicky, F. S. Bates, J. Ankner, H. Kaiser and S. K. Satija, Langmuir, **12**, 6681 (1996).

[22] E. Huang, T. P. Russell, C. Harrison, P. M. Chaikin, R. A. Register, C. J. Hawker and J. Mays, Macromolecules, **31**, 7641 (1998).

[23] T. Geisinger, M. Muller and K. J. Binder, Chem. Phys., **111**, 5241 (1999).

[24] T. Geisinger, M. Muller and K. J. Binder, Chem. Phys., **111**, 5251 (1999).

[25] G. Brown and A. Chakrabarti, J. Chem. Phys., **102**, 1440 (1995).

[26] M. S. Turner, A. Johner and J. F. Joanny, J. Phys. I, **5**, 917 (1995).

[27] G. T. Pickett and A. C. Balazs, Macromolecules, **30**, 3097 (1997).

[28] W. H. Tang, Macromolecules, **33**, 1370 (2000).

[29] M. J. Fasolka, P. Banerjee, A. M. Mayes, G. Pickett and A. C. Balazs, Macromolecules, **33**, 5702 (2000).

[30] P. Mansky, T. P. Russell, C. J. Hawker, M. Pitsikalis and J. Mays, Macromolecules, **30**, 6810 (1997).

[31] E. Huang, P. Mansky, T. P. Russell, C. Harrison, P. M. Chaikin, R. A. Register, C. J. Hawker and J. Mays, Macromolecules, **33**, 80 (2000).

[32] B. H. Sohn and S. H. Yun, Polymer, **43**, 2507 (2002).

[33] J. U. Sommer, A. Hoffann and A. Blumen, J. Chem. Phys., **111**, 3728 (1999).

[34] T. P. Russell, A. Menelle, S. H. Anastasiadis, S. K. Satija and C. F. Majkrzak, Macromolecules, **24**, 6263 (1991).

[35] T. L. Morkved and H. M. Jaeger, Europhys. Lett., **40**, 643 (1997).

[36] Wang, Q. Ph.D. Dissertation: Molecular Study of The Structure and Morphology of Diblock Copolymers on Nano-Patterned Substrates".

[37] E. W. Cochran, C. J. Garcia-Cervera and G. H. Fredrickson, Macromolecules, **39**, 2449 (2006).

[38] G. Tzeremes, K. O. Rasmussen, T. Lookman and A. Saxena, Phys. Rev. E, **65**, 041806 (2002).

[39] H. D. Ceniceros and G. H. Fredrickson, Multiscale Modeling and Simulation, **2**, 452 (2004).

[40] W. H., S. A. Teukolsky, W. T. Vetterling and B. P. Flannery, "Numerical Recipes (Chapter 4)", Cambridge University Press, 1992.

4. SELF-ASSEMBLY OF DIBLOCK COPOLYMERS ON NANO-PATTERNED SUBSTRATES

4.1 Introduction

Establishing a robust and versatile nanopatterning process has been a central issue in nanotechnology.[1–3] Molecular selfassembly has several advantages over other methods, in that molecular building blocks ensure ultrafine pattern precision, parallel structure formation allows for mass production, and a variety of three-dimensional (3D) structures are available for fabricating complex structures.[4] Block copolymers are representative such self-assembling materials extensively utilized in nanofabrication.[5–12] In contrast to colloid assembly or anodized metal oxides, various shapes of nanostructures, including lines or interconnected networks, can be generated with a precise tunability of shape and size. However, the interaction for block copolymers self-assembly generally relies on weak forces such as van der Waals forces and hydrogen bonding[13] that are readily influenced by thermal fluctuation. As a result the structure formation is usually slow and the degree of ordering is low in an assembled structure. To promote self-assembly and as well to modify the block copolymer nanostructures, pre-defined guiding patterns containing chemical and/or nanostructured topographical contrast are typically used. These approaches provide additional driving forces for structure formation as well as guiding the assembly of block

copolymers such that a highly ordered assembled structure is expected over an arbitrarily large area.

In collaboration with experimental investigations, in the following two sections, we will study from a computational standpoint the bending property of lamellae resulting from directed assembly of symmetric diblock copolymers (DBC) using topographic guiding patterns; and novel complex structures formed by cylinder forming DBC on chemical patterned flat substrate respectively .

4.2 *Bending of Lamellar Microdomains of Symmetric Diblock Copolymers on Topologically Nano-Patterned Surfaces*

For lamellae forming symmetric diblock copolymers, it is well known that without any guiding patterns, the lamella microdomains give fingerprint-like surface patterns on non-selective substrates as reported previously with a variety of model diblock copolymers. The fact that this fingerprint-like pattern contains many regions of high curvature of bent lamellae suggests the energetic cost of lamellae bending maybe relatively small. Nealey et al.[14] reported that the lamellar microdomains of PS-b-PMMA follows faithfully the lithographically predefined surface patterns of chemical contrast. They showed that bent block copolymer lamellae could be obtained when homopolymers were added to the copolymer. More recently, Wilmes et al. examined the extent to which patterns with different curvatures can be created within the same block copolymer thin films. They showed that the lamellae conform to patterns with radii of curvature equal to the equilibrium domain spacing. In this section, using self-consistent field calculation we report our investigation on the collective bending property of lamellae result-

ing from directed assembly of symmetric diblock copolymer using topographic guiding patterns. The topographic guiding patterns are designed as elbows with varying corner angles as shown in Figure 4.1.

4.2.1 Self-Consistent Field Calculations

The SCF equations are given by Eq. (2.5)~(2.9), with the replacement of $\phi_0(x)$ by $\phi_0(\mathbf{r})$ in Eq. (2.9) due to the two dimensional confinement considered here. The chain propagators $q(\mathbf{r}, s)$ and $q^*(\mathbf{r}, t)$ satisfying Eq. (6.8) and Eq. (6.9) respectively. Since our computational study is carried out in collaboration with experimental investigations, all the parameters required by the calculation are estimated based on the information provided by experiments where symmetric diblock copolymer of poly(methyl methacrylate), poly(styrene-b-methyl methacrylate) (PS-b-PMMA) is used. The formula $\chi = 0.028 + 3.9/T$ [15] is used to estimate the Flory-Huggins parameter at the annealing temperature T in units of Kelvin. For the symmetric PS-b-PMMA diblock copolymers used in experiments, assuming the same statistical segment length of a 0.66 nm and bulk density for both PS and PMMA segments, our SCF calculations give the bulk lamellar period of $L_0 \approx 31$nm, with $N = 733$ being the total number of segments on each diblock copolymer chain, which is close to the experimental value of 28 nm for 36 kg/mol PS-b-PMMA.

Based on the experimental findings, we perform 2D self-consistent field (SCF) calculations in real space, without a priori knowledge about the possible morphologies. Our 2D SCF calculations are performed in a rectangular unit cell shown in Figure 4.1, where the periodic boundary conditions are applied in the x (horizontal) direction and the reflective boundary conditions are applied

in the y (vertical) direction. Two parallel walls are placed at a separation distance $D_1 = 100$nm to represent the topographic elbow-patterns. The length of each wall $L = 312$nm together with the angle θ determines the cell size L_y. The cell size L_x is chosen such that under the periodical boundary conditions the distance D_2 between the two walls as marked in the figure is 200nm. To exclude copolymers from the regions occupied by the walls while maintain good numerical performance of SCF calculations, we impose the following overall copolymer segmental density profile $\phi_0(\mathbf{r}) = \phi_A(\mathbf{r}) + \phi_B(\mathbf{r})$:[16]

$$\begin{aligned}\phi_A(\mathbf{r}) + \phi_B(\mathbf{r}) =& 1 - \frac{1}{2}\tanh\frac{4(x - x_1(y) + \eta)}{\tau}\tanh\frac{4(-x + x_1(y) + \eta)}{\tau} \\ & - \frac{1}{2}\tanh\frac{4(x - x_2(y) + \eta)}{\tau}\tanh\frac{4(-x + x_2(y) + \eta)}{\tau}\end{aligned} \tag{4.1}$$

where $\phi_A(\mathbf{r})$ and $\phi_B(\mathbf{r})$ are the segmental densities (volume fractions) of A and B segments, respectively, at position $\mathbf{r} = (x, y)$; $x_1(y)$ and $x_2(y)$ denote the x-coordinates of the two wall centers, respectively, with the relation $x_2(y) - x_1(y) = D_1/\cos(\theta)/2)$; and we set $\eta = 0.5\sqrt{N/6}a \approx 3.65$nm and $\tau = 0.4\sqrt{N/6}a \approx 2.92$nm. In addition to $\phi_A(\mathbf{r})$ and $\phi_B(\mathbf{r})$ at equilibrium (i.e., the morphology), the SCF calculations further provide us with the corresponding free-energy density $f_c(\mathbf{r})$ and its components, which can help us understand the formation mechanism of the obtained morphology. In particular, the mean-field free energy (of mixing) per chain F_c is given by:

$$\begin{aligned}F_c =& \frac{1}{\bar{\phi}_C V}\int d\mathbf{r}\,[f_{AB}(\mathbf{r}) + f_{el}(\mathbf{r})] \\ =& \frac{1}{\bar{\phi}_C V}\int d\mathbf{r}\,[f_{AB}(\mathbf{r}) - \omega_A(\mathbf{r})\phi_A(\mathbf{r}) - \omega_B(\mathbf{r})\phi_B(\mathbf{r})] - \ln Q_C\end{aligned} \tag{4.2}$$

where V is the system volume and $\overline{\phi}_C = \int d\mathbf{r} \left[\phi_A(\mathbf{r}) + \phi_B(\mathbf{r})\right]/V$ is the average copolymer segmental density. As shown in Eq. (4.2), $f_c(\mathbf{r})$ has two contributions: $f_{AB}(\mathbf{r}) = \chi N \phi_A(\mathbf{r})\phi_B(\mathbf{r})$ corresponds to the local repulsion between A and B segments, and the chain elastic free-energy density $f_{el}(\mathbf{r})$ is due to the chain conformational entropy.

4.2.2 Results and Discussions

For the purpose of comparison with the results from our SCF calculations, Figure 4.2 shows top-down SEM images of lamellar microdomains in PS-b-PMMA thin films on paired neutral elbow-patterns with varying angles θ from 30° to 170° in 20° increments.

Figure 4.3(a) and (c) show the segmental density (volume fraction) profiles of lamellae confined in paired elbow-patterns at different elbow-pattern angles obtained from SCF calculations. At $\theta = 70°$(Figure 4.3(a)) the lamellar domains form arc structures in the inner regions close to the elbow corners, and bend structures farther away from the corners. Such structures were referred to as "chevron" kinks by Gido and Thomas.[17] The bend structures terminate in the linear regions of the elbow-patterns, where aligned lamellae connecting the side walls form. Similar results are also found at $\theta = 90°$ and $\theta = 110°$ (data not shown). At $\theta = 130°$ (Figure 4.3(c)) and $\theta = 150°$ (data not shown), the SCF calculations show that the lamellae break and form asymmetric "omega" kinks[17] in the inner regions close to the elbow corners. Finally at $\theta = 170°$ (data not shown), only aligned lamellae connecting the side walls are obtained. These are in good agreement with the experimental observations at $\theta \geq 50°$ discussed above. Note that the experimental results contain more

defects, partly due to the larger gap width than that used in our calculations; on the other hand, we have used different initial guesses in our SCF calculations and at each only the morphology with the lowest free energy is presented.

The tilting angle φ of lamellar domains with respect to the side walls are also measured in our calculations. Since the titling angle depends on the distance from the elbow corner, we measure φ of the bending lamellar interface whose vertex is located at the middle of corner-to-corner distance in accordance with the experiments. The tilting angle $\varphi = 90^{\circ}$ when lamellae are confined between two parallel neutral walls. For lamellae confined between paired elbow-patterns, our SCF results in Figure 4.4 show that φ first decreases with increasing θ and then increases abruptly to about 90° at $\theta = 130^{\circ}$. This result is in good qualitative agreement with experimental data as shown in Figure 4.4.

The observed variation of φ with θ can be understood from the free-energy densities provided by the SCF calculations. Figure 4.3(b) shows the chain elastic free-energy density $f_{el}(\mathbf{r})$, due to chain-stretching (loss of chain conformational entropy) at $\theta = 70^{\circ}$. We see that $f_{el}(\mathbf{r})$ is high in the middle of A-rich and B-rich domains (due to the localization of chain ends) and even higher at the bend vertices. This indicates that the formation of bend structures costs a lot of chain conformational entropy. To reduce the degree of bending of lamellae and thus alleviate such a high entropic penalty, lamellae tilt at an angle φ smaller than 90° with respect to the side walls. Since a neutral side wall prefers lamellae oriented perpendicular to it,[18] a tilting angle $\varphi < 90^{\circ}$ increases the chain elastic free energy close to the wall. In other words, there is a balance between the bending and tilting of lamellae confined in-between the

elbow-pattern. As θ increases from 70° to 110°, reducing the lamellae bending at the cost of increasing lamellae tilting dominates, which explains the decrease of φ.

As θ further increases, decreasing φ is not sufficient for reducing the bending penalty. Lamellae thus break and form "omega" kinks, i.e., defects with highly localized chain elastic free-energy density as shown in Figure 4.3(d). This is more effective to reduce the entropic penalty in other regions and thus lower the overall free energy of the system. φ therefore increases abruptly to almost 90° at $\theta = 130°$.

Due to the large cell size L_x needed, we have not performed SCF calculations for $\theta < 70°$. The bending of lamellae in such cases, however, can be inferred from our results at $\theta = 70°$, where, as lamellae move closer to the elbow corners, the space in-between the elbow-pattern becomes smaller. In such small confined space, forming bend structures with vertices of high elastic free-energy density is not favored; instead, arc structures with less bending (no vertices) form. This situation is similar to that when θ decreases, where lamellae tend to go straight from one side wall to the other as shown in Figure 4.2(b) at $\theta = 30°$. The lamellar bending is therefore reduced at the cost of increasing lamellae tilting. This is clearly shown by our results in Figure 4.4 (the inset figure) at $\theta = 70°$, where φ decreases as lamellae move closer to the elbow corners, in accordance with the decrease of φ as θ decreases from 70° to 30° observed in experiments.

4.3 Complex Nanostructure of Cylinder-Forming Diblock Copolymers on Chemically Nano-Patterned Substrates

In this section we consider cylinder forming DBC on nanopatterned substrates of alternating neutral and preferential stripes. We demonstrate that the directed assembly of a block copolymer on such a chemically patterned surface may produce a well-registered novel complex nanostructure. When a cylinder-forming block copolymer was assembled on a chemical pattern whose period was twice as large as the natural lattice size of the block copolymer, a new structure was produced, where cylinders were oriented alternately perpendicular and parallel to the surface. This intrinsically 3D structure provides linear arrays of nanocylinders whose orientation is registered by the surface pattern underneath. Our work shows that a judiciously designed chemical pattern may be used to fabricate a well-ordered complex nanostructure in block copolymer thin films.

4.3.1 Self-Consistent Field Calculations

We performed 3D real-space self-consistent field (SCF) calculations. The SCF equations are given by Eq. (2.5)−(2.9). The usual incompressibility constraint i.e., $\phi_0(x) = 1$ is enforced in everywhere in the system. Since our computational study is carried out in collaboration with experimental investigations, all the parameters required by the calculations are estimated based on the information provided from experiments. $N = 652$ is the total number of segments in the copolymer chain; the volume fraction of the shorter (A) block $f_A = 0.3$; and the product of chain length N with the FloryCHuggins χ parameter between A and B segments is 18.3. We denote the distance between neighboring cylinders formed in bulk condition by L_0. This corresponds to PS-b-PMMA diblock

copolymers in experiment, with PMMA being the minor block.

Figure 4.1 shows the patterned substrates of alternating neutral and preferential stripes with period L_s. The preferential stripes have width $w = 0.5L_0$ and attract the A block. The upper surface was set to be neutral, and we denote the film thickness by D. Accordingly, the H field in Eq. (2.5) and (2.6) that represents the energetic surface preference for the two blocks are given by

$$H(x,y) = \frac{\Lambda(y)}{2}(1+\cos\frac{x\pi}{0.4}) \tag{4.3}$$

for $x < 0.4$ (in units of $a\sqrt{N/6}$) and 0 otherwise, where a is the statistical segment length (taking the same value of 0.66 nm for both A and B), and we set $\Lambda(y) = 5$ for the preferential stripes and 0 for the neutral stripes. Periodic boundary conditions were applied in the y- and z-directions, and the Neumann boundary conditions were applied in the x-direction.

4.3.2 Results and Discussion

For the purpose of comparison with the results from SCF calculations, Figure 4.5 shows the top-view scanning electron microscopy (SEM) images obtained from experiments of the morphological evolution of the diblock copolymer thin film as the preferential stripe period L_s and film thickness D being adjusted.

In SCF calculations, we first set $L_s = L_0$ and $D = \sqrt{3}L_0/2$. Figure 4.6(a) shows that two layers of staggered, parallel half-cylinders formed in the film, in register with the substrate pattern, corresponding to the film on the patterned substrates shown in Figure 4.5(c). The well-aligned stripes parallel to the surface observed

in Figure 4.5(c) correspond to the upper layer of half-cylinders.

In Figures 4.6(b) and (c), we changed L_s to $2.3L_0$ by increasing the width of the neutral stripes. Two different morphologies were obtained in SCF calculations. One is again that of two layers of staggered, parallel half-cylinders, as shown in Figure 4.6(b); here the lower half-cylinders are located alternately on the preferential and neutral stripes. The other is a mixed morphology of two layers of parallel half-cylinders on the preferential stripes and perpendicular cylinders on the neutral stripes, as shown in Figure 4.6(c). The latter corresponds to the morphology of stripes and dots observed in Figure 4.5(d) and (e). Note that, unlike the morphologies shown in Figure 4.6(a) and (b), here the parallel half-cylinders in the upper layer were located directly above the half-cylinders in the lower layer; this compressed the parallel half-cylinders, as clearly revealed by the SCF calculations. Our calculations also revealed small undulations of the perpendicular cylinders along the x-direction, and some deformations of the parallel half-cylinders by the perpendicular cylinders. Minimizing the system free energy with respect to the calculation cell size along the z-direction showed that the distance between neighboring perpendicular cylinders in a row is slightly smaller than L_0. Finally, our SCF calculations indicate that both morphologies shown in Figure 4.6(b) and (c) have about the same free energy (the difference is less than $0.03kBT$ per chain, where kB is the Boltzmann constant and T the absolute temperature). This could explain the high density of defects observed in experiments.

In Figure 4.6(d), we reduced the film thickness to $D = \sqrt{3}L_0/4$ which corresponds to the experimental system shown in Figure 4.6(f). The upper layer of the parallel half-cylinders now disappeared and the morphology changed into

alternating parallel half-cylinders and perpendicular cylinders. The presence of the underlying parallel half-cylinders explains the experimental observations that the film thickness was spontaneously quantized and that the interval region between adjacent rows of dots appeared dark. For this thin thickness, the morphology of one layer of parallel half-cylinders turned out to have a higher free energy than the mixed morphology. From Figure 4.6(d), we see that the parallel half-cylinders are stretched in the y-direction significantly. The free-energy penalty due to such stretching could be relieved by forming perpendicular cylinders on neutral stripes. Overall, our SCF calculations are in good agreement with experimental observations and further provide detailed 3D structures inside thin films.

4.4 Conclusion

We have demonstrated that bending and arc geometries of lamellar microdomains in block copolymer films can be formed on angled corners of topographic guiding patterns with non-selective wetting property, thereby providing an extension of the capabilities of graphoepitaxial technique. The ability to generate non-linear geometry of lamellar microdomains using neutral topographic guiding patterns is scientifically interesting because it demonstrates the degree to which angled topographic patterns directs the assembly of lamellar bends in a thin block copolymer film.

We also show that directed assembly on incommensurate surface patterns may induce a new complex nanostructure in block copolymer thin films. The cylinders of an asymmetric block copolymer were alternately oriented parallel to

the surface on preferential stripes and perpendicular to the surface on neutral stripes, constituting a novel complex morphology. The nanoscale morphology provides a well-ordered linear nanocylinder array, whose orientation is in register with the underlying stripe pattern.

List of Figures

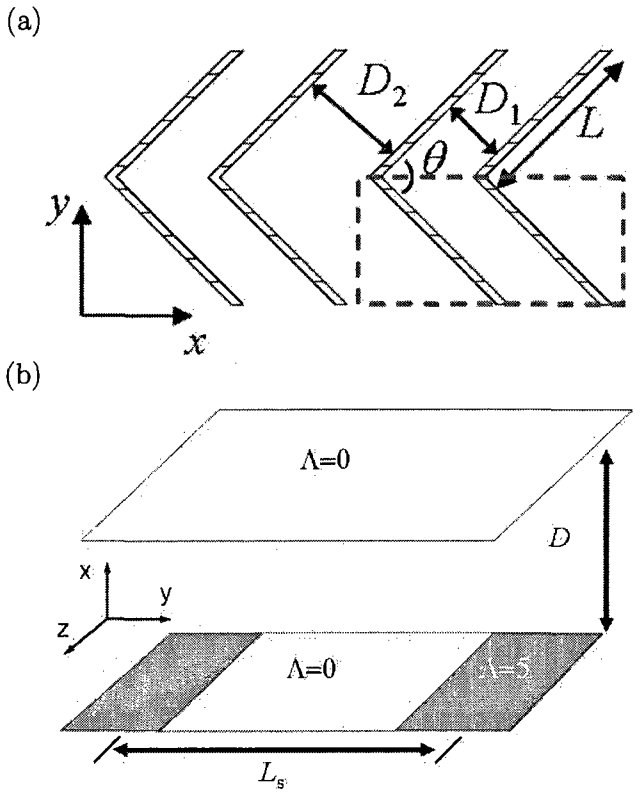

Fig. 4.1: (a) The unit cell (area enclosed by the dashed lines) used in our SCF calculations in Section 4.2. The sidewalls of the topographic elbow-patterns are represented by the two parallel shaded walls in our unit cell, and the unit cell is duplicated in both x- and y-directions according to the boundary conditions applied. (b) The unit cell used in our SCF calculations in Section 4.3. The upper surface was set to be neutral; the lower substrate has alternating neutral and preferential stripes with period L_s. The width of preferential stripes $w = 0.5L_0$. The film thickness is denoted by D.

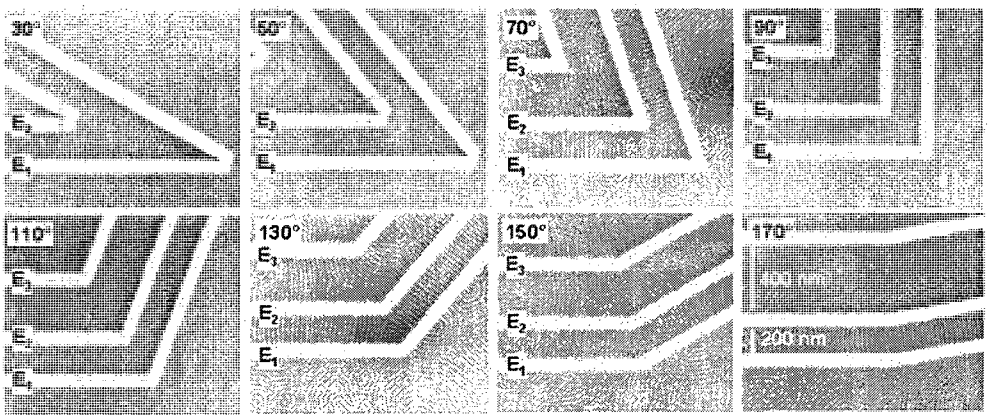

Fig. 4.2: top-down SEM images of lamellar microdomains in PS-b-PMMA thin films on paired neutral elbow-patterns with varying angles θ from 30° to 170° in 20° increments.

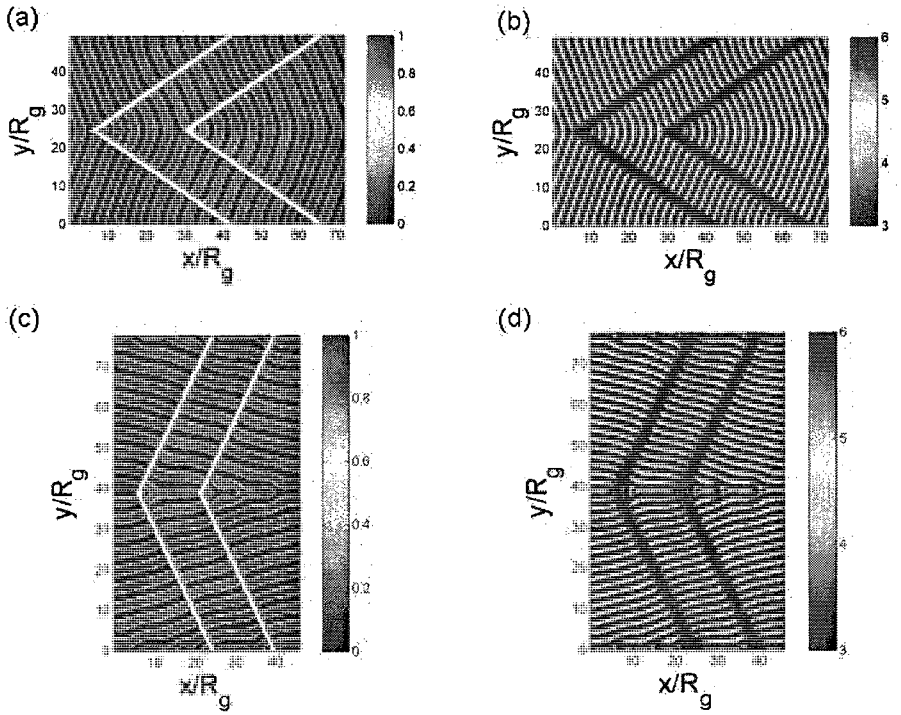

Fig. 4.3: Segmental density profiles of symmetric diblock copolymers confined between paired elbow-patterns at (a)$\theta = 70^o$ and (c)$\theta = 130^o$ obtained from SCF calculations. The $\widetilde{\phi}_{\mathrm{A}}(\mathbf{r})$ shown on the plots is defined as $\widetilde{\phi}_{\mathrm{A}}(\mathbf{r}) \equiv \frac{\phi_A(\mathbf{r})}{\phi_A(\mathbf{r})+\phi_B(\mathbf{r})}$. The bright and dark domains correspond to the A-rich and B-rich region respectively; the side walls are represented by the blank region. The unit cell is duplicated in the y direction according to the reflecting boundary condition. Distribution of elastic free energy f_{el} at (b)$\theta = 70^o$ and (d)$\theta = 130^o$.

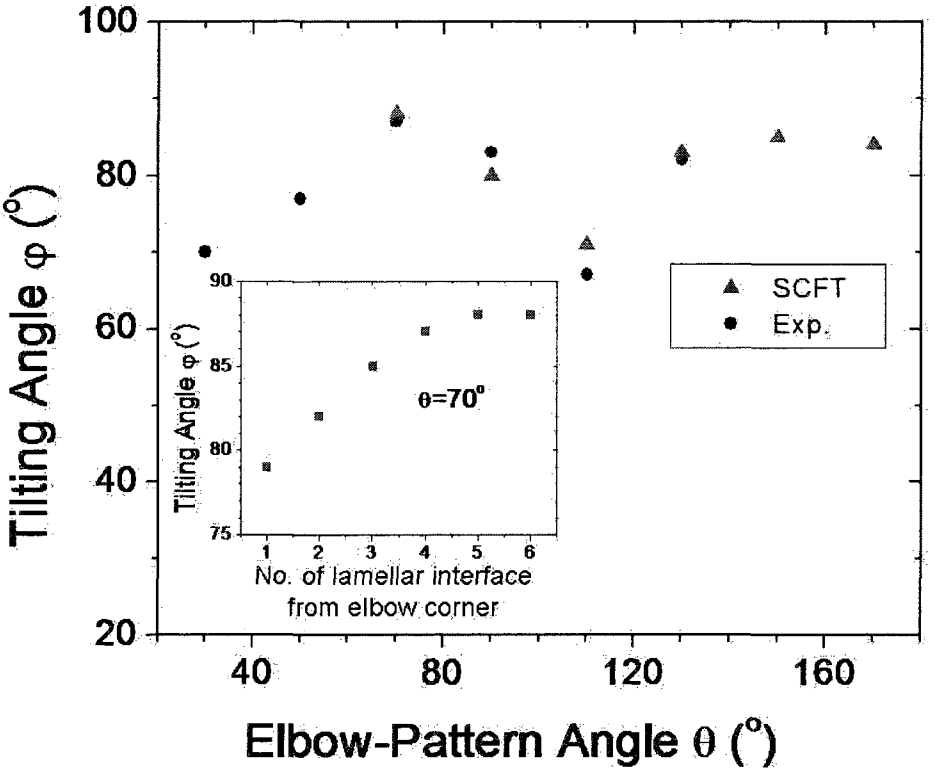

Fig. 4.4: Variation of lamellar tilting angle φ with the elbow-pattern angle θ. (Inset) Lamellar tilting angle φ measured at different lamellar interfaces with $\theta = 70^o$. The interfaces are sequentially labeled according to their distance from the elbow-pattern corner.

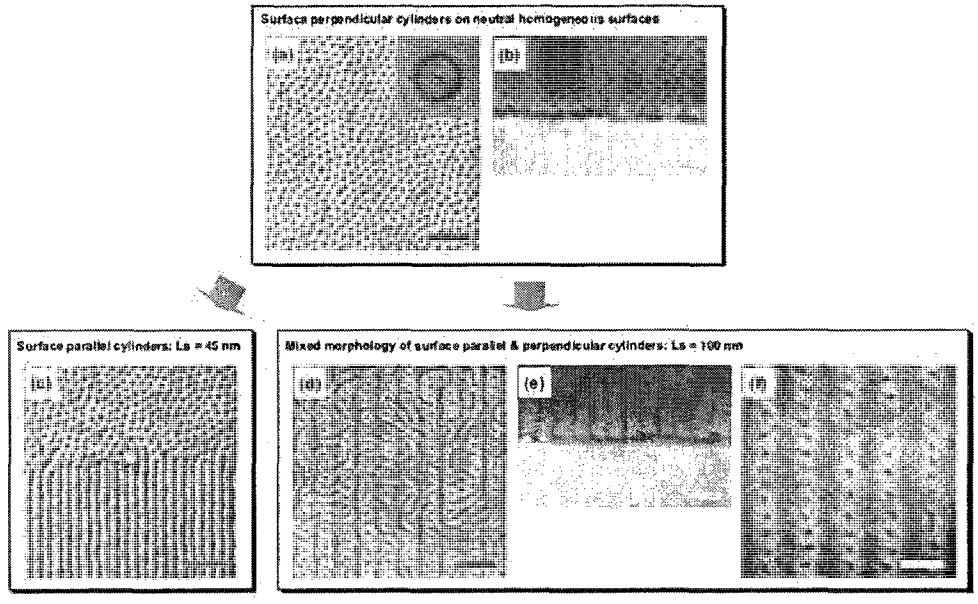

Fig. 4.5: Nanostructure evolution (SEM images) in block copolymer thin films. (a) Top and (b) cross-sectional views of cylinders perpendicular to the surface on a chemically neutral homogeneous surface. (c) Top view of block copolymer morphology on a commensurate pattern ($L_s = L_0$, film thickness $D = 0.866L_0$, $L_0 = 45$nm). Cylinders were registered by the commensurate chemical pattern to line up parallel to the surface (bottom of the image), whereas they were oriented perpendicular to the surface, revealing hexatic ordering, on an unpatterned neutral surface (upper part of the image). (d) Top and (e) cross-sectional views of the novel block copolymer nanostructure on an incommensurate surface pattern ($L_s = 2.3L_0$ and $D = 0.866L_0$). Cylinders were alternately oriented parallel and perpendicular to the surface to constitute a novel complex morphology. The density of defects was high in this film thickness. (f) Defect-free complex morphology assembled on an incommensurate surface pattern ($L_s = 2.3L_0$ and $D = 0.866L_0$). Linear arrays (rows) of nanocylinders perpendicular to the surface are shown. Red and yellow scale bars correspond to 200 and 100 nm, respectively.

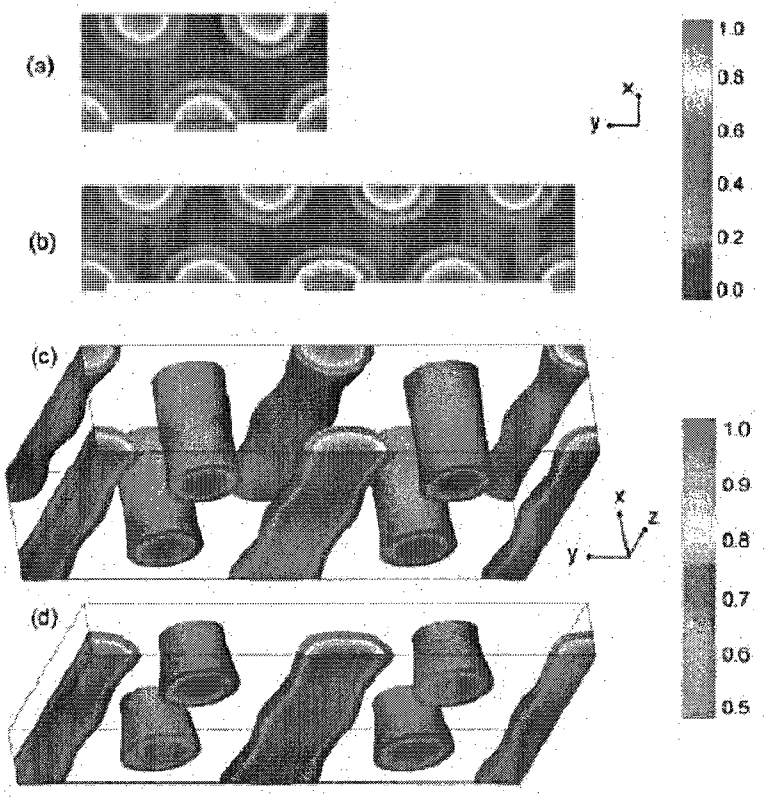

Fig. 4.6: Thin-film morphology obtained from self-consistent field calculations. The stripe-patterned substrate with a period L_s is placed at $x = 0$ and a top neutral surface is at $x = D$, with periodic boundary conditions applied in both the y- and z-directions. The preferential stripes (represented in teal blue) on the substrate are along the z-direction and have width $w = 0.5L_0$; these preferential stripes attract the A (PMMA) block, while the neutral stripes are not shown. The color bars correspond to the volume fraction of the A (PMMA) block. (a) Two layers of parallel half-cylinders ($L_s = L_0$ and $D = 0.866L_0$). (b) Two layers of parallel half-cylinders ($L_s = 2.3L_0$ and $D = 0.866L_0$). (c) Mixed morphology of two layers of parallel half-cylinders on preferential stripes and perpendicular cylinders on neutral stripes ($L_s = 2.3L_0$ and $D = 0.866L_0$). (d) Mixed morphology of alternating parallel half-cylinders on preferential stripes and perpendicular cylinders on neutral stripes ($L_s = 2.3L_0$ and $D = 0.433L_0$).

BIBLIOGRAPHY

[1] H. H. Solak, J. Phys. D: Appl. Phys., **39**, R171 (2006).

[2] D. S. Ginger, H. Zhang and C. A. Mirkin, Angew. Chem. Int. Ed., **43**, 30 (2004).

[3] S. Y. Chou, P. R. Krauses and P. J. Renstrom, Science, **272**, 85 (1996).

[4] B. A. Parvia, D. Ryan and G. M. Whitesides, IEEE Trans. Adv. Packag., **26**, 233 (2003).

[5] R. A. Segalman, H. Yokoyama and E. J. Kramer, Adv. Mater., **13**, 1152 (2001).

[6] S. O. Kim, H. H. Solak, M. P. Stoykovich, N. J. Ferrier, J. J. de Pablo and P. F. Nealey, Nature, **424**, 411 (2003).

[7] M. P. Stoykovich, M. Muller, S. O. Kim, E. W. Edwards, J. J. de Pablo and P. F. Nealey, Science, **308**, 1442 (2005).

[8] J. Y. Cheng, A. M. Mayes and C. A. Ross, Nat. Mater., **3**, 823 (2004).

[9] M. Park, C. Harrison, P. M. Chaikin, R. A. Register and D. H. Adamson, Science, **276**, 1401 (1997).

[10] T. Thurn-Albrecht, J. Schotter, G. A. Kastle, N. Emley, T. Shibauchi, L. Krusin-Elbaum, K. Guarini, C. T. Black, M. T. Tuominen and T. P. Russell, Science, **290**, 2126 (2000).

[11] M. J. Fasolka and A. M. Mayes, Annu. Rev. Mater. Res., **31**, 323 (2001).

[12] S. O. Kim, B. H. Kim, K. Kim, C. M. Koo, M. P. Stoykovich, P. F. Nealey and H. H. Solak, Macromolecules **39**, 5466 (2006).

[13] J. Israelachvili, Intermolecular and Surface Forces, 2nd ed., Academic, London 1992.

[14] R. Ruiz, H. M. Kang, F. A. Detcheverry, E. Dobisz, D. S. Kercher, T. R. Albrecht, J. J. de Pablo and P. F. Nealey, **321**, 936 (2008).

[15] T. P. Russell, R. P. Hjelm and P. A. Seeger, Macromolecules, **23**, 890 (1990).

[16] V. Khanna, E. W. Cochran, A. Hexemer, G. E. Stein, G. H. Fredrickson, E. J. Kramer, X. Li, J. Wang and S. F. Hahn, Macromolecules, **39**, 9346 (2006).

[17] S. P. Gido, and E. L. Thomas, Macromolecules, **27**, 6137 (1994).

[18] D. Meng and Q. Wang, J. Chem. Phys., **126**, 234902 (2007).

Part II

SMART SURFACES OF POLYMER BRUSHES

5. THERMAL-RESPONSE OF POLY-NIPAM BRUSHES IN WATER

5.1 Introduction

Unlike most polymers, water soluble PNIPAM (poly(N-isopropylcarylamide)) exhibits lower critical solution temperature (LCST) in water solution.[1–4] While the polymer is completely miscible in water at low temperature, as temperature is raised above LCST, the solution phase separates into polymer-rich and polymer-poor phases. Such behavior is due to the hydrogen bonding of PNIPAM segments with water molecules and it leads to many important applications, such as making temperature responsive thermal gels, colloidal dispersion, controlled drug delivery, solute separation.[5–10] Because of these promising properties, the research involving PNIAPM have drawn great interests recently, from both experiments[11–16] and theoretical investigations.[17–23] In particular, there is a special significance in the work by Afroze et. al,.[16] In their work, the binodal curves of PNIPAM bulk solution with large molecular weight are experimentally measured, and the curves are fitted to the computational results from Flory-Huggins theory with a concentration dependent χ parameter expressed as a polynomial function of polymer concentration. Through fitting, the temperature dependent polynomial parameters are obtained, and by doing this it provides a convenient way to model the LCST behavior of PNIPAM

solutions phenomenologically without having to include the complex nature of hydrogen bonding mechanisms.

Because of its thermal responsive property, grafting PNIPAM onto surfaces is a promising strategy for creating responsive surfaces. Such thermal responsive surfaces have a variety of applications in tissue culture substrates, controlling absorption of proteins, blood cells and bacteria. To better design such temperature responsive surface, it is important to understand how the conformations of grafted PNIPAM chains change with temperature. Significant effort has been put into such studies.[25–33] Kidoaki et al.[25] used AFM to study the dense, high molecular weight PNIPAM brushes and reported changes in brush height with temperature. Balamurugan et al. [26] used surface plasmon resonance (SPR) to investigate conformational changes on a gold surface and also reported significant change of brush height with temperature. However a systematic study of such temperature responsive conformational changes as a function of molecular weight and surface grafting density was largely absent until Yim et al.[27–31] reported a series of experiments using neutron reflection (NR) to capture the temperature response of PNIPAM brushes. In their study they found that, only at proper surface grafting density and molecular weight, the brush height is observed to change with temperature. Using NR they also found that the segmental density profiles of the brush has a two-layer shape with the inner layer having higher polymer concentrations than the outer layer. Such phase separation happens within the tethered layer and therefore is also known as vertical phase separation. This is the first time that direct experimental evidence of vertical phase separation of PNIPAM brushes had been reported, even though such behavior had been predicted by the theoretical studies of

Baulin and Halperin using the Pincus model.[22]

In Baulins and Halperin's work,[22] a number of forms of the concentration dependent χ parameters had been used to investigate their effects on the brush segmental density profiles. In particular, using values of χ from Afroze's[16] work they showed that only when the surface grafting density is high enough will the vertical phase separation occur at one temperature. However, the effects of chain length on the vertical phase separation were left unstudied. More importantly, because their work focused more on the effects of different forms of χ parameter, how the transitions of brush segmental profiles occur with temperature change (the thermal response of PNIPAM brushes) was not included. A later study by Baulin, et. al,.[23]used the more accurate analytical mean field model the strong stretching theory (SST) to study PNIAPM brushes. In their work, brush density profiles are very similar to those obtained using the Pincus model, and the effects of grafting density on the vertical phase separation are also shown. Because the chain-end distribution in the SST can be analytically solved rather than assumed, their work also includes the study of the compression force profile of PNIAPM brushes. The full numerical mean field study on PNIPAM brushes was first performed by Mendez et al[19] using the density functional theory with the χ parameter adopted from Afroze's work. The effects of grafting density and polymer chain length on the thermal response of PNIPAM brushes were systematically studied. However, in their work, the polymer concentration used in calculating the χ is the averaged rather than the local polymer concentration in the brush solution. This causes the discrepancy between the homogeneous χ parameter and the inhomogeneous segmental density in the brushes.

In this work, from a theoretical point of view we want to study systematically the effects of the grafting density and polymer chain length on the thermal response of PNIPAM brushes using the numerical self-consistent field theory (NSCFT). The Flory-Huggins χ parameter in the our model depends on the local segmental density in the brushes and having the form given by Afroze's work.

5.2 Theoretical Formalism and Numerical Methods

5.2.1 Numerical Self-Consistent Field Calculations

We use numerical (real-space) self-consistent field (SCF) calculations in this work. Since the polymer SCF theory has been well developed, we only summarize our SCF equations and numerical methods here; readers are referred to, e.g., Ref. [34] for detailed derivation and explanation of this theory.

We consider the brush formed by homopolymers A (PNIPAM) of chain length N end-grafted onto a flat and impenetrable substrate placed at $x = 0$. The brush is immersed in a small-molecule solvent S (water). We neglect the energetic preference of the substrate, and assume that the polymer segments have the same density ρ_0 as the solvent molecules and the statistical segment length a. Our SCF equations are

$$\omega_{\mathrm{A}}(\mathbf{r}) = \chi(\phi_{\mathrm{A}}(\mathbf{r}))N\phi_{\mathrm{S}}(\mathbf{r}) + \frac{\mathrm{d}\chi(\phi_{\mathrm{A}}(\mathbf{r}))}{\mathrm{d}\phi_{\mathrm{A}}(\mathbf{r})}N\phi_{\mathrm{A}}(\mathbf{r})\phi_{\mathrm{S}}(\mathbf{r}) + \eta(\mathbf{r}) \tag{5.1}$$

$$\omega_{\mathrm{S}}(\mathbf{r}) = \chi(\phi_{\mathrm{A}}(\mathbf{r}))N\phi_{\mathrm{A}}(\mathbf{r}) + \eta(\mathbf{r}) \tag{5.2}$$

$$\phi_{\mathrm{A}}(\mathbf{r}) = \frac{\bar{\phi}_{\mathrm{A}}}{Q_{\mathrm{A}}}\int_0^1 \mathrm{d}s q(\mathbf{r}, s)q^*(\mathbf{r}, 1-s) \tag{5.3}$$

$$\phi_{\mathrm{S}}(\mathbf{r}) = \frac{\bar{\phi}_{\mathrm{S}}}{Q_{\mathrm{S}}} \exp\left[-\frac{\omega_{\mathrm{S}}(\mathbf{r})}{N}\right] \tag{5.4}$$

$$\phi_{\mathrm{A}}(\mathbf{r}) + \phi_{\mathrm{S}}(\mathbf{r}) = 1 \tag{5.5}$$

Here $\phi_{\mathrm{A}}(\mathbf{r})$ and $\phi_{\mathrm{S}}(\mathbf{r})$ are the normalized (by ρ_0) density (i.e., volume fraction) fields of A segments and S molecules, respectively, at position $\mathbf{r}$; $\omega_{\mathrm{A}}(\mathbf{r})$ and $\omega_{\mathrm{S}}(\mathbf{r})$ are the (purely imaginary) conjugate fields interacting the corresponding species. The (purely imaginary) conjugate field $\eta(\mathbf{r})$ enforces the incompressibility constraint, Eq. (7.10).

$\chi(\phi_{\mathrm{A}}(\mathbf{r}))$ is the concentration-dependent Flory-Huggins interaction parameter between PNIPAM segments and water, obtained from the experimental fitting by Afroze *et al.*,[16]

$$\chi(\phi_{\mathrm{A}}(\mathbf{r})) = (a_0 + b_0 T) + (a_1 + b_1 T)\phi_{\mathrm{A}}(\mathbf{r}) + (a_2 + b_2 T)\phi_{\mathrm{A}}^2(\mathbf{r}) \tag{5.6}$$

where T is the temperature, and a_i and b_i $(i = 0, 1, 2)$ are constants obtained from the fitting. Fig. 5.1 shows how the parameter χ calculated from Eq. (5.6) changes with respect to polymer concentration at three different temperatures. Note that we take the χ parameter to be dependent of the local polymer segmental density $\phi_{\mathrm{A}}(\mathbf{r})$ (i.e., position-dependent); this is different from that used by Mendez *et al.*, who took χ as a function of the volume-averaged polymer segmental density $\bar{\phi}_{\mathrm{A}}$ (i.e., position-independent) in their SCF calculations.[19]

The propagator $q(\mathbf{r}, s)$ corresponds to the probability of finding a copolymer chain of length sN that starts from the grafted end (where $s = 0$) and ends at position $\mathbf{r}$, and is commonly calculated from the following modified diffusion

equation (MDE)

$$\frac{\partial q}{\partial s} = \nabla^2 q - \omega_{\rm A}(\mathbf{r})q \tag{5.7}$$

with the corresponding initial and boundary conditions discussed later. Similarly, the propagator $q^*(\mathbf{r}, t)$ with $t \equiv 1 - s$ corresponds to the probability of finding a copolymer chain of length tN that starts from the free end (where $s = 1$) anywhere in the system and ends at $\mathbf{r}$, and is calculated from the following MDE

$$\frac{\partial q^*}{\partial t} = \nabla^2 q^* - \omega_{\rm A}(\mathbf{r})q^* \tag{5.8}$$

Alternatively, $q(\mathbf{r}, s)$ can be calculated from the Chapman-Kolmogorov equation (CKE)[37]

$$q(\mathbf{r}, s + {\rm d}s) = \exp[-\omega_{\rm A}(\mathbf{r}){\rm d}s] \int {\rm d}\mathbf{r}' \Phi(\mathbf{r} - \mathbf{r}')q(\mathbf{r}', s) \tag{5.9}$$

where $\Phi(\mathbf{r} - \mathbf{r}') = (4\pi {\rm d}s)^{-d/2} \exp(-|\mathbf{r} - \mathbf{r}'|^2/4{\rm d}s)$ corresponds to the probability for a Gaussian chain to propagate from $\mathbf{r}'$ to $\mathbf{r}$ over a small chain length of $N{\rm d}s$, and d is the dimensionality of the system. A similar CKE holds for q^*.

In Eqs. (7.4) and (7.6), $Q_{\rm A} = \int {\rm d}\mathbf{r} q(\mathbf{r}, 1)/V$, $Q_{\rm S} = \int {\rm d}\mathbf{r} \exp[-\omega_{\rm S}(\mathbf{r})/N]/V$, $\bar{\phi}_{\rm A} = \int {\rm d}\mathbf{r} \phi_{\rm A}(\mathbf{r})/V$, and $\bar{\phi}_{\rm S} = 1 - \bar{\phi}_{\rm A}$, where V denotes the system volume. Note that we have normalized all the distance by $R_g \equiv a\sqrt{N/6}$ in the above equations. Once the SCF equations are solved, the mean-field free energy (of mixing) per chain can be calculated as

$$\begin{aligned} f_c = \frac{1}{V} \int {\rm d}\mathbf{r} \Big[\chi(\phi_{\rm A}(\mathbf{r}))N\phi_{\rm A}(\mathbf{r})\phi_{\rm S}(\mathbf{r}) - \omega_{\rm A}(\mathbf{r})\phi_{\rm A}(\mathbf{r}) - \omega_{\rm S}(\mathbf{r})\phi_{\rm S}(\mathbf{r}) \Big] \\ -\bar{\phi}_{\rm A} \ln \frac{Q_{\rm A}}{\bar{\phi}_{\rm A}} - N\bar{\phi}_{\rm S} \ln \frac{Q_{\rm S}}{\bar{\phi}_{\rm S}} \end{aligned} \tag{5.10}$$

Assuming lateral homogeneity, we perform 1D calculations in the spatial domain of $0 \leq x \leq l$, where l is chosen to be large enough such that the total polymer segmental density $\phi_A(x) \leq 10^{-5}$ at $x = l$ in all cases. The volume-averaged polymer segmental density $\bar{\phi}_A$ is then related to the chain-grafting density σ_0 (i.e., number of chains per substrate area of a^2) by $\bar{\phi}_A = \sqrt{6N}\sigma_0/l$, where we have used $\rho_0 = a^{-3}$. When solving the propagators, we apply the Neumman boundary conditions of $\partial q(x,s)/\partial x = \partial q^*(x,s)/\partial x = 0$ at $x = 0$ and l for all s, together with the initial condition of $q(x, s = 0) = \delta(x)$ for Eqs. (5.7) and (7.11) (i.e., we assume that all the grafted ends are fixed at $x = 0$); the initial condition of $q^*(x, t = 0) = 1$ at $0 \leq x \leq l$ is also used.

5.2.2 *Numerical Methods and Calculated Quantities*

In our calculations, the chain contour is uniformly discretized into 200 steps, and the spatial domain is uniformly discretized into 256 subintervals. In most cases, we calculate the propagators from CKE using the Romberg integration[35] in order to avoid the numerical problem encountered in brush calculations when solving MDE.[36,38] But in a few cases where the solvent quality is very poor and the polymer chains collapse to form a densely packed layer near the substrate, finer spatial discretization (into 512 subintervals) is needed to converge the SCF calculations; in these cases, we solve MDE using the split-step pseudo-spectral method[39] with the fast cosine transforms due to its faster speed. Detailed numerical comparisons between solving MDE and CKE will be reported in another paper.[38]

The SCF equations are solved in real space by the Broyden method combined with a globally convergent strategy,[40] and the convergence

criterion of $|\phi_A(x) + \phi_S(x) - 1| \leq 10^{-8}$ is satisfied at all collocation points. Here, for given $\omega_A(x)$, Eq. (7.4) is used to calculate $\phi_A(x)$ after q and q^* are solved; $\omega_S(x)$ is then calculated from $\omega_S(x) = \omega_A(x) + N[\chi(x)(\phi_A(x) - \phi_S(x)) - \partial\chi(x)/\partial\phi_A(x)\phi_A(x)\phi_S(x)]$; and $\phi_S(x)$ is then calculated from Eq. (7.6). Finally, since the conjugate fields can be shifted by an arbitrary constant without changing the density fields and the system free energy, we set $Q_A = 10^{-3}$ to obtain a unique solution.

Once the SCF equations are solved, we calculate the brush height as

$$h \equiv \frac{2\int_0^l \mathrm{d}x\phi_A(x)x}{\int_0^l \mathrm{d}x\phi_A(x)} \tag{5.11}$$

Finally, we also check the stability of our 1D brush structures against laterally inhomogeneous (3D) ones by numerically evaluating $\partial^2 f_c/\partial\sigma^2$; a negative value indicates that the 1D structure is unstable.

5.2.3 The Pincus Model

We also compare our numerical SCF calculations with the Pincus model used by Baulin and Halperin.[22] The Pincus model is basically a strong-stretching theory, i.e., only chain conformations that minimize the chain elastic free energy (the classical path) is considered, with the additional assumption that the chain-end distribution is proportional to $\phi_A(x)/N$. The readers are referred to Refs. [22] and [41] for details of the Pincus model and how it is applied to PNIPAM brushes. Here we only summarize its equations. As in Ref. [22], $\phi_A(x)$ in the Pincus model

is calculated from

$$x = \sqrt{\frac{8}{3}}\frac{N}{\pi}\sqrt{\mu_\infty(\phi_0) - \mu_\infty(\phi_A(x))} \tag{5.12}$$

under the constraint

$$N\sigma_0 = \int_0^H \phi_A(x)\mathrm{d}x \tag{5.13}$$

where $\phi_0 \equiv \phi_A(x = 0)$, H denotes the maximum brush height (in unit a) above which $\phi_A(x \geq H) = 0$, $\mu_\infty(\phi_A(x)) \equiv \mathrm{d}f_\infty(x)/\mathrm{d}\phi_A(x)$ with

$$f_\infty(x) = (1 - \phi_A(x))\ln(1 - \phi_A(x)) + \chi(\phi_A(x))\phi_A(x)(1 - \phi_A(x)) \tag{5.14}$$

5.3 Results and Discussion

5.3.1 Bulk Phase Behavior and Vertical Phase Separation in Brush

It is well known that PNIPAM in water exhibits a lower critical solution temperature (LCST). Fig. 5.2 shows the bulk phase diagram of PNIPAM solution with $N \to \infty$ calculated from the Flory-Huggins theory, with the concentration-dependent χ parameter given by Eq. (5.6). As the solution temperature T is below the LCST $T_c \approx 26.4°C$, PNIPAM is completely soluble in water. At $T > T_c$, however, a homogeneous solution may phase separate into two coexisting phases with different polymer concentrations ϕ_+ and ϕ_- as shown in the figure. As T further increases above $T_0 \approx 30.5°C$, the polymer-poor phase becomes pure solvent, *i.e.*, $\phi_- = 0$.

It has also been reported[27–31] that at certain temperatures PNIPAM brushes can form two-layer structures with the inner layer having a higher polymer segmental density than the outer layer, known as the vertical phase separation.[41]

Fig. 5.3 shows the segmental density profiles of a PNIPAM brush at different temperatures, obtained from our numerical SCF calculations. We see that the brush extends at $T = 20°C$, which is below T_c. At $T = 28°C > T_c$, the brush segmental density profile exhibits sharp variation, forming a two-layer structure. The outer layer becomes thinner with increasing T, and at $T = 35°C > T_0$ the brush collapses and forms a step-function-like, single-layer structure as in a poor solvent. This trend is in good agreement with the neutron reflectivity studies of Kent and co-workers.[30]

Such thermal response of PNIPAM brushes can be understood based on the bulk phase diagram shown in Fig. 5.2. For the given example, at $T < T_c$, PNIPAM and water are completely miscible; the brush therefore exhibits an extended segmental density profile as in a good solvent. At $T > T_c$, a bulk homogeneous solution with a PNIPAM concentration between ϕ_+ and ϕ_- becomes unstable against phase separation. Correspondingly, the brush segmental density profile exhibits sharp variation at certain position, representing the interface between the inner layer (a polymerr-rich phase) and the outer layer (a polymer-poor phase). As T further increases, ϕ_- in the bulk phase diagram approaches zero; the outer layer in the brush therefore shrinks and eventually disappears at $T > T_0$.

The connection between the vertical phase separation of PNIPAM brushes in water and their bulk phase behavior was clearly revealed by Baulin and Halperin[22] using the Pincus model.[41] Within this model, they showed that, at the interface (the width of which is neglected) between the two layers, the brush equilibrium condition is equivalent to the bulk equilibrium condition with

$N \to \infty$. In other words, the brush density profile exhibits a discontinuity at the interface, where the polymer segmental densities equal to ϕ_+ and ϕ_- shown in Fig. 5.2;[22] this is illustrated in Fig. 5.4.

5.3.2 Pincus Model vs. Numerical SCF Calculations

Fig. 5.4 also compares the brush segmental density profiles obtained from our numerical SCF calculations with those predicted by the Pincus model using the same parameters. Three differences can be seen: First, there is a spike very close to the grafting substrate in the numerical SCF profile, while in the Pincus model $\phi_A(x)$ smoothly approaches ϕ_0 as $x \to 0$; this is due to the δ-function initial condition used for solving the propagator q in our calculations. Second, the numerical SCF profile exhibits an exponentially decaying tail, while the Pincus model gives $\phi_A(x \geq H) = 0$; this is because all possible chain conformations are included in the numerical SCF calculations, while only that minimizing the chain elastic free energy (i.e., the classical path) is included in the Pincus model. Most importantly, when the vertical phase separation occurs, the numerical SCF calculations give a sharply varying but *not* discontinuous density profile; the discontinuous profile predicted by the Pincus model results from the fact that its $f_\infty(x)$ given by Eq. (5.14) does not include any free-energy penalty for a spatially varying segmental density profile. In spite of all the simplifications used in the Pincus model, however, its segmental density profiles agree fairly well with our numerical SCF calculations.

Fig. 5.4 further suggests that wether or not the vertical phase separation occurs in a brush at a given temperature is affected by its chain-grafting density σ_0. As $\phi_A(x)$ monotonically decreases with increasing x in a brush, only when

$\phi_0 > \phi_+$ (within the Pincus model) can the vertical phase separation occur. Since ϕ_0 increases with increasing σ_0 as shown in Fig. 5.10 according to the Pincus model , thus increasing σ_0 leads to the vertical phase separation as shown in Fig. 5.4. The effects of σ_0 on the vertical phase separation can also be seen from the variation of brush height h vs. σ_0. The non-monotonic variation shown in Fig. 5.5 is the signature of the vertical phase separation, as pointed out by Baulin and Halperin.[22] We also see from Fig. 5.5 that at this temperature the scaling of h with σ_0 of PNIPAM brushes in water, at both small and large grafting densities, is different from that of polymer brushes with upper critical solution temperatures in either a good ($h \propto \sigma_0^{1/3}$) or a poor ($h \propto \sigma_0$)[24] solvent.

The chain length N also affects the vertical phase separation of PNIPAM brushes in water. Fig. 5.6 shows the brush segmental density profiles obtained from our numerical SCF calculations with three different N, all at $T = 28°C$ and $\sigma_0 = 0.072$. The results obtained from the Pincus model are also included for comparison, which are again in good agreement with the numerical SCF results. We note the following within the Pincus model: First, ϕ_0 is the same for brushes at the same σ_0 but with different N; this can be seen by re-writing Eq. (5.13) as

$$\sigma_0 = \frac{C}{2}\int_0^{\phi_0} \frac{\phi_A(x)}{\sqrt{\mu_\infty(\phi_0) - \mu_\infty(\phi_A(x))}} \frac{\partial f_\infty^2(\phi_A(x))}{\partial \phi_A(x)^2} \mathrm{d}\phi_A(x) \qquad (5.15)$$

where $C = \sqrt{8/3\pi^2}$, and the right-hand-side of Eq. (5.15) depends on ϕ_0 only. Second, both the maximum brush height H and the location x_d where the density profile exhibits a discontinuity, when expressed in units of a, are proportional to N, so is the outer layer thickness $H - x_d$; according to Eq. (5.12), we have $x_d = \sqrt{\mu_\infty(\phi_0) - \mu_\infty(\phi_\pm)}N/C$ and $H = \sqrt{\mu_\infty(\phi_0) - \mu_\infty(0)}N/C$, where the bulk

polymer concentrations $\phi_{\pm}$ of the two coexisting phases depend on T only. This indicates that the vertical phase separation is more pronounced for longer chains.

5.3.3 Thermal Response: Numerical SCF Results

While using the Pincus model to study the thermo-response of PNIPAM brushes in water is simple and instructive, in the following we investigate systematically the thermo-response using the more accurate numerical SCF calculations. The thermo-response of PNIPAM brushes in water is characterized by the variation of h vs. T.

Effects of Chain-Grafting Density σ_0

Fig. 5.7(a) shows the thermal response of PNIPAM brushes with $N = 300$ at different grafting densities σ_0. As σ_0 being increased, the temperature T_m where brushes exhibit maximum thermal response $(\partial^2 h/\partial T^2)|_{T=T_m} = 0$ is observed to shift to lower values. This is better elucidated by Fig. 5.7(b) where $\partial h/\partial T)$ is plotted. In order to explain this we choose $\sigma_0 = 0.024$ and $\sigma_0 = 0.1036$ as two examples to show how the segmental density profiles evolves with temperature.

In Fig. 5.8(a), brushes show extended morphology at $T = 20°C$. As temperature raises, the solvent quality slowly deteriorate making the segmental density near the substrate slowly increases. According to the Eq. 5.11, such reallocation of segments will reduce the brush height. However such change is small in this temperature range and brush structures still remain extended up to $T = 27°C$ which is already above T_c. As temperature further increases to $T = 28°C$ the segmental density near the substrate exhibits a sudden increase, and at $T = 29°C$ such segmental enrichment develops into an step-like inner

layer which will cause a further decrease in brush height according to Eq. 5.11. Therefore brush shows maximum thermal response at $T > T_c$.

Fig. 5.8(b) shows how the segmental density profiles changes with temperature at a higher grafting density. At $T = 20°C$ brush also shows extended morphology similar to Fig. 5.8(a). However, the solvent quality has deteriorated at $T = 20°C$ here comparing to the situation at small grafting densities and as the result the brush is less extended. This can be seen from Fig. 5.7(c) showing the scaling of brush height with respect to grafting density at $T = 20°C$. The scaling coefficient at low grafting densities is close to 1/3 which is in agreement with the good solvent condition. At high grafting densities, however, the scaling is far off from the "one third power law" indicating that the solvent can no longer be regarded as good solvent. Such deterioration in solvent quality is due to the concentration dependent $\chi(\phi_A)$. As shown in Fig. 5.1, the solvent quality is good at $T = 20°C$ only when the segmental density is small. Also, at high grafting density a slight increase in temperature, in this case to $T = 23°C < T_c$, will reduce the solvent quality enough so that segmental profiles start showing enrichment near the substrate. Correspondingly the maximum thermal response is to happen around this temperature. Also, due to the less extended profile at $T = 20°C$, the magnitude of the thermal response is going to be smaller compare to that at low grafting densities.

From the two examples we can see that T_m happens at temperatures where brush profiles change from extended morphology to "two-layer" type morphology. It is usually accompanied by a fast increase in the segmental density near the substrate. Considering that the relation between ϕ_0, σ_0 and T has been

conveniently given by Eq. 5.15, the Pincus model can thus provide a simple way to look at how the grafting density affect the brush thermal response.

Fig. 5.10 shows ϕ_0 calculated from Eq. 5.15 as a function of T at different grafting densities. For the purpose of reference, the bulk phase data is also included in the figure with T plotted with respect to ϕ_0. T_m can be roughly located at the temperature where $\partial\phi_0/\partial T$ is at maximum. When grafting density is low, ϕ_0 is small at $T = 20^oC$ so that the brush is in a good solvent condition. The solvent quality slightly decreases when temperature increases. In this process, ϕ_0 will slowly increase until at a temperature higher than T_c it becomes larger than ϕ_-. Once this happens, ϕ_0 will leap to a value greater than ϕ_+ at the temperature, causing a sudden change in brush height. Therefore sharp thermal response happens at $T > T_c$ at low grafting density, which is what happens for $\sigma_0 = 0.006$ and 0.024 in Fig. 5.7(a). At higher grafting density, the solvent quality deteriorate faster as temperature being raised. ϕ_0 experiences a quick increase at $T < T_c$, which in turn leads to a fast change in brush height. This is what happens in the cases of $\sigma_0 = 0.05263$, 0.07067 and 0.10363 in Fig. 5.7(a), where $T_m < T_c$. If the grafting density is very high, the solvent quality is bad enough even at $T = 20^oC$ so that the brushes exhibit "two-layer" type morphologies. Raising temperature in this situation will only slightly modify the brush profiles as shown in Fig. 5.8(c), and as the result very little change in brush height will be observed.

One thing to note is that in the above discussions on the shifting of T_m, the chain length N is an irrelevant parameter under the Pincus model, which means that in the Pincus model T_m depends only on the grafting density σ_0.

In the next section, we will then investigate how the chain length will play its role in affecting the thermal response of PNIPAM brushes at constant grafting density.

Effects of Chain Length N

Fig. 5.11 shows the effects of chain length N on the thermal response of PNIPAM brushes at $\sigma_0 = 0.036$ from numerical SCF calculations. T_m is observed to be at $T \approx 28^oC$ for all three cases, independent of N, as shown by the inset figure. This is in agreement with the prediction by the Pincus model. Also under the Pincus model, if we renormalize x by x/N in Eq. 5.12 and 5.13, brush height h can be shown to scale with N at a constant grafting density σ_0 at all temperatures. If we quantify the magnitude of brush thermal response within a temperature range T_1 to T_2 by $\Delta h \equiv h(T_2) - h(T_1)$, then Δh will also scale with N. This says that brushes of longer chains will experience more change in brush height within a temperature range.

In order to compare this to our numerical SCF results, we estimate the scaling coefficient of N at three temperatures, $T = 20^oC < T_c$, $T_c < T = 28^oC < T_0$ and $T = 34^oC > T_0$ based on the data shown in Fig. 5.11. The scaling coefficients at $T = 20^oC$ and $T = 34^oC$ have values 0.99 and 0.98 respectively that are close to one. This is because at low grafting density the solvent quality is good at $T = 20^oC$, and at $T = 34^oC$ the brush height can be approximated by $h \approx \sigma N/\phi_+$ given the "step function" shape of brush profiles. At $T = 28^oC$, the coefficient obtained from numerical SCF calculation is 0.91 that is further off from one. This is because in the Pincus model the brush profiles are discontinuous at this temperature as opposed to the continuous profiles given by

numerical SCF calculations.

After all, results from the Pincus model and numerical SCF calculations both indicate that increase in chain length will make the magnitude of thermal response bigger within a temperature range.

5.4 Conclusions

Using both self-consistent field (SCF) calculations and the Pincus model, we investigated the thermal response of one-component PNIPAM (A) brushes in water (S) characterized by the change of brush height with respect to temperature. Our formalism explicitly accounts for the entropy of polymer chains and water molecules. An incompressibility constraint is also imposed requiring the total volume fraction of PNIPAM segments and water molecules be one everywhere in the system. The energetic interactions between the polymer segments and water molecules is modeled by a concentration-dependent Flory-Huggins interaction parameter $\chi(\phi_A)$, obtained through fitting the measured demixing temperature of bulk PNIAPM water solution to the binodal curve from the Flory-Huggins theory, as reported by Afroz et. al,.

The vertical phase separation of PNIPAM brushes was first predicted by Baulins and Halperin[22] using the Pincus model at temperature $T = 28°C$. The segmental density profiles from our SCF calculations agrees very well with their results. Both the grafting density σ_0 and polymer chain length N affect the occurrence of the vertical phase separation. We further extend our interests to study how the morphological structure of PNIPAM brushes changes at different

temperatures using both SCF calculations and the Pincus model. Such evolution of the structure with temperature are reflected by the thermal response of the brush height. Our SCF calculations show that the temperature T_m at which such thermal response is maximized is determined by the grafting density σ_0, with T_m shifting to lower values at higher σ_0. Thermal response of brush height is also found at temperatures $T < T_c$, where vertical phase separation does not occur. Our results also show that N does not affect the value of T_m, it instead controls the magnitude of change in brush height. Our SCF results are well explained based on the Pincus model in this work.

Our study provides some guidance to the design of smart surfaces of PNIAPM.

List of Figures

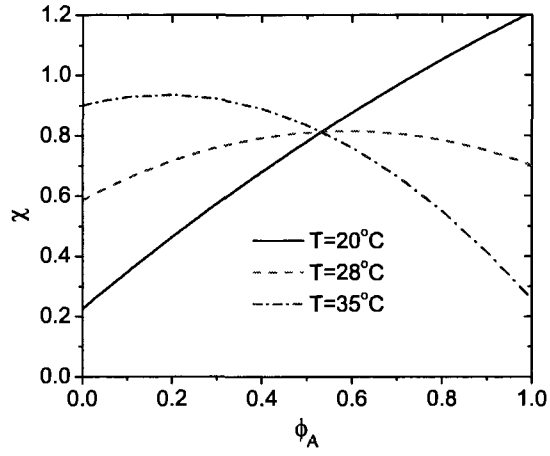

Fig. 5.1: Variation of Flory-Huggins χ parameter with respect to polymer segmental density (volume fraction).

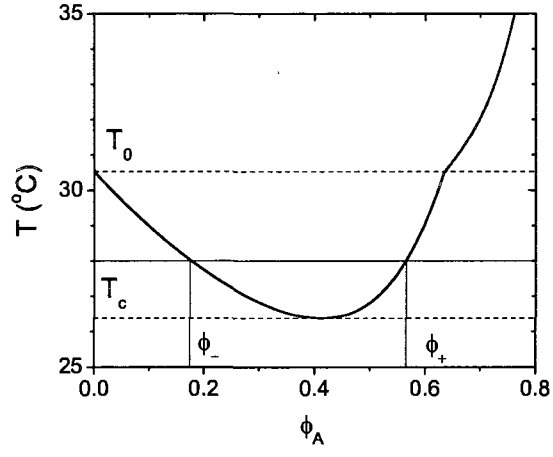

Fig. 5.2: Fitted binodal curve of PNIPAM water solution in bulk condition, using the Flory-Huggins theory with the interaction parameter χ given by Eq. 5.6.

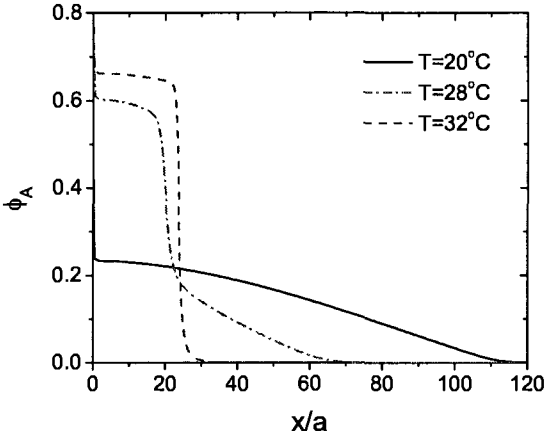

Fig. 5.3: Segmental distributions of a PNIPAM brushes (N=300, σ_0 = 0.0526) obtained from SCF calculations at different temperatures.

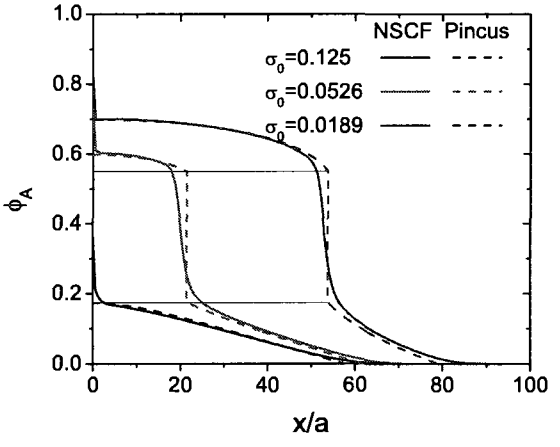

Fig. 5.4: Segmental distributions of a PNIPAM brushes (N=300) obtained from SCF calculations (solid curve) and the Pincus model (dashed curve) at different grafting densities at $T = 28^oC$.

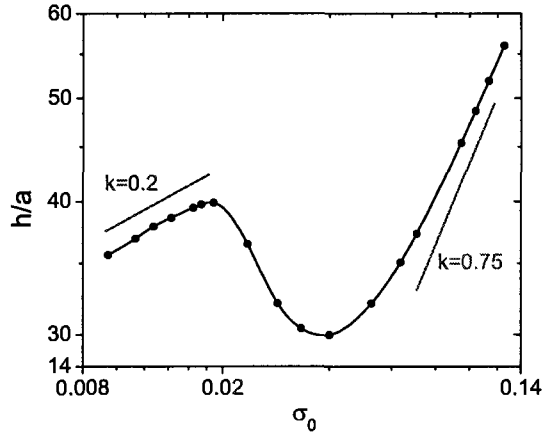

Fig. 5.5: The brush hight calculated from Eq. (5.11) from SCF calculations as a function of the grafting density at $T = 28°C$, N=300.

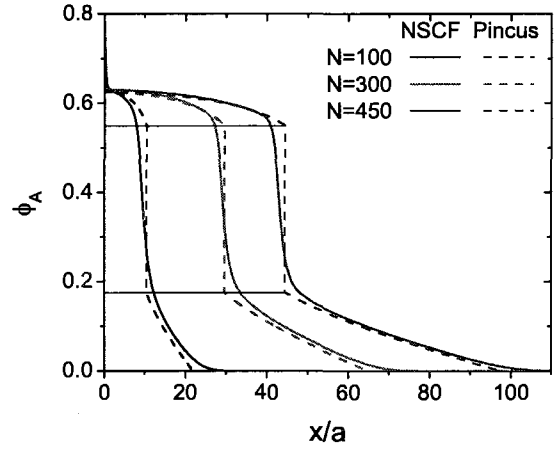

Fig. 5.6: Segmental density profiles of PNIPAM brushes obtained from SCF calculations (solid curve) and the Pincus model (dashed curve) at $T = 28°C$, $\sigma_0 = 0.072$.

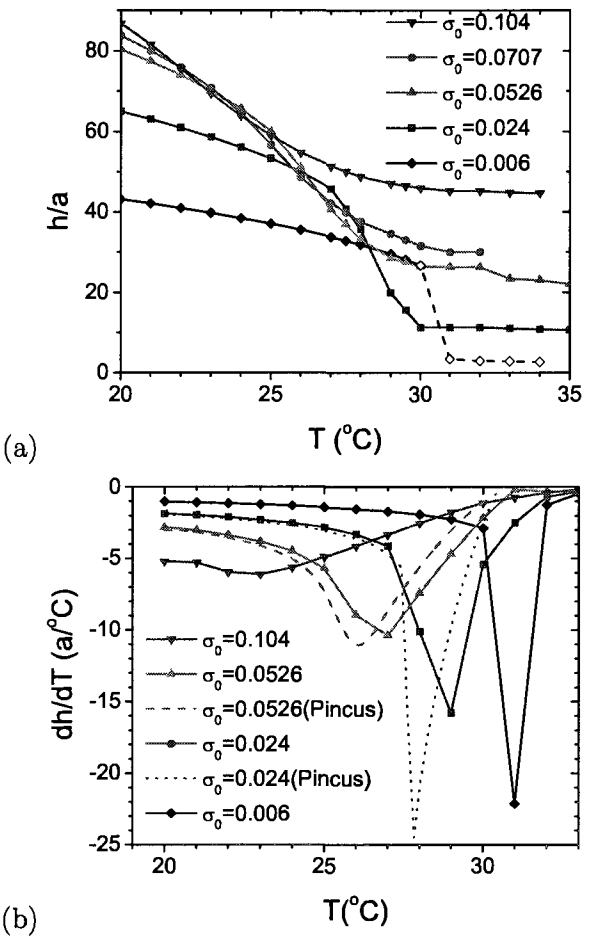

Fig. 5.7: (a) Brush height of PNIPAM brushes obtained from SCF calculations as a function of temperature at different grafting densities with $N = 300$. (b) Variation of $\partial h/\partial T$ at different grafting densities. Results obtained from the Pincus model (dashed and dotted curves) are included for comparison.

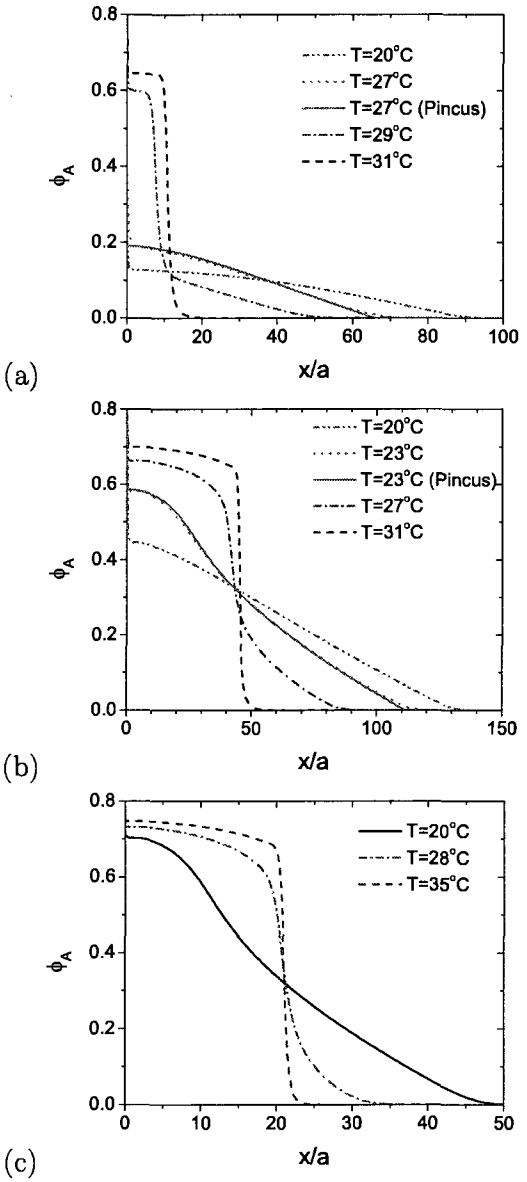

Fig. 5.8: Evolution of segmental distributions of PNIPAM brushes with temperature at (a) $N = 300$, $\sigma_0 = 0.024$; (b) $N = 300$, $\sigma_0 = 0.1036$; (c) $N = 100, \sigma_0 = 0.158$

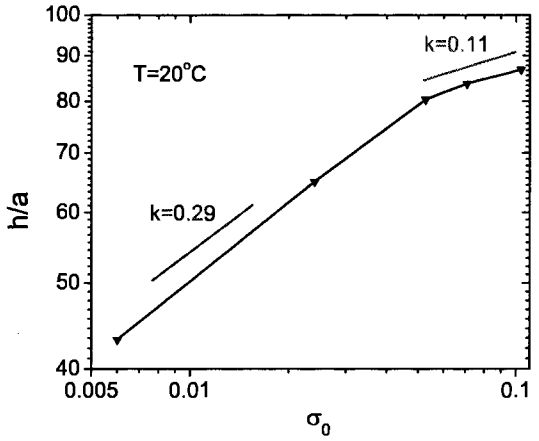

Fig. 5.9: PNIPAM Brush height as a function of grafting density at $T = 20°C$ with $N = 300$, obtained from SCF calculations

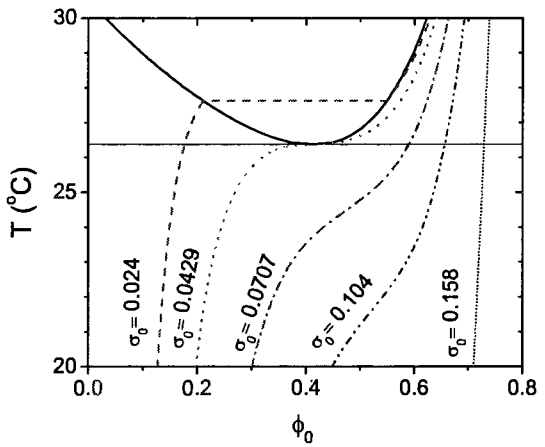

Fig. 5.10: Variation of volume fraction of PNIPAM on the grafting substrate ϕ_0 with temperature, obtained from the Pincus model at different grafting densities.

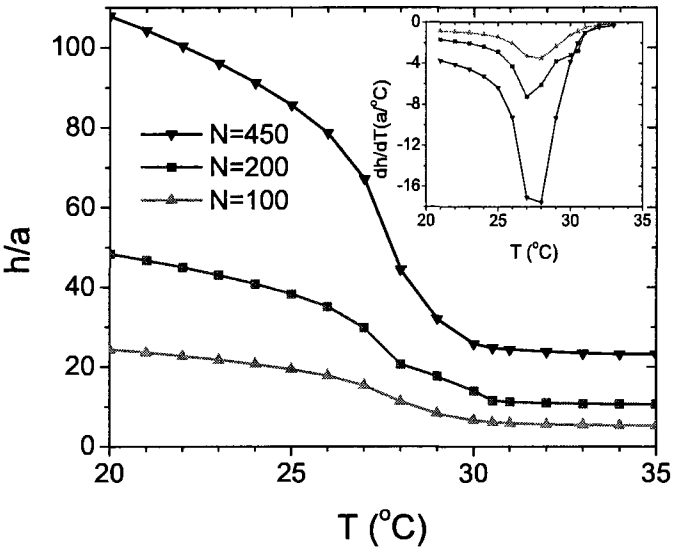

Fig. 5.11: PNIPAM brush height as a function of temperature obtained from SCF calculations with $\sigma_0 = 0.036$, at different chain length N. The inset figure shows the variation of $\partial h/\partial T$ with temperature.

BIBLIOGRAPHY

[1] S. Y. Lin, K. S. Chen and L. R. Chu, Polymer **40**, 6307 (1999).

[2] A. Percot, X. X. Zhu and M. J. Lafleur, Polym. Sci., Polym. Phys. **38**, 907 (2000).

[3] Y. Katsumoto, T. Tanaka, H. Sato, and Y. Ozaki, The Journal of Physical Chemistry A **106**, 3429 (2002).

[4] H. G. Schild, Progress in Polymer Science **17**, 163 (1992).

[5] P. S. Stayton, T. Shimoboji, C. Long, A. Chilkoti, G. Ghen, J. M. Harris and A. S. Hoffman, Nature **378**, 472 (1995).

[6] H. Feil, Y. H. Bae, J. Feijen and S. W. Kim, Journal of Membrane Science **64**, 283 (1991).

[7] Y. S. Park, Y. Ito and Y. Imanishi, Langmuir **14**, 910 (1998).

[8] N. Yamada, T. Okano, H. Sakai, F. Karikusa, Y. Sawasaki and Y. Saku-Rai, Die Makromolekulare Chemie. Rapid communications **11**, 571 (1990).

[9] Y. G. Takei, T. Aoki, K. Sanui, N. Ogata, Y. Sakurai and T. Okano, Biomaterials **16**, 667 (1995).

[10] H. Kawaguchi, K. Fujimoto and Y. Mizuhara, Colloid Polymer Science **270**, 53 (1992).

[11] P. W. Zhu and D. H. Napper, Journal Of Colloid and Interface Science **164**, 489 (1994).

[12] P. W. Zhu and D. H. Napper, Colloids and Surface A-Physicochemical and Engineering Aspects **113**, 145 (1996).

[13] C. Wu and S. Q. Zhou, **28**, 8381 (1995).

[14] C. Wu and S. Q. Zhou, Physical Review Letters **77**, 3053 (1996).

[15] C. Wu and X. H. Wang, Physical Review Letters **80**, 4092 (1998).

[16] F. Afroze, E. Nies and H. J. Berghmans, Mol. Struct. **55**, 554 (2000).

[17] M. Wagner, F. Brochardwyart, H. Hervet, and P. G. de Gennes, Colloid Polym. Sci. **271**, 621 (1993).

[18] W. L. Mattice, S. Misra and D. H. Napper, Europhys. Lett. **28**, 603 (1994).

[19] S. Mendez, J. G. Curro, J. D. McCoy and G. P. Lopez, **38**, 174 (2005).

[20] A. Matsuyama and F. Tanaka, Journal Of Chemical Physics **94**, 781 (1991). 1991, 94(1), 781

[21] V. A. Baulin and A. Halperin, Macromolecules **35**, 6432 (2002).

[22] V. A. Baulin and A. Halperin, Macromol. Theory Simul. **12**, 549 (2003).

[23] V. A. Baulin, E. B. Zhulina and A. Halperin, J. Chem. Phys. **119**, 10977 (2003).

[24] G. S. Grest and M. Murat, Macromolecules **26**, 3108 (1993)

[25] S. Kidoaki, S. Ohya, Y. Nakayama and T. Matsuda, Langmuir **17**, 2402 (2001).

[26] S. Balamurugan, S. Mendez, S. S. Balamurugan, M. J. O'Brie and G. P. Lopez, Langmuir **19**, 2545 (2003).

[27] H. Yim, M. S. Kent, D. L. Huber, S. Satija, J. Majewski, and G. S. Smith, Macromolecules **36**, 5244 (2003).

[28] H. Yim, M. S. Kent, S. Mendez, S. S. Balamurugan, G. P. Lopez and S. Satija, Macromolecules **37**, 1994 (2004).

[29] H. Yim, M. S. Kent, S. Satija, S. Mendez, S. S. Balamurugan and G. P. Lopez, J. Polym. Sci., Part B: Polym. Phys. **42**, 3302 (2004).

[30] H. Yim, M. S. Kent, S. Satija, S. Mendez, S. S. Balamurugan and G. P. Lopez, Phys. Rev. E **72**, 051801 (2005).

[31] H. Yim, M. S. Kent, S. Mendez, G. P. Lopez, S. Satija and Y. Seo, Macromolecules **39**, 3420 (2006).

[32] K. N. Plunkett, X. Zhu, J. S. Moore and D. E. Leckband, Langmuir **22**, 4259 (2006).

[33] X. Zhu, C. Yan, F. M. Winnik and D. Leckband, **23**, 162 (2007).

[34] G. H. Fredrickson, The Equilibrium Theory of Inhomogeneous Polymers; Oxford University Press, 2006.

[35] Press, W. H.; Teukolsky, S. A.; Vetterling, W. T.; Flannery, B. P. Chap. 4.3 in Numerical Recipes in C: the Art of Scientific Computing, 2nd Ed., Cambridge University Press 2002.

[36] D. Meng, W. Wang, The Journal of Chemical Physics **130**, 134904 (2009).

[37] E. Helfand and Y. Tagami, J. Chem. Phys. **56**, 3592 (1972).

[38] D. Meng, W. Wang, Numerical Mehtods in Self-Consistant Field Calculations of Polymer Brushes (To be published) 2009.

[39] G. Tzeremes, K. O. Rasmussen, T. Lookman and A. Saxena, Phys. Rev. E **65**, 041806 (2002).

[40] Press, W. H.; Teukolsky, S. A.; Vetterling, W. T.; Flannery, B. P. Chap. 9.7 in Numerical Recipes in C: the Art of Scientific Computing, 2nd Ed.; Cambridge University Press, 2002.

[41] P. Pincus, Macromolecules **24**, 2912 (1991).

6. SOLVENT-RESPONSE OF UNCHARGED DIBLOCK COPOLYMER BRUSHES

6.1 Introduction

Smart surfaces, also known as stimuli-responsive surfaces, can respond to very subtle changes in their environment such as temperature, pressure, light, solvent selectivity, ionic strength, salt type, pH, applied electric field, etc.[1–3] The response is manifested by reorganization of the surface structure and composition. Hence, the surface properties (e.g., wettability, adhesion, friction, elasticity, and biocompatibility) can be reversibly tuned between different states by the external stimuli. Such surfaces have diverse applications in many fields, such as colloid stabilization, chemical gates, microfluidic devices, sensors, bioanalysis, drug delivery, biomaterials, molecular lubricants, and imaging technologies.[1–3]

Among various methods of creating smart surfaces, tethering stimuli-responsive polymer chains to a substrate has proved to be effective and versatile.[1–3] The so-called polymer "brush"[4] is formed when the distance between adjacent grafted chains is less than two times the chain radius of gyration so that the excluded-volume interactions between polymer segments force the chains to stretch in the direction perpendicular to the grafting substrate.[5–7] Recent advances in the synthesis of polymer brushes have paved the way for preparing

brushes with controlled thickness, ranging from a few nanometers to several hundreds of nanometers, as well as the preparation of block copolymer brushes of almost any composition.[8,9] Furthermore, the covalently grafted polymers possess thermal and solvent stability under various processing conditions, indispensable for their applications.

Chain conformations in the brush are sensitive to external stimuli; different conformations give rise to different surface properties, thus providing the mechanisms for the smart surfaces to reversibly switch between different states. This has been experimentally demonstrated with homopolymer brushes.[10–12] Two-component polymer brushes, including both mixed homopolymer brushes[13] and block copolymer brushes,[14] however, have been more widely used to create smart surfaces, where the segregation (self-assembly) between the different polymer species is utilized. Since these species can have very different physical and chemical properties, the effects of external stimuli on their spatial arrangement in the brush provide the mechanisms for reversibly tuning the surface properties, which can be over a much wider range than (one-component) homopolymer brushes. Two-component polymer brushes also provide more degrees of freedom for the design of smart surfaces.

In this work we focus on the solvent-response of diblock copolymer brushes on flat substrates, where all the copolymer chains are grafted by the same end (i.e., the A-end). In a solvent selective for the ungrafted (B) block, the B segments dominate the brush surface layer (since the A-ends are grafted, copolymers in the brush may adopt similar conformations even in a non-selective solvent). When the solvent is selective for the A block, the A segments can dominate the surface

layer while B segments are embedded in the brush. In the latter case, it is likely that the B segments segregate into laterally structured clusters; compared to the microphase separation in mixed homopolymer brushes,[15–31] however, diblock copolymer brushes are less studied and their detailed microphase-separated structures are not well understood yet.[32–38]

The response of block copolymer brushes has been studied by various experimental groups.[14,32–35,39–55] Zhao and Brittain first reported the synthesis of poly(styrene-*b*-methylmethacrylate) diblock copolymer brushes via the "grafting from" approach and their reversible changes in water contact angles upon treatment with different solvents;[14] this group also first reported the lateral nano-pattern formation in the brush due to solvent treatment.[39]

In great contrast, few groups have reported theoretical and simulation studies on diblock copolymer brushes. Using 2D lattice self-consistent field (SCF) calculations, Balazs and co-workers studied compatible diblock copolymers (i.e., the Flory-Huggins interaction parameter between A and B segments $\chi_{AB} = 0$), in a solvent selective for A, grafted at a low density.[36,37] They also used scaling arguments to complement their SCF results. Various morphologies were predicted depending on the grafting block (A or B), block lengths, grafting density, and the solubilities of the two blocks.[36,37] They further studied the interactions between two surfaces coated with symmetric diblock copolymers at a low grafting density immersed in a selective solvent.[56] Another relevant theoretical study on diblock copolymer brushes was done by Ferreira and Leibler, who reported 1D continuum SCF calculations of diblock copolymer brushes grafted to an impenetrable substrate in a non-selective, good solvent.[57] They

found that, for large $\chi_{AB} > 0$, the grafted block forms a step-like brush near the substrate while the other block is expelled from this region and forms a parabolic brush as the outer layer. For $\chi_{AB} < 0$, backwards twisted configurations due to the A-B attraction become important, which may lead to collapse of the diblock copolymer brush.[57] Very recently, Yin et al. performed lattice Monte Carlo simulations with simulated annealing to study the morphology of strongly incompatible diblock copolymer brushes in strongly selective solvents.[38] Various morphologies were obtained depending on the chain-grafting density and block lengths. Their results are consistent with available experiments[32–34] and theories.[36,37]

More studies on block copolymer brushes are needed in order to understand not only their microphase-separated structures but also their response to solvents of various quality and selectivity, as well as how various factors such as chain-grafting density, chain length, copolymer composition, A-B incompatibility, etc. affect their solvent response. Such knowledge is essential to the design of smart surfaces best suited for targeted applications. As the first step towards this goal, here we use 1D continuum SCF calculations to study the solvent-response of diblock copolymer brushes; more intensive 3D calculations addressing the possible lateral inhomogeneity in diblock copolymer brushes will be reported in future publications.

6.2 Theoretical Formalism and Numerical Methods

6.2.1 Self-Consistent Field Calculations

Since the polymer self-consistent field (SCF) theory has been well developed, we only summarize our SCF equations here; readers are referred to, e.g., Ref. [58] for detailed derivation and explanation of SCF theory.

In this work we consider the brush formed by diblock copolymers A-B of chain length N all grafted by the A-end onto a flat and impenetrable substrate placed at $x = 0$. The brush is immersed in a small-molecule solvent S. We neglect the energetic preference of the substrate, and assume that all polymer segments have the same density ρ_0 as the solvent molecules and the same statistical segment length a. Our SCF equations are

$$\omega_{\mathrm{A}}(\mathbf{r}) = \chi_{\mathrm{AB}} N \phi_{\mathrm{B}}(\mathbf{r}) + \chi_{\mathrm{AS}} N \phi_{\mathrm{S}}(\mathbf{r}) + \eta(\mathbf{r}) \tag{6.1}$$

$$\omega_{\mathrm{B}}(\mathbf{r}) = \chi_{\mathrm{AB}} N \phi_{\mathrm{A}}(\mathbf{r}) + \chi_{\mathrm{BS}} N \phi_{\mathrm{S}}(\mathbf{r}) + \eta(\mathbf{r}) \tag{6.2}$$

$$\omega_{\mathrm{S}}(\mathbf{r}) = \chi_{\mathrm{AS}} N \phi_{\mathrm{A}}(\mathbf{r}) + \chi_{\mathrm{BS}} N \phi_{\mathrm{B}}(\mathbf{r}) + \eta(\mathbf{r}) \tag{6.3}$$

$$\phi_{\mathrm{A}}(\mathbf{r}) = \frac{\bar{\phi}_{\mathrm{C}}}{Q_{\mathrm{C}}} \int_0^{f_{\mathrm{A}}} \mathrm{d}s q(\mathbf{r}, s) q^*(\mathbf{r}, 1-s) \tag{6.4}$$

$$\phi_{\mathrm{B}}(\mathbf{r}) = \frac{\bar{\phi}_{\mathrm{C}}}{Q_{\mathrm{C}}} \int_{f_{\mathrm{A}}}^1 \mathrm{d}s q(\mathbf{r}, s) q^*(\mathbf{r}, 1-s) \tag{6.5}$$

$$\phi_{\mathrm{S}}(\mathbf{r}) = \frac{\bar{\phi}_{\mathrm{S}}}{Q_{\mathrm{S}}} \exp\left[-\frac{\omega_{\mathrm{S}}(\mathbf{r})}{N}\right] \tag{6.6}$$

$$\phi_{\mathrm{A}}(\mathbf{r}) + \phi_{\mathrm{B}}(\mathbf{r}) + \phi_{\mathrm{S}}(\mathbf{r}) = 1 \tag{6.7}$$

Here $\phi_A(\mathbf{r})$, $\phi_B(\mathbf{r})$ and $\phi_S(\mathbf{r})$ are the normalized (by ρ_0) density (i.e., volume fraction) fields of A, B segments and solvent molecules, respectively; and $\omega_A(\mathbf{r})$, $\omega_B(\mathbf{r})$ and $\omega_S(\mathbf{r})$ are the (purely imaginary) conjugate fields interacting the corresponding species. The (purely imaginary) conjugate field $\eta(\mathbf{r})$ enforces the incompressibility, Eq. (7.10). We use χ_{AB} to denote the Flory-Huggins interaction parameter between A and B segments. Similarly, χ_{AS} and χ_{BS} denote the Flory-Huggins interaction parameters between solvent molecules and A or B segments, respectively; the difference between them characterizes the solvent selectivity. The copolymer composition is denoted by $f_A \equiv N_A/N$, where N_A is the A-block length, and $s \in [0,1]$ denotes the segmental position along the chain contour.

The propagator $q(\mathbf{r},s)$ corresponds to the probability of finding a copolymer chain of length sN that starts from the A-end (where $s=0$) and ends at position $\mathbf{r}$, and is commonly calculated from the following modified diffusion equation (MDE)

$$\frac{\partial q}{\partial s} = \begin{cases} \nabla^2 q - \omega_A(\mathbf{r}) q & \text{for } 0 \le s \le f_A \\ \nabla^2 q - \omega_B(\mathbf{r}) q & \text{for } f_A \le s \le 1 \end{cases} \tag{6.8}$$

with the corresponding initial and boundary conditions discussed later. Similarly, the propagator $q^*(\mathbf{r},t)$ with $t \equiv 1-s$ corresponds to the probability of finding a copolymer chain of length tN that starts from the B-end (where $s=1$) anywhere

in the system and ends at $\mathbf{r}$, and is calculated from the following MDE

$$\frac{\partial q^*}{\partial t} = \begin{cases} \nabla^2 q^* - \omega_{\mathrm{B}}(\mathbf{r}) q^* & \text{for } 0 \le t \le 1 - f_{\mathrm{A}} \\ \nabla^2 q^* - \omega_{\mathrm{A}}(\mathbf{r}) q^* & \text{for } 1 - f_{\mathrm{A}} \le t \le 1 \end{cases} \tag{6.9}$$

An alternative way of calculating $q(\mathbf{r}, s)$ is from the Chapman-Kolmogorov equation (CKE)[59]

$$q(\mathbf{r}, s + \mathrm{d}s) = \begin{cases} \exp[-\mathrm{d}s\omega_{\mathrm{A}}(\mathbf{r})] \int \mathrm{d}\mathbf{r}' \Phi(\mathbf{r} - \mathbf{r}') q(\mathbf{r}', s) & \text{for } 0 \le s \le f_{\mathrm{A}} \\ \exp[-\mathrm{d}s\omega_{\mathrm{B}}(\mathbf{r})] \int \mathrm{d}\mathbf{r}' \Phi(\mathbf{r} - \mathbf{r}') q(\mathbf{r}', s) & \text{for } f_{\mathrm{A}} \le s \le 1 \end{cases} \tag{6.10}$$

where $\Phi(\mathbf{r} - \mathbf{r}') = (4\pi \mathrm{d}s)^{-d/2} \exp(-|\mathbf{r} - \mathbf{r}'|^2 / 4\mathrm{d}s)$ corresponds to the probability for a Gaussian chain to propagate from $\mathbf{r}'$ to $\mathbf{r}$ over a small length of $N\mathrm{d}s$, and d is the dimensionality of the system. The MDE, Eq. (6.8), is actually obtained from the CKE after Taylor expansion, which requires q be continuously differentiable. A similar CKE holds for q^*.

In Eqs. (7.4)$\sim$(7.6), $Q_{\mathrm{C}} = \int \mathrm{d}\mathbf{r} q(\mathbf{r}, 1)/V$, $Q_{\mathrm{S}} = \int \mathrm{d}\mathbf{r} \exp[-\omega_{\mathrm{S}}(\mathbf{r})/N]/V$, $\bar{\phi}_{\mathrm{C}} = \int \mathrm{d}\mathbf{r}[\phi_{\mathrm{A}}(\mathbf{r}) + \phi_{\mathrm{B}}(\mathbf{r})]/V$, and $\bar{\phi}_{\mathrm{S}} = 1 - \bar{\phi}_{\mathrm{C}}$, where V denotes the system volume. Note that we have normalized all the distance by $R_g \equiv a\sqrt{N/6}$ in the above equations.

Assuming lateral homogeneity, we perform 1D calculations in the spatial domain of $0 \le x \le l$, where l is chosen to be large enough such that the total polymer segmental density $\phi_{\mathrm{C}}(x) \equiv \phi_{\mathrm{A}}(x) + \phi_{\mathrm{B}}(x) \le 10^{-5}$ near $x = l$ in all cases. The volume-averaged polymer segmental density $\bar{\phi}_{\mathrm{C}}$ is then related to

the chain-grafting density σ (i.e., number of chains per substrate area of R_g^2) by $\bar{\phi}_C = 6^{1.5}\sigma/\sqrt{N}l$, where we have used $\rho_0 = a^{-3}$. We apply the Dirichlet boundary conditions of $q(x,s) = q^*(x,s) = 0$ at $x = 0$ and l for all s, together with the initial condition of $q(x, s = 0) = \delta(x - a)$ for Eqs. (6.8) and (7.11) (we assume that all the A-ends are fixed at $x = a$ as the substrate is impenetrable to polymers); the initial condition of $q^*(x, t = 0) = 1$ at $0 < x < l$ is also used.

Our SCF theory is similar to those used in Refs. [36, 37, 57]. The use of an explicit solvent (with the incompressibility constraint) instead of an implicit solvent (with the excluded volume parameter) as in Ref. [57] allows us to consider poor-solvent conditions as well as solvent selectivity, and provides more accurate description when $\phi_C(x)$ is large.

6.2.2 Numerical Methods and Calculated Quantities

We use the split-step pseudo-spectral method[60] with the fast sine transforms to solve the MDE. This, however, gives some numerical problems when chains are strongly stretched (e.g., at a high grafting density or in a good solvent), due to the (indifferentiable) δ-function initial condition for q; namely, sufficiently accurate numerical evaluation of $\nabla^2 q$ becomes difficult in such cases, which affects the convergence of SCF equations. We therefore calculate the propagators from the CKE using the Romberg integration[61] in these cases. We note that a similar method has been used in the dynamic mean-field density functional method,[62] where the stencil[63] is used to approximate the integral in Eq. (7.11). Detailed numerical comparisons between solving MDE and CKE will be reported in another paper.[64]

In our calculations, the chain contour is uniformly discretized into 200 steps, and

the spatial domain is uniformly discretized into 256 subintervals. The SCF equations are solved in real space by the Broyden method combined with a globally convergent strategy,[65] and both convergence criteria of $|\phi_{\mathrm{C}}(x) + \phi_{\mathrm{S}}(x) - 1| \leq \epsilon$ and $|\omega_{\mathrm{A}}(x) - \omega_{\mathrm{B}}(x) - \chi_{\mathrm{AB}}N[\phi_{\mathrm{B}}(x) - \phi_{\mathrm{A}}(x)] - (\chi_{\mathrm{AS}} - \chi_{\mathrm{BS}})N\phi_{\mathrm{S}}(x)| \leq \epsilon$ are satisfied at all collocation points with $\epsilon = 10^{-5}$. Here, for given $\omega_{\mathrm{A}}(x)$ and $\omega_{\mathrm{B}}(x)$, Eqs. (7.4) and (7.5) are used to calculate $\phi_{\mathrm{A}}(x)$ and $\phi_{\mathrm{B}}(x)$, respectively, after q and q^* are solved; $\omega_{\mathrm{S}}(x)$ is then calculated as $\omega_{\mathrm{S}}(x) = [\omega_{\mathrm{A}}(x) + \omega_{\mathrm{B}}(x) - \chi_{\mathrm{AB}}N\phi_{\mathrm{C}}(x)]/2 + N[\chi_{\mathrm{AS}}\phi_{\mathrm{A}}(x) + \chi_{\mathrm{BS}}\phi_{\mathrm{B}}(x)] - (\chi_{\mathrm{AS}} + \chi_{\mathrm{BS}})N[1 - \phi_{\mathrm{C}}(x)]/2$; and $\phi_{\mathrm{S}}(x)$ is then calculated from Eq. (7.6). Finally, since the conjugate fields can be shifted by an arbitrary constant without changing the density fields, we set $Q_{\mathrm{C}} = 10^{-3}$ to obtain a unique solution.

Once the SCF equations are solved, we can define the brush height as

$$h = \frac{2\int_0^l \mathrm{d}x\phi_{\mathrm{C}}(x)x}{\int_0^l \mathrm{d}x\phi_{\mathrm{C}}(x)} \tag{6.11}$$

and the surface-layer composition as

$$\phi_{\mathrm{A}}^{SL}(h) = \frac{\int_h^l \mathrm{d}x\phi_{\mathrm{A}}(x)}{\int_h^l \mathrm{d}x\phi_{\mathrm{C}}(x)} \tag{6.12}$$

These two quantities are used to characterize the solvent-response of diblock copolymer brushes.

In SCF calculations, a brush has an exponentially decaying tail, which introduces some ambiguity in defining the brush height. For example, a different

definition of brush height can be

$$h_2 = \sqrt{\frac{3\int_0^l \mathrm{d}x\phi_{\mathrm{C}}(x)x^2}{\int_0^l \mathrm{d}x\phi_{\mathrm{C}}(x)}} \tag{6.13}$$

and $\phi_{\mathrm{A}}^{SL}(h_2)$ can be calculated using Eq. (7.14) with h replaced by h_2. This issue is discussed further in Sec. 6.3.2 below.

6.3 Results and Discussion

6.3.1 Solvent Treatment to Switch Surface Properties

In this work, we treat the diblock copolymer brushes by three different solvents: neutral ($\chi_{\mathrm{AS}} = \chi_{\mathrm{BS}} = 0$), A-like ($\chi_{\mathrm{AS}} = 0$ and $\chi_{\mathrm{BS}} = 0.8$) and B-like ($\chi_{\mathrm{AS}} = 0.8$ and $\chi_{\mathrm{BS}} = 0$), and use the difference in surface-layer composition between the treatment by the A-like and B-like solvents to characterize the surface switchability of the brush.

Fig. 6.1 shows the segmental distributions of a diblock copolymer brush in these solvents. We see that, in the neutral solvent, A and B segments have about the same volume fraction in the region beyond the brush height h marked by the vertical line (referred to as the brush surface layer). In the A-like solvent, the ungrafted (B) block is folded inside the brush to avoid its unfavorable contact with the solvent, and the surface layer is dominated by A segments. In the B-like solvent, however, the grafted (A) block is strongly pushed inside the brush, and the surface layer is dominated by B segments.

Due to our small A-B incompatibility $\chi_{\mathrm{AB}}N = 15$ and chain-grafting den-

sity $\sigma = 0.3$ (this is still in the brush regime, the threshold of which can be taken as $\sigma_c \approx 0.289$ with the regular hexagonal arrangement of grafting points), the profiles in the neutral solvent shown in Fig. 6.1(a) are different from the prediction of Ref. [57], i.e., the grafted block forms a step-like brush near the substrate while the other block is expelled from this region and forms a parabolic brush as the outer layer (at large σ and $\chi_{AB} > 0$).[66] On the other hand, it is interesting to note that, in the B-like solvent, the B segmental density profile $\phi_B(x)$ shown in Fig. 6.1(c) exhibits a small plateau near the grafting substrate; similar results were also obtained in recent Monte Carlo simulations by Yin et al.[38] We attribute this to the presence of a depletion zone near the substrate (i.e., the total polymer segmental density decays towards zero as the substrate is approached, due to our boundary conditions for q), where the volume fraction of the solvent is high according to the incompressibility constraint; the B segments are therefore accumulated near the substrate due to their favorable interaction with the solvent. While the depletion zone always presents in our modeling, such a plateau in $\phi_B(x)$ is not found in the A-like solvent.

Given the different physical and chemical properties of A and B segments, the results shown in Fig. 6.1 suggest that the surface properties of the diblock copolymer brush can be switched by different solvents. This is, however, not always the case; changing the copolymer composition f_A from 0.8 in Fig. 6.1 to 0.5, for example, we find that the brush surface layer is always dominated by B segments regardless of the solvent selectivity (see Fig. 6.2 below). In addition, as shown in Fig. 6.1, different solvent treatments could also lead to significant changes in the brush height. To better design such smart surfaces for their applications, one needs to know how the surface-switching is affected

by various factors. In the following, we investigate the influence of copolymer composition f_A (at either constant chain length N or constant A-block length N_A), chain-grafting density σ, and A-B incompatibility $\chi_{AB}N$ on both the brush height and surface switchability.

6.3.2 Effects of Copolymer Composition

Here we use a chain-grafting density $\sigma = 0.3$, and in most cases a small A-B incompatibility $\chi_{AB}N = 15$. The copolymer composition f_A is changed either by varying N_A at a constant copolymer chain length $N = 150$, or by varying N at a constant A-block length $N_A = 120$; the latter also allows us to examine the effects of N.

At Constant Copolymer Chain Length ($N = 150$)

Fig. 6.2 shows how the surface-layer composition $\phi_A^{SL}(h)$ of diblock copolymer brushes in different solvents changes with f_A at constant $N = 150$; the maximum surface switchability (i.e., the largest difference in $\phi_A^{SL}(h)$ between treatments by the A-like and B-like solvents) is obtained at $f_A \approx 0.8$. In the neutral-solvent case, we see that the larger the f_A, the larger $\phi_A^{SL}(h)$. For $f_A > 0.5$, $\phi_A^{SL}(h)$ in the neutral solvent lies between those in the A-like and B-like solvents, and approaches the former as f_A increases (and vice versa). The surface-switching due to the treatments of the A-like and B-like solvents can therefore be understood as the following: For $f_A \geq 0.7$ this is mainly due to the grafted (A) block which is pushed inside the brush in the B-like solvent (as shown in Fig. 6.1(c)), while for $f_A \leq 0.6$ this is mainly due to the ungrafted (B) block which is folded into the brush in the A-like solvent.

Fig. 6.3(a) shows how the brush height h in different solvents changes with f_A at constant $N = 150$. In the neutral-solvent case, h slightly increases from that of the corresponding homopolymer brush (where $f_A = 0$ or 1, or $\chi_{AB} = 0$), due to the small A-B incompatibility $\chi_{AB}N = 15$ in the diblock copolymer brushes. At a relatively low grafting density of $\sigma = 0.3$, the system is dominated by interactions between the solvent and polymer segments, and the A-B incompatibility only plays a minor role. In both cases of a selective (A-like or B-like) solvent, we see strong effects of f_A on the brush height h; these results can be easily understood in terms of the number of segments in the swollen block preferred by the solvent. In addition, the asymmetry about $f_A = 0.5$ for all the solid curves shown in Fig. 6.3(a) is due to the chain-grafting.

At Constant A-Block Length ($N_A = 120$)

Fig. 6.2 also shows how $\phi_A^{SL}(h)$ in different solvents changes with f_A at constant $N_A = 120$ (i.e., at different N); for $f_A \geq 0.6$, the results are close to those at constant $N = 150$, indicating that the copolymer chain length N only has weak influence on the surface switchability. This is in good agreement with recent experiments by Xu et al., who measured the water contact angle of diblock copolymer brush surfaces after different solvent treatments.[53,54] In their combinatorial study, the height of the grafted block (denoted by h_A) was fixed while that of the ungrafted block (denoted by h_B) varied across a sample, and three samples with different h_A were used. The measured water contact angles were plotted versus h_B in Fig. 6 of Ref. [54], which appeared as distinct curves for different values of h_A. Upon plotting their measured water contact angles versus $h_A/(h_A + h_B)$ (a quantity similar to f_A since at constant unnormalized chain-grafting density (i.e., number of chains per unit area) the brush height

is proportional to the polymer molecular weight in the brush regime), we see that the curves for different values of h_A collapse, suggesting that the copolymer chain length N only has weak influence on the surface switchability. It further shows the maximum surface switchability (i.e., the largest difference in water contact angles between treatments by their A-like and B-like solvents) occurs at $h_A/(h_A + h_B) \approx 0.7$. While the lack of quantitative correspondence between their experiments and our calculations (including that between the water contact angle and $\phi_A^{SL}(h)$) precludes quantitative comparison between the two studies, both of them have indicated significant influence of copolymer composition on the surface switchability.

For the cases of $f_A \leq 0.5$ in the A-like solvent, we see in Fig. 6.2 abnormally large differences between $\phi_A^{SL}(h)$ at $N_A = 120$ and that at $N = 150$, which we attribute to the high sensitivity of ϕ_A^{SL} on the definition of brush height in these cases, instead of the effects of N directly on ϕ_A^{SL}. This is illustrated in Fig. 6.4(a), where $\phi_A^{SL}(h)$ is compared with $\phi_A^{SL}(h_2)$ at constant $N_A = 120$; we see that ϕ_A^{SL} is quite sensitive to the definition of brush height in the cases of $f_A \leq 0.5$ in the A-like solvent. In such cases, the B block collapses but cannot be completely folded into the region of shorter A block; this results in a two-step-like profile of the total segmental density $\phi_C(x)$ in our 1D calculations, which in turn gives a large difference between h and h_2, as shown in Figs. 6.4(b) and 6.4(c). Since a brush has an exponentially decaying tail in SCF calculations, this leads to a large difference between $\phi_A^{SL}(h)$ and $\phi_A^{SL}(h_2)$. 3D calculations, however, are needed to confirm the two-step-like segmental distributions in such cases. Note that large differences between h and h_2 are also found in the B-like solvent for $f_A \leq 0.5$, as shown in Fig. 6.4(b); this, however, does not give rise to

noticeable differences in $\phi_{\rm A}^{SL}$ because both $\phi_{\rm A}^{SL}(h)$ and $\phi_{\rm A}^{SL}(h_2)$ are very close to zero in such cases.

Finally, Fig. 6.3(b) shows how h in different solvents changes with $f_{\rm A}$ at constant $N_{\rm A} = 120$. We see that h decreases with increasing $f_{\rm A}$ in all cases. These results are again easily understood in terms of the number of segments in the swollen block preferred by the solvent. In the neutral-solvent case, our fitting with $h = cN^{\alpha}$ gives the scaling exponent $\alpha \approx 0.70$, which is expected since both blocks are in a good solvent and the small incompatibility $\chi_{\rm AB}N = 15$ plays only a minor role. Similarly, in the B-like solvent, our fitting with $h = c_1 N_{\rm B}^{\alpha} + c_2$ gives $\alpha \approx 0.68$, which is again expected since the grafted (A) block collapses and forms a thin layer near the substrate; the diblock brush is therefore close to a homopolymer (B) brush in a good solvent. This scaling, however, is not obtained in the A-like solvent (except when $f_{\rm A}$ is close to 1) due to the folding of the ungrafted (B) block into the brush, which significantly changes the conformations of the A block.

6.3.3 *Effects of Chain-Grafting Density*

Here we set $N = 150$, $f_{\rm A} = 0.8$, $\chi_{\rm AB}N = 15$, and increase the chain-grafting density σ from 0.3 to 3. The CKE are used to calculate the chain propagators. Figs. 6.5(a) and 6.5(b) show how $\phi_{\rm A}^{SL}(h)$ and h vary with σ, respectively, in different solvents. We see that σ has only weak effects on $\phi_{\rm A}^{SL}(h)$. In particular, $\phi_{\rm A}^{SL}(h)$ slightly decreases with increasing σ in the A-like and neutral solvents. This can be understood by comparing the segmental density profiles in the A-like solvent shown in Figs. 6.1(b) (where $\sigma = 0.3$) and 6.5(c) (where $\sigma = 3$); namely, the denser the brush, the more difficult for the B block to be folded inside the

brush.[67] Further comparisons between the brush segmental density profiles with $\chi_{AB}N = 0$ (data not shown) and 15 in the A-like solvent (both at $\sigma = 3$) confirm that this is indeed mainly due to the chain-grafting density rather than the A-B incompatibility. Similarly, that $\phi_A^{SL}(h)$ increases with increasing σ in the B-like solvent is because the denser the brush the more difficult for the A block to be pushed inside the brush. Increasing σ therefore weakly decreases the surface switchability.

On the other hand, Fig. 6.5(b) shows how h increases with increasing σ. Our fitting with $h = c\sigma^{\beta}$ gives $\beta \approx 0.34$ in both the neutral and A-like solvents. This scaling, however, is not obtained in the B-like solvent, where the major (A) block is in a poor solvent. Finally, for comparison the results obtained from solving the MDE at low grafting densities are also shown in Fig. 6.5, which agree with those obtained from solving the CKE.

6.3.4 *Effects of A-B Incompatibility*

Here we use two chain-grafting densities, $\sigma = 0.3$ and 3. The MDE are used for calculating the chain propagators at $\sigma = 0.3$, while the CKE are used at $\sigma = 3$. We also set $N = 150$ and $f_A = 0.8$, and increase $\chi_{AB}N$ from 0 to 120. Fig. 6.6(a) shows the effects of $\chi_{AB}N$ on $\phi_A^{SL}(h)$, where we see that the systems in the A-like solvent behave quite differently at the low and high grafting densities. At $\sigma = 0.3$, the A-B incompatibility has little effects on the surface-layer composition, because the A-B repulsion plays little role compared to the interactions between the solvent molecules and polymer segments due to the low polymer segmental densities in the system. As σ is increased by ten folds, the effects of A-B incompatibility become much more pronounced.

Particularly, in the A-like solvent, $\phi_{\mathrm{A}}^{SL}(h)$ increases from 0.38 at $\chi_{\mathrm{AB}}N = 40$ to 0.56 at $\chi_{\mathrm{AB}}N = 80$ and then levels off.

The increase of $\phi_{\mathrm{A}}^{SL}(h)$ in the A-like solvent at $\sigma = 3$ can be understood by comparing the segmental density profiles at $\chi_{\mathrm{AB}}N = 15$ and 100 shown in Figs. 6.5(c) and 6.6(b), respectively. At $\chi_{\mathrm{AB}}N = 15$, the brush exhibits a two-layer structure with a B-rich surface layer due to the high grafting density, as discussed in the previous section. At $\chi_{\mathrm{AB}}N = 100$, the much stronger A-B repulsion leads to a stronger segregation between A and B segments; the brush therefore adopts a three-layer structure with a B-rich layer sandwiched between two A-rich layers, and the brush surface is now dominated by A segments, consistent with the solvent selectivity.

On the other hand, Fig. 6.6(a) shows that, in the B-like solvent, $\phi_{\mathrm{A}}^{SL}(h)$ does not change significantly with the A-B incompatibility at both grafting densities. This is because the solvent selectivity already keeps most of the A segments away from the surface layer (i.e., the brush exhibits a two-layer structure with a B-rich surface layer); further segregation between A and B segments due to the A-B incompatibility only slightly reduces the amount of A segments in the surface layer. We are currently performing 3D calculations to investigate the possible lateral inhomogeneity in diblock copolymer brushes.

Finally, the A-B incompatibility has little effects on the brush height (data not shown). This is because the brush height is determined by the overall segmental distribution while the A-B incompatibility affects mainly the segregation between A and B segments.

6.4 Conclusions

We have performed 1D self-consistent field (SCF) calculations in continuum to study the solvent-response of uncharged diblock copolymer A-B brushes. All copolymer chains are grafted by the same (A) end onto a flat and impenetrable substrate that has no preference for the two blocks, and immersed in a small-molecule solvent S. Our formalism explicitly accounts for the entropy of polymer chains and solvent molecules, and the energetic interactions between the polymer segments and solvent molecules (modeled by the Flory-Huggins interaction parameters χ_{AB}, χ_{AS}, and χ_{BS}). An incompressibility constraint is also imposed, which requires the total volume fraction of A, B segments and S be one everywhere in the system. In order to avoid the numerical problems associated with the δ-function initial condition specifying that all A-ends are grafted at a small distance from the impenetrable substrate, we numerically integrate the Chapman-Kolmogorov equations, rather than solving the modified diffusion equations, when chains are strongly stretched (e.g., at a high grafting density or in a good solvent). This gives much better numerical performance of SCF calculations in such cases.

The solvent-response of the diblock copolymer brushes is characterized by the changes of brush height and the surface-layer composition ϕ_A^{SL} (i.e., relative fraction of A segments in the copolymers present in the region above the brush height, referred to as the brush surface layer) in three different solvents: neutral ($\chi_{AS} = \chi_{BS} = 0$), A-like ($\chi_{AS} = 0$ and $\chi_{BS} = 0.8$), and B-like ($\chi_{AS} = 0.8$ and $\chi_{BS} = 0$). We have systematically studied the influence of copolymer composition f_A (volume fraction of A-block in the copolymer), copolymer chain

length N, chain-grafting density σ (number of copolymer chains per substrate area of $Na^2/6$ with a denoting the statistical segment length assumed to be the same for both A and B segments), and A-B incompatibility $\chi_{AB}N$ on the solvent-response of diblock copolymer brushes. Our results show that f_A has significant influence, while N has only weak influence, on the brush surface switchability; the maximum surface switchability (i.e., the largest difference in ϕ_A^{SL} between treatments by the A-like and B-like solvents) is obtained at $f_A \approx 0.8$, regardless of N. This is in good agreement with recent experiments.[53,54] On the other hand, increasing σ weakly decreases the surface switchability. The effects of χ_{AB} are manifested only in the A-like solvent at a high grafting density ($\sigma = 3$), where, as $\chi_{AB}N$ increases, the brush can change from a two-layer structure with a B-rich surface layer to a three-layer structure with a B-rich layer sandwiched between two A-rich layers.

Different solvent treatments can also lead to significant changes in the brush height. The variations of brush height with f_A and N are easily understood in terms of the number of segments in the swollen block preferred by the solvent. The brush height increases with increasing σ, while $\chi_{AB}N$ has little effects on the brush height. That a brush has an exponentially decaying tail in SCF calculations could lead to some ambiguity in defining the brush height and correspondingly the surface-layer composition.

Our work can provide some guidance to the design of smart surfaces from diblock copolymer brushes best suited for targeted applications. On the other hand, when at least one of the blocks is charged, other stimuli such as ionic strength, pH, and applied electric field can also be used to switch the brush

surface. These will be the topics of our future publications.

List of Figures

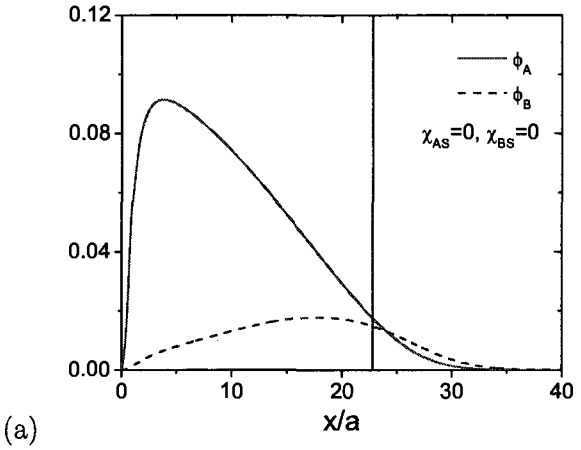

(a)

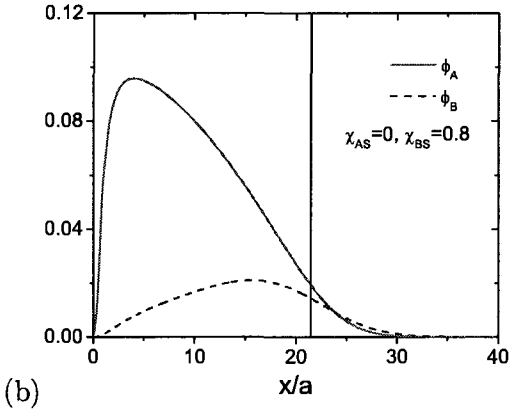

(b)

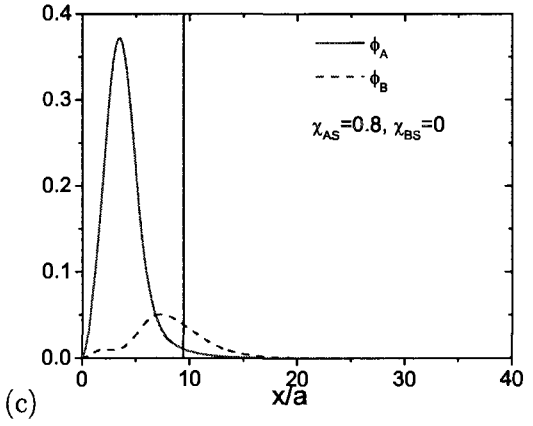

(c)

Fig. 6.1: Segmental distributions of a diblock copolymer brush (N=150, f_A=0.8, σ = 0.3, and $\chi_{AB}N$ = 15) in (a) the neutral solvent, (b) the A-like solvent, and (c) the B-like solvent. The vertical line in each plot marks the brush height h.

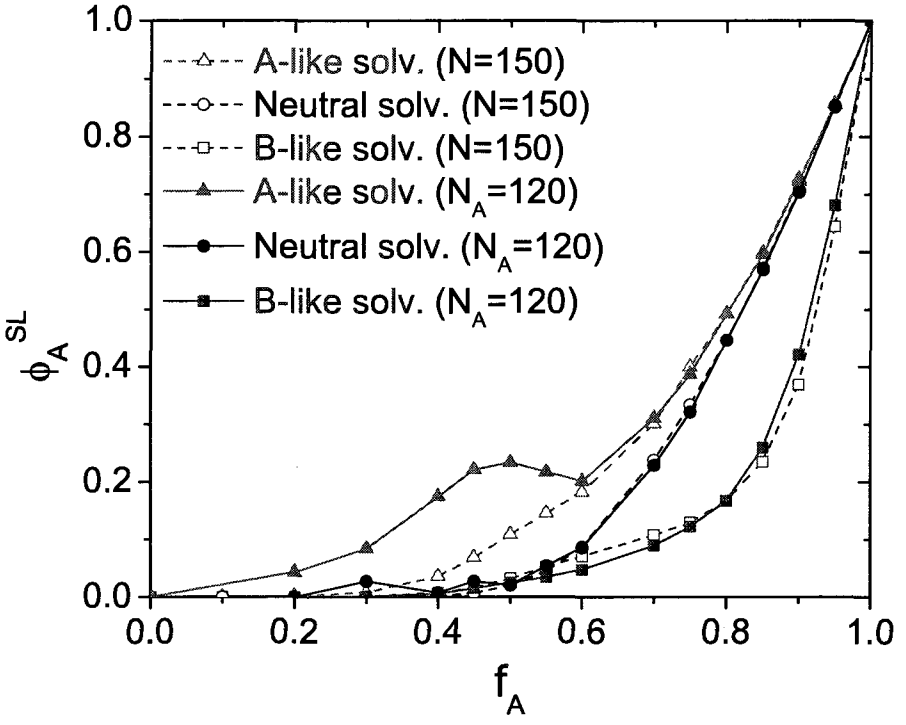

Fig. 6.2: Effects of copolymer composition f_A on the surface-layer composition $\phi_A^{SL}(h)$ of diblock copolymer brushes in different solvents. $\sigma = 0.3$ and $\chi_{AB}N = 15$.

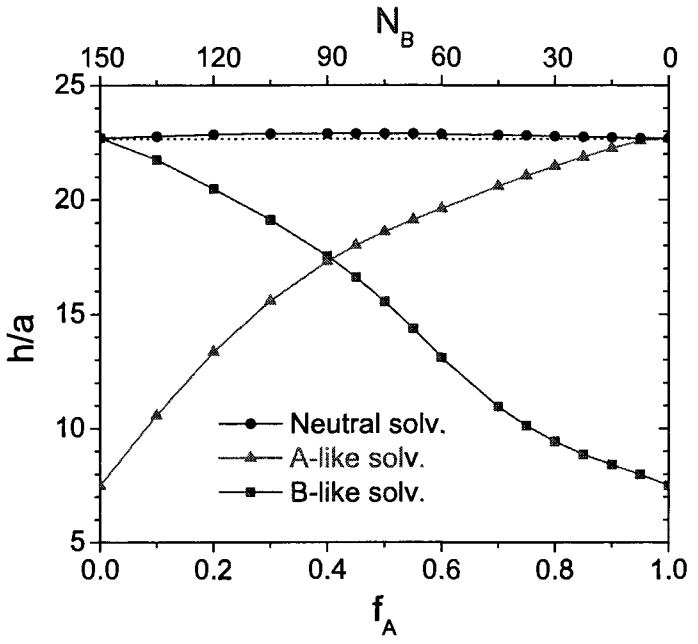

(a)

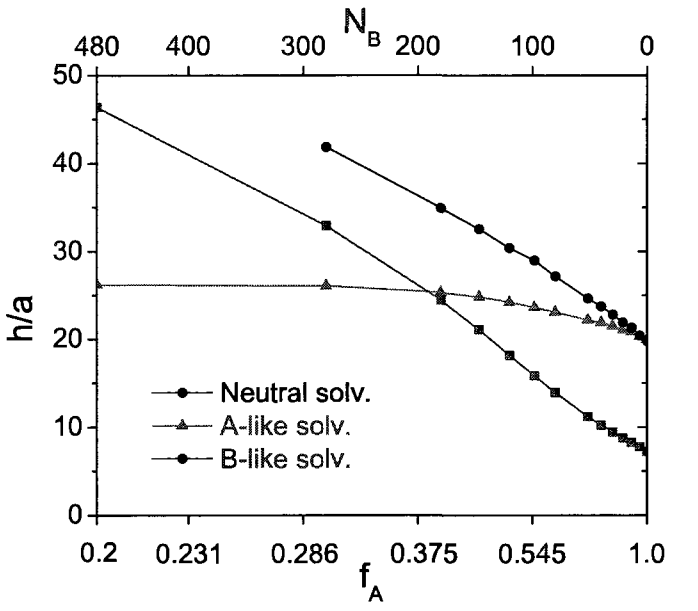

(b)

Fig. 6.3: Effects of copolymer composition f_A on the diblock copolymer brush height h in different solvents at (a) a constant copolymer chain length $N = 150$ and (b) a constant A-block length $N_A = 120$. $\sigma = 0.3$ and $\chi_{AB}N = 15$. The dotted horizontal line in part (a) marks the brush height of the corresponding homopolymer brush (i.e., $\chi_{AB} = 0$) in the neutral solvent.

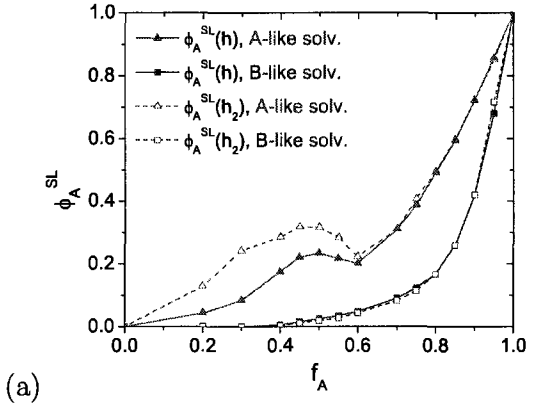

(a)

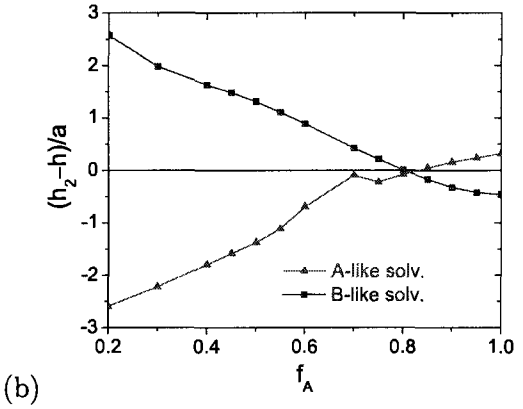

(b)

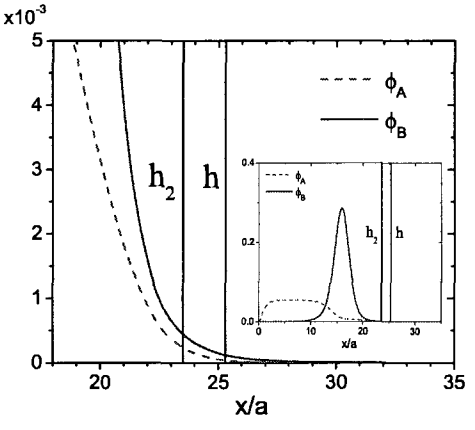

(c)

Fig. 6.4: (a) Effects of different definitions of brush height, h and h_2, on the calculated surface-layer composition ϕ_A^{SL} of diblock copolymer brushes in different solvents. (b) Difference between h and h_2 of diblock copolymer brushes in different solvents. (c) Segmental distributions in the exponentially decaying tail of a diblock copolymer brush (with $f_A = 0.4$) in the A-like solvent. The inset shows the complete segmental distributions of the brush. In all cases, $N_A = 120$, $\sigma = 0.3$, and $\chi_{AB}N = 15$.

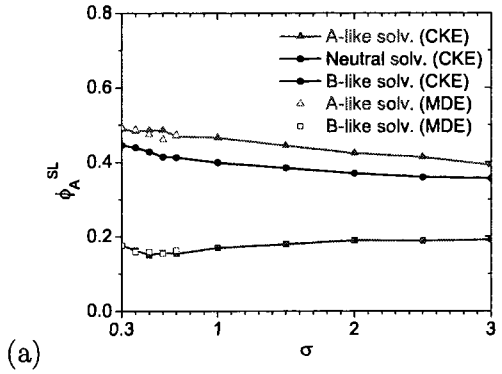

(a)

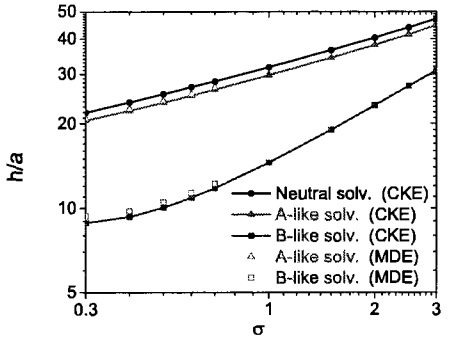

(b)

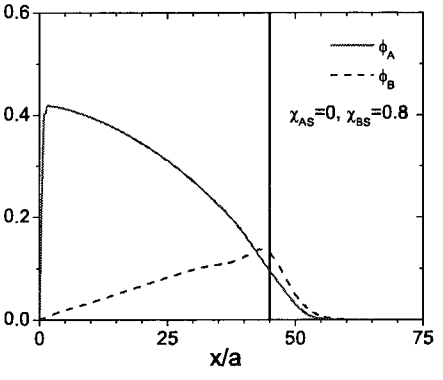

(c)

Fig. 6.5: Effects of chain-grafting density σ on (a) the surface-layer composition $\phi_{\mathrm{A}}^{SL}(h)$ and (b) the brush height h of diblock copolymer brushes in different solvents. The results obtained from solving the modified diffusion equations (MDE) at low σ are also compared with those from solving the Chapman-Kolmogorov equations (CKE) in parts (a) and (b). Part (c) shows the brush segmental distribution in the A-like solvent at $\sigma = 3$. In all cases, $N = 150$, $f_{\mathrm{A}} = 0.8$, and $\chi_{\mathrm{AB}}N = 15$.

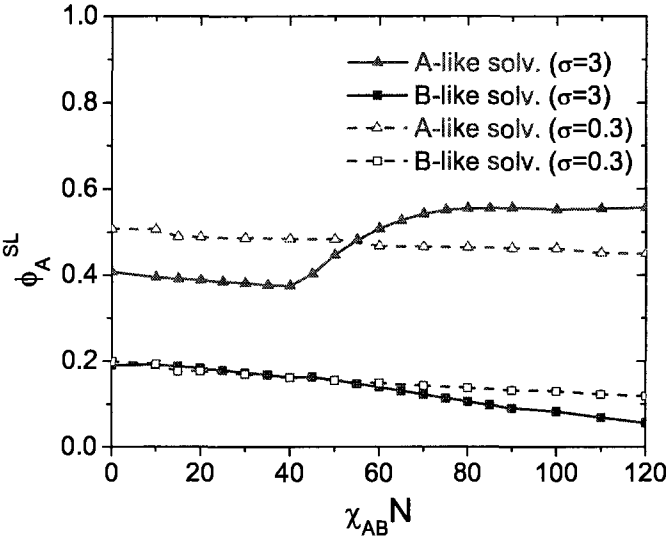

(a)

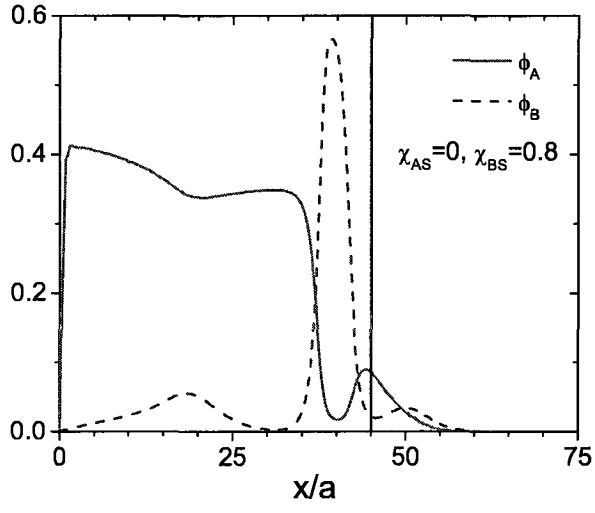

(b)

Fig. 6.6: (a) Effects of A-B incompatibility $\chi_{AB}N$ on the surface-layer composition $\phi_A^{SL}(h)$ in different solvents at two chain-grafting densities σ. (b) The brush segmental distribution in the A-like solvent at $\chi_{AB}N = 100$ and $\sigma = 3$. In all cases, $N = 150$ and $f_A = 0.8$.

BIBLIOGRAPHY

[1] T. P. Russell, Science **297**, 964 (2002).

[2] I. Luzinov, S. Minko, and V. V. Tsukruk, Prog. Polym. Sci. **29**, 635 (2004).

[3] Y. Liu, L. Mu, B. H. Liu, and J. L. Kong, Chem. Eur. J. **11**, 2622 (2005).

[4] W. J. Brittain and S. Minko, J. Polym. Sci., Part A: Polym. Chem. **45**, 3505 (2007).

[5] S. T. Milner, Science **251**, 905 (1991).

[6] A. Halperin, M. Tirrell, and T. P. Lodge, Adv. Polym. Sci. **100**, 31 (1992).

[7] I. Szleifer and M. A. Carignano, Adv. Chem. Phys. **94**, 165 (1996).

[8] B. Zhao and W. J. Brittain, Prog. Polym. Sci. **25**, 677 (2000).

[9] W. J. Brittain, S. G. Boyes, A. M. Granville, M. Baum, B. K. Mirous, B. Akgun, B. Zhao, C. Blickle, and M. D. Foster, Adv. Polym. Sci. **198**, 125 (2006).

[10] T. L. Sun, G. J. Wang, L. Feng, B. Q. Liu, Y. M. Ma, L. Jiang, and D. B. Zhu, Angew. Chem. Int. Ed. **43**, 357 (2004).

[11] S. Moya, O. Azzaroni, T. Farhan, V. L. Osborne, and W. T. S. Huck, Angew. Chem. Int. Ed. **44**, 4578 (2005).

[12] F. Zhou and W. T. S. Huck, Chem. Commun. **48**, 5999 (2005).

[13] A. Sidorenko, S. Minko, K. Schenk-Meuser, H. Duschner, and M. Stamm, Langmuir **15**, 8349 (1999).

[14] B. Zhao and W. J. Brittain, J. Am. Chem. Soc. **121**, 3557 (1999).

[15] P. Y. Lai, J. Chem. Phys. **100**, 3351 (1994).

[16] G. Brown, A. Chakrabarti, and J. F. Marko, Europhys. Lett. **25**, 239 (1994).

[17] K. G. Soga, M. J. Zuckermann, and H. Guo, Macromolecules **29**, 1998 (1996).

[18] L. Wenning, M. Muller, and K. Binder, Europhys. Lett. **71**, 639 (2005).

[19] C. Chen, N. Dan, S. Dhoot, M. Tirrell, J. Mays, and H. Watanabe, Isr. J. Chem. **35**, 41 (1995).

[20] C. Singh, G. T. Pickett, and A. C. Balazs, Macromolecules **29**, 7559 (1996).

[21] P. Y. Lai, Chin. J. Phys. **31**, 569 (1993).

[22] T. A. Witten and S. T. Milner, Mat. Res. Soc. Symp. Proc. **177**, 37 (1990).

[23] J. F. Marko and T. A. Witten, Phys. Rev. Lett. **66**, 1541 (1991).

[24] E. S. C. Ching and T. A. Witten, Europhys. Lett. **19**, 687 (1992).

[25] H. Dong, J. Phys. II **3**, 999 (1993).

[26] J. F. Marko and T. A. Witten, Macromolecules **25**, 296 (1992).

[27] M. Muller, Phys. Rev. E **65**, 030802 (2002).

[28] S. Minko, M. Muller, D. Usov, A. Scholl, C. Froeck, and M. Stamm, Phys. Rev. Lett. **88**, 035502 (2002).

[29] S. Minko, I. Luzinov, V. Luchnikov, M. Muller, S. Patil, and M. Stamm, Macromolecules **36**, 7268 (2003).

[30] J. R. Roan, Int. J. Mod. Phys. B **18**, 2469 (2004).

[31] J. R. Roan, Phys. Rev. Lett. **96**, 248301 (2006).

[32] S. A. Prokhorova, A. Kopyshev, A. Ramakrishnan, H. Zhang, and J. Ruhe, Nanotechnology **14**, 1098 (2003).

[33] S. Santer and J. Ruhe, Polymer **45**, 8279 (2004).

[34] M. R. Tomlinson and J. Genzer, Langmuir **21**, 11552 (2005).

[35] H. Xiong, J. X. Zheng, R. A. Van Horn, K.-U. Jeong, R. P. Quirk, B. Lotz, E. L. Thomas, W. J. Brittain, and S. Z. D. Cheng, Polymer **48**, 3732 (2007).

[36] E. B. Zhulina, C. Singh, and A. C. Balazs, Macromolecules **29**, 6338 (1996).

[37] E. B. Zhulina, C. Singh, and A. C. Balazs, Macromolecules **29**, 8254 (1996).

[38] Y. H. Yin, P. C. Sun, B. H. Li, T. H. Chen, Q. H. Jin, D. T. Ding, and A. C. Shi, Macromolecules **40**, 5161 (2007).

[39] B. Zhao, W. J. Brittain, W. S. Zhou, and S. Z. D. Cheng, J. Am. Chem. Soc. **122**, 2407 (2000).

[40] R. A. Sedjo, B. K. Mirous, and W. J. Brittain, Macromolecules **33**, 1492 (2000).

[41] B. Zhao and W. J. Brittain, Macromolecules **33**, 8813 (2000).

[42] B. Zhao, W. J. Brittain, W. S. Zhou, and S. Z. D. Cheng, Macromolecules **33**, 8821 (2000).

[43] X. X. Kong, T. Kawai, J. Abe, and T. Iyoda, Macromolecules **34**, 1837 (2001).

[44] M. Baum and W. J. Brittain, Macromolecules **35**, 610 (2002).

[45] S. G. Boyes, W. J. Brittain, X. Weng, and S. Z. D. Cheng, Macromolecules **35**, 4960 (2002).

[46] W. X. Huang, J. B. Kim, G. L. Baker, and M. L. Bruening, Nanotechnology **14**, 1075 (2003).

[47] A. M. Granville, S. G. Boyes, B. Akgun, M. D. Foster, and W. J. Brittain, Macromolecules **37**, 2790 (2004).

[48] H. Y. Zhao, B. P. Farrell, and D. A. Shipp, Polymer **45**, 4473 (2004).

[49] A. M. Granville and W. J. Brittain, Macromol. Rapid Commun. **25**, 1298 (2004).

[50] J. N. Kizhakkedathu, K. R. Kumar, D. Goodman, and D. E. Brooks, Polymer **45**, 7471 (2004).

[51] A. M. Granville, S. G. Boyes, B. Akgun, M. D. Foster, and W. J. Brittain, Macromolecules **38**, 3263 (2005).

[52] D. J. Hu, Z. P. Cheng, J. Zhu, and M. L. Zhu, Polymer **46**, 7563 (2005).

[53] C. Xu, T. Wu, J. D. Batteas, C. M. Drain, K. L. Beers, and M. J. Fasolka, Appl. Surf. Sci. **252**, 2529 (2006).

[54] C. Xu, T. Wu, C. M. Drain, J. D. Batteas, M. J. Fasolka, and K. L. Beers, Macromolecules **39**, 3359 (2006).

[55] G. Sakellariou, M. Park, R. Advincula, J. W. Mays, and N. Hadjichristidis, J. Polym. Sci., Part A: Polym. Chem. **44**, 769 (2006).

[56] C. Singh and A. C. Balazs, Macromolecules **29**, 8904 (1996).

[57] P. G. Ferreira and L. Leibler, J. Chem. Phys. **105**, 9362 (1996).

[58] G. H. Fredrickson, The Equilibrium Theory of Inhomogeneous Polymers, Oxford University Press, 2006.

[59] E. Helfand and Y. Tagami, J. Chem. Phys. **56**, 3592 (1972).

[60] G. Tzeremes, K. O. Rasmussen, T. Lookman, and A. Saxena, Phys. Rev. E **65**, 041806 (2002).

[61] W. H. Press, S. A. Teukolsky, W. T. Vetterling, and B. P. Flannery, Chap. 4.3 in Numerical Recipes in C: the Art of Scientific Computing, 2nd Ed., Cambridge University Press, 2002.

[62] J. G. E. M. Fraaije, B. A. C. van Vlimmeren, N. M. Maurits, M. Postma, O. A. Evers, C. Hoffmann, P. Altevogt, and G. Goldbeckwood, J. Chem. Phys. **106**, 4260 (1997).

[63] N. M. Maurits, J. G. E. M. Fraaije, P. Altevogt, and O. A. Evers, Comput. Theor. Polym. Sci. **6**, 1 (1996).

[64] D. Meng and Q. Wang, in preparation (2009).

[65] W. H. Press, S. A. Teukolsky, W. T. Vetterling, and B. P. Flannery, Chap. 9.7 in Numerical Recipes in C: the Art of Scientific Computing, 2nd Ed., Cambridge University Press, 2002.

[66] For example, the parameter values of $nv = 0.1$ and $n\chi_{AB} = 0.1$ used in Fig. 1 of Ref. [57] correspond to $\chi_{AS} = \chi_{BS} = -11.34$ and $\chi_{AB}N = 2268$ (with $N = 100$ and $\sigma = 0.3$), respectively, in our formalism; these numbers are inversely propotional to σ at constant N.

[67] In the neutral solvent, the folding of B-block into the brush is due to the chain conformational entropy instead of solvent selectivity.

7. STIMULI-RESPONSE OF CHARGED DIBLOCK COPOLYMER BRUSHES

7.1 Introduction

The central issue of using polymer brushes to make "smart" surfaces is to investigate what and how external stimuli can be used to trigger the conformational or compositional changes in brushes in a desired way. Compared to neutral polymer brushes, charged polymer brushes (polyelectrolyte), which consist of charged polymer chains densely grafted onto a surface, experience conformational and compositional changes in response to external stimuli such as the the solution pH value, ionic strength as well as the presence of external electric field in addition to solvent quality. Such simultaneous manifestation of nonelectrostatic short range interaction and electrostatic forces in the polyelectrolyte brushes provide peculiar behavior of these systems, making the polyelectrolyte brushes a very promising candidate material to be used in applications such as colloid stabilization and flocculation, friction weakening, selective membrane modification, drug delivery, nano actuator, etc.[16]

Due to such great practical interests, the polyelectrolyte brush system has been actively studied both theoretically[1–13] and experimentally[17–34] in the recent years. In particular, great progress has been made using theory approaches.

The pioneering work by Pincus[3] demonstrated the scaling laws of polyelectrolyte brushes in two regimes. In the "osmotic" brush regime with dense and strongly charged brushes, the brush height is independent of salt concentration. Mobile ions are trapped inside the brush compensating the immobilized charge of the tethered polyions and the brush is swollen due to osmotic pressure of counterions from inside. In the Pincus regime, with sparse tethering of the polyions and low degrees of ionization, the electrostatic attraction between the tethered polyions and mobile ions is not sufficient to trap the counterions inside the brush, thus the distribution of counterions is far beyond brush region. The scaling dependences for the thickness and other brush properties are different. Such observations had also been supported by other scaling studies.[5,8]

In addition to the scaling behavior, the intrinsic structure of polyelectrolyte brushes (brush profiles) is also of great interest to study. By invoking the local electroneutrality approximation, Zhulina *et al.*[6] used a free energy model that includes the elastic free energy (adopted from strong stretching neutral polymer chains), electrostatic interaction (approximated by the Debye-Huckel approximation). The brush profiles is then obtained by minimizing the free energy with respect to the polymer segmental density. This model is valid for situations where counterions are strongly trapped inside brush, so that all polyions are completely compensated by the neighboring counterions. For the opposite situations where counterions are distributed far beyond the brush region, Borisov *et al.*[11] approximate the polyelectrolyte brushes as a "capacitor" model in which the polyions and counterions are assumed to be distributed within two separate regions. Under the approximation of strong stretching polymer chains, the full scale self-consistent analytical model uniting the two extreme cases is proposed

in the later work by Zhulina *et al.*[9] Along with the analytical models, numerical self-consistent calculations had been conducted on polyelectrolyte brushes by several authors,.[1,2,12,13] With very few approximations, the numerical SCF calculations is advantageous to the analytical models in that they are not limited to special cases and are able to provide much accurate and complete information about the brush segmental profiles, distributions of polymer segment, mobil ions as well as electrostatic potentials.

Compared to the large volume of work published on charged homopolymer brushes, very little study has been reported on two-component polyelectrolyte brushes including charged mixed brushes and charged diblock copolymer brushes. Compared to charged homopolymer brush, two-component polyelectrolyte brushes exhibit the responses in both conformational and compositional change such that a much richer stimuli-response behavior can be expected. Compared to mixed brushes, diblock copolymer brushes eliminate the influence of nonuniform distribution of grating points of different homopolymer chains, and can therefore produce more uniform surfaces. In this section, our focus is to use numerical self-consistent calculations to study for a charged diblock copolymer brushes how external stimuli, such as the solvent quality, solution pH value, solution ionic strength and the presence of external electric field affect the brush conformation as well as its surface-layer composition that are the two most important factors characterizing the stimuli-response of polymer brushes.

7.2 Theoretical Formalism and Numerical Methods

Self-Consistent Field Theory for Charged Diblock Copolymer Brushes

Based on self-consistent field (SCF) theory for polyelectrolytes system,[14] we summarize our SCF equations here; readers are referred to Ref. [14] for detailed derivation and explanation of this theory.

The diblock copolymer polyelectrolyte brushes are formed by diblock copolymers A-B of chain length N all grafted by the A-end onto a flat and impenetrable substrate placed at $x = 0$. We only consider monovalent systems with one of the two blocks charged. The brush is immersed in a small-molecule solvent S, and is in equilibrium with a bulk solution with salt concentration of $c_{s,b}$. We assume that the counterions from polyelectrolytes are identical to the ions from salt that carry the same type of charges, and denote cations by $+$ and anions by $-$. We also assume that the dielectric constant of the system ϵ is position independent. We further neglect the short-range interactions for all small ions and the energetic preference of the substrate, assume that all polymer segments have the same density ρ_0 as the solvent molecules and the same statistical segment length a, and ignore the volume of small ions. Our SCF equations are

$$\omega_{\mathrm{A}}(\mathbf{r}) = \chi_{\mathrm{AB}} N \phi_{\mathrm{B}}(\mathbf{r}) + \chi_{\mathrm{AS}} N \phi_{\mathrm{S}}(\mathbf{r}) + \eta(\mathbf{r}) \tag{7.1}$$

$$\omega_{\mathrm{B}}(\mathbf{r}) = \chi_{\mathrm{AB}} N \phi_{\mathrm{A}}(\mathbf{r}) + \chi_{\mathrm{BS}} N \phi_{\mathrm{S}}(\mathbf{r}) + \eta(\mathbf{r}) \tag{7.2}$$

$$\omega_{\mathrm{S}}(\mathbf{r}) = \chi_{\mathrm{AS}} N \phi_{\mathrm{A}}(\mathbf{r}) + \chi_{\mathrm{BS}} N \phi_{\mathrm{B}}(\mathbf{r}) + \eta(\mathbf{r}) \tag{7.3}$$

$$\phi_{\mathrm{A}}(\mathbf{r}) = \frac{\bar{\phi}_{\mathrm{C}}}{Q_{\mathrm{C}}} \int_0^{f_{\mathrm{A}}} \mathrm{d}s q(\mathbf{r}, s) q^*(\mathbf{r}, 1-s) \tag{7.4}$$

$$\phi_{\mathrm{B}}(\mathbf{r}) = \frac{\bar{\phi}_{\mathrm{C}}}{Q_{\mathrm{C}}} \int_{f_{\mathrm{A}}}^{1} \mathrm{d}s q(\mathbf{r}, s) q^{*}(\mathbf{r}, 1-s) \tag{7.5}$$

$$\phi_{\mathrm{S}}(\mathbf{r}) = \frac{\bar{\phi}_{\mathrm{S}}}{Q_{\mathrm{S}}} \exp\left[-\frac{\omega_{\mathrm{S}}(\mathbf{r})}{N}\right] \tag{7.6}$$

$$\phi_{+}(\mathbf{r}) = c_{s,b} \exp\left[-\psi(\mathbf{r})\right] \tag{7.7}$$

$$\phi_{-}(\mathbf{r}) = c_{s,b} \exp\left[\psi(\mathbf{r})\right] \tag{7.8}$$

$$-\phi_{\mathrm{A}}(\mathbf{r}) \frac{\mathrm{d}g_{\mathrm{A}}(\mathbf{r})}{\mathrm{d}\psi(\mathbf{r})} - \phi_{\mathrm{B}}(\mathbf{r}) \frac{\mathrm{d}g_{\mathrm{B}}(\mathbf{r})}{\mathrm{d}\psi(\mathbf{r})} + \phi_{+}(\mathbf{r}) - \phi_{-}(\mathbf{r}) + \frac{\epsilon}{N} \nabla^{2} \psi(\mathbf{r}) = 0 \tag{7.9}$$

$$\phi_{\mathrm{A}}(\mathbf{r}) + \phi_{\mathrm{B}}(\mathbf{r}) + \phi_{\mathrm{S}}(\mathbf{r}) = 1 \tag{7.10}$$

Here $\phi_{\mathrm{A}}(\mathbf{r})$, $\phi_{\mathrm{B}}(\mathbf{r})$, $\phi_{\mathrm{S}}(\mathbf{r})$ are the normalized (by ρ_0) density fields of A, B segments and solvent molecules, respectively; and $\omega_{\mathrm{A}}(\mathbf{r})$, $\omega_{\mathrm{B}}(\mathbf{r})$ and $\omega_{\mathrm{S}}(\mathbf{r})$ are the conjugate fields interacting with the corresponding species. $\psi(\mathbf{r})$ is the (purely imaginary) electrostatic potential in units of $k_B T/e$. The (purely imaginary) field $\eta(\mathbf{r})$ imposes the incompressibility constraint Eq. (7.10). We use χ_{AB} to denote the Flory-Huggins interaction parameter between A and B segments. Similarly, χ_{AS} and χ_{BS} denote the Flory-Huggins interaction parameters between solvent molecules and A or B segments, respectively. The copolymer composition is denoted by $f_{\mathrm{A}} \equiv N_{\mathrm{A}}/N$, where N_{A} is the A-block length, and $s \in [0,1]$ denotes the segmental position along the chain contour. $\alpha_{\mathrm{P}} \in [0,1]$ where $\mathrm{P} = \mathrm{A}, \mathrm{B}$ denotes the degree of ionization of the P type segment. For smeared charge distribution (strongly dissociating polyelectrolytes) α_{P} corresponds to the charge fraction on each P type segment p_{P}; for annealed charge distribution (weakly dissociating polyelectrolytes) α_{P} corresponds to the probability of a segment of type P being in the dissociated state. Hence, $g_{\mathrm{P}}(\mathbf{r}) \equiv -\alpha_{\mathrm{P}} \upsilon_{\mathrm{P}} \psi(\mathbf{r})$ for smeared charge, and $g_{\mathrm{P}}(\mathbf{r}) \equiv \ln[1-\alpha_{\mathrm{P}}+\alpha_{\mathrm{P}}\exp(-\upsilon_{\mathrm{P}}\psi(\mathbf{r}))]$ for annealed charge.

The propagator $q(\mathbf{r}, s)$ corresponds to the probability of finding a copolymer chain of length sN that starts from the A-end (where $s = 0$) and ends at position $\mathbf{r}$, and is calculated from the following Chapman-Kolmogorov equation (CKE)[15]

$$q(\mathbf{r}, s+\mathrm{d}s) = \begin{cases} \exp[-\mathrm{d}s(\omega_{\mathrm{A}}(\mathbf{r}) - Ng_{\mathrm{A}}(\mathbf{r}))] \int \mathrm{d}\mathbf{r}'\Phi(\mathbf{r}-\mathbf{r}')q(\mathbf{r}', s) & \text{for } 0 \le s \le f_{\mathrm{A}} \\ \exp[-\mathrm{d}s(\omega_{\mathrm{B}}(\mathbf{r}) - Ng_{\mathrm{B}}(\mathbf{r}))] \int \mathrm{d}\mathbf{r}'\Phi(\mathbf{r}-\mathbf{r}')q(\mathbf{r}', s) & \text{for } f_{\mathrm{A}} \le s \le 1 \end{cases} \tag{7.11}$$

with the corresponding initial and boundary conditions discussed later. $\Phi(\mathbf{r} - \mathbf{r}') = (4\pi\mathrm{d}s)^{-d/2} \exp(-|\mathbf{r} - \mathbf{r}'|^2/4\mathrm{d}s)$ corresponds to the probability for a Gaussian chain to propagate from $\mathbf{r}'$ to $\mathbf{r}$ over a small length of $N\mathrm{d}s$, and d is the dimensionality of the system. Similarly, the propagator $q^*(\mathbf{r}, t)$ with $t \equiv 1 - s$ corresponds to the probability of finding a copolymer chain of length tN that starts from the B-end (where $s = 1$) anywhere in the system and ends at $\mathbf{r}$, and it satisfies

$$q^*(\mathbf{r}, t+\mathrm{d}t) = \begin{cases} \exp[-\mathrm{d}t(\omega_{\mathrm{B}}(\mathbf{r}) - Ng_{\mathrm{B}}(\mathbf{r}))] \int \mathrm{d}\mathbf{r}'\Phi(\mathbf{r}-\mathbf{r}')q^*(\mathbf{r}', s) & \text{for } 0 \le t \le 1 - f_{\mathrm{A}} \\ \exp[-\mathrm{d}t(\omega_{\mathrm{A}}(\mathbf{r}) - Ng_{\mathrm{A}}(\mathbf{r}))] \int \mathrm{d}\mathbf{r}'\Phi(\mathbf{r}-\mathbf{r}')q^*(\mathbf{r}', s) & \text{for } 1 - f_{\mathrm{A}} \le t \le 1 \end{cases} \tag{7.12}$$

The commonly used modified diffusion equation in calculating the chain propagators is actually obtained from the CKE after Taylor expansion, which requires q be continuously differentiable.

In Eqs. (7.4)$\sim$(7.6), $Q_{\mathrm{C}} = \int \mathrm{d}\mathbf{r} q(\mathbf{r}, s)q^*(\mathbf{r}, 1-s)/V$, $Q_{\mathrm{S}} = \int \mathrm{d}\mathbf{r} \exp[-\omega_{\mathrm{S}}(\mathbf{r})/N]/V$; $\bar{\phi}_{\mathrm{C}} = \int \mathrm{d}\mathbf{r}[\phi_{\mathrm{A}}(\mathbf{r}) + \phi_{\mathrm{B}}(\mathbf{r})]/V$, and $\bar{\phi}_{\mathrm{S}} = 1 - \bar{\phi}_{\mathrm{C}}$, where V denotes the system

volume. Note that by writing Eqs. (7.7),(7.8) we have set $\psi(x \to \infty) = 0$. We normalized all the distance by $R_g \equiv a\sqrt{N/6}$ in the above equations. The normalized dielectric constant is defined as $\epsilon \equiv 3k_BT\epsilon/(2\pi\rho_0 e^2 a^2)$, where the unnormalized dielectric constant ϵ is in units of $4\pi\epsilon_0$, and $\epsilon_0 = 8.8854 \times 10^{-12}(\mathrm{A \cdot s})^2/(\mathrm{J \cdot m})$ is the permittivity of vacuum.

Assuming lateral homogeneity, we perform 1D calculations in the spatial domain of $0 \leq x \leq l$, where l is chosen to be large enough such that the total polymer segmental density $\phi_C(x) \equiv \phi_A(x) + \phi_B(x) \leq 10^{-5}$, $\psi(x) \leq 10^{-5}$ and $\mathrm{d}\psi(x)/\mathrm{d}x \leq 10^{-5}$ near $x = l$ in all cases. The volume-averaged polymer segmental density $\bar{\phi}_C$ is then related to the chain-grafting density σ (i.e., number of chains per substrate area of R_g^2) by $\bar{\phi}_C = 6^{1.5}\sigma/\sqrt{N}l$, where we have used $\rho_0 = a^{-3}$. We apply the Dirichlet boundary conditions of $q(x,s) = q^*(x,s) = 0$ at $x = 0$ and l for all s, together with the initial condition of $q(x, s = 0) = \delta(x - a)$ for Eqs. (7.11) (we assume that all the A-ends are grafted at $x = a$); the initial condition of $q^*(x, t = 0) = 1$ at $0 < x < l$ is also used. To solve Eq. (7.9), an auxiliary function $\tilde{\psi}(x) = \psi(x) - \psi_0(x)$ is constructed. In the case where $\psi_{SF} \equiv \psi(x = 0)$ is fixed, we set $\psi_0(x) = -\psi_{SF}x/l + \psi_{SF}$ and then the laplace of $\psi(x)$ becomes $\mathrm{d}^2\psi(x)/\mathrm{d}x^2 = \mathrm{d}^2\tilde{\psi}(x)/\mathrm{d}x^2 + \mathrm{d}^2\psi_0(x)/\mathrm{d}x^2$, where $\mathrm{d}^2\psi_0(x)/\mathrm{d}x^2$ can be analytically calculated, the term $\mathrm{d}^2\tilde{\psi}(x)/\mathrm{d}x^2$ however can be calculated using the fast sine transform. This corresponds to applying the Dirichlet boundary condition. On the other hand if instead the surface charge density at the grafting substrate σ_{SF} is fixed, with the knowledge that the surface charge density is related to the electrostatic potential by $-\sigma_{SF}N/\varepsilon = \mathrm{d}\psi(x)/\mathrm{d}x|_{x=0}$, we choose $\psi_0(x)$ such that $\mathrm{d}\psi_0(x)/\mathrm{d}x = \mathrm{x}\sigma_{SF}\mathrm{N}/\varepsilon\mathrm{l} - \sigma_{SF}\mathrm{N}/\varepsilon$. Again, $\mathrm{d}^2\psi_0(x)/\mathrm{d}x^2$ can be analytically calculated, the term $\mathrm{d}^2\tilde{\psi}(x)/\mathrm{d}x^2$ can now be calculated using the

fast cosine transform. This corresponds to applying the Neumann boundary condition.

7.2.1 Numerical Methods and Calculated Quantities

We calculate the propagators from the CKE using the Romberg integration[36] in all cases. In our calculations, the chain contour is uniformly discretized into 200 steps, and the spatial domain is uniformly discretized into 256 subintervals. The SCF equations are solved in real space by the Broyden method combined with a globally convergent strategy,[37] and the convergence criteria of $|\phi_C(x) + \phi_S(x) - 1| \leq \epsilon$, $|\omega_A(x) - \omega_B(x) - \chi_{AB}N[\phi_B(x) - \phi_A(x)] - (\chi_{AS} - \chi_{BS})N\phi_S(x)| \leq \epsilon$ and the left hand side of Eq. (7.9)$\leq \epsilon$ are all satisfied at all collocation points with $\epsilon = 10^{-8}$. Here, for given $\omega_A(x)$, $\omega_B(x)$ and $\psi(x)$, Eqs. (7.4) and (7.5) are used to calculate $\phi_A(x)$ and $\phi_B(x)$, respectively, after q and q^* are solved; $\omega_S(x)$ is then calculated from $\omega_S(x) = [\omega_A(x) + \omega_B(x) - \chi_{AB}N\phi_C(x)]/2 + N[\chi_{AS}\phi_A(x) + \chi_{BS}\phi_B(x)] - (\chi_{AS} + \chi_{BS})N[1 - \phi_C(x)]/2$; and $\phi_S(x)$ is then calculated from Eq. (7.6). Finally, since the conjugate fields can be shifted by an arbitrary constant without changing the density fields, we set $Q_C = 10^{-3}$ to obtain a unique solution. The numerical calculations for binary blends brushes stays the same except that we set the discretization along A chain $n_A = 200$ and that for B chain satisfies $n_B/n_A = \beta$ so that $ds = 1/n_A$ for both A and B chains.

Once the SCF equations are solved, we can define the brush height as

$$h = \frac{2\int_0^l dx\phi_C(x)x}{\int_0^l dx\phi_C(x)} \tag{7.13}$$

and the surface-layer composition as

$$\phi_{\mathrm{A}}^{SL}(h) = \frac{\int_h^l \mathrm{d}x\phi_{\mathrm{A}}(x)}{\int_h^l \mathrm{d}x\phi_{\mathrm{C}}(x)} \tag{7.14}$$

These two quantities are used to characterize the stimuli-response of diblock copolymer brushes.

In charged diblock copolymer brushes it is useful to quantify the spreadness of each blocks. We define the spreadness of the P (P= A or B) block as

$$S_{\mathrm{P}} = \sqrt{\frac{1}{\bar{\phi}_{\mathrm{P}} l}\int_0^l (x - c_{\mathrm{P}})^2 \phi_{\mathrm{P}}(x)dx} \tag{7.15}$$

where c_{P} is the mass center of block P, calculated by

$$c_{\mathrm{P}} = \frac{1}{\bar{\phi}_{\mathrm{P}} l}\int_0^l x\phi_{\mathrm{P}}(x)dx \tag{7.16}$$

7.3 Results and Discussion

Diblock copolymer AB brushes show stimulus response upon treatments by solvents preferring different blocks. The response is reflected by the change in brush surface layer composition and brush height. In particular, the change in surface layer composition characterizes the switchability of brush surfaces. According to our previous study,[35] when treated by different solvent the biggest change in brush surface layer composition is observed when the copolymer composition $f_A \simeq 0.8$. For charged DBC brushes, however, due to the presence of charges on polymer chains, other variables can also affect the surface switchability, including the amount of charges on polymer chains, the ionic strength in the solutions

and the external electric field. In this section, we will investigate systematically how each of these variables affects the surface switchability of charged polymer brushes. For comparison, all calculations in this section are under the same conditions as in our neutral brush studies, i.e., $f_{\mathrm{A}} = 0.8$, $\chi_{\mathrm{AB}}N = 15$, and $\sigma = 0.3$. We set $\chi_{\mathrm{AS}} = 0, \chi_{\mathrm{BS}} = 0.8$ for A-like solvent and $\chi_{\mathrm{AS}} = 0.8, \chi_{\mathrm{BS}} = 0$ for B-like solvent. For simplicity we consider the situation that only one of the two polymer blocks (either A or B) is negatively charged and the counterions released by the polymer chains are assumed to carry positive charges.

7.3.1 Effect of Charge

Fig. 7.1 shows the surface-layer composition as a function of the charge fraction on the A block (B block being neutral) in different solvent conditions and salt concentrations under neutral surface condition ($\sigma_{\mathrm{SF}} = 0$). In the B-like solvent, ϕ_{A}^{SL} quickly increases with p_{A} and then levels off. In the A-like solvent ϕ_{A}^{SL} slowly increases with p_{A}, however the magnitude is much smaller than that in the B-like solvent. This makes the difference in ϕ_{A}^{SL} in the two different solvent conditions decrease, which suggests that switching surface layer composition via solvent treatments becomes less effective. This happens because the charges on the A block make the effective solvent quality for A segments better, and in the B-like solvent as the charge fraction increases the effective solvent quality for both blocks will eventually equals each other, as the result the solvent treatment becomes ineffective in switching the surface composition.

To better illustrate this, we apply Flory-Huggins theory to a free chain AB diblock copolymer in B-like solvent ($\chi_{\mathrm{BS}} = 0$) with the A block being charged and for simplicity the two blocks are assumed to be compatible *i.e.*,

$\chi_{AB} = 0$. The free energy of the system can be expressed as

$$f = \frac{\phi}{N}\ln\phi + (1-\phi)\ln(1-\phi) + \chi_{AS} f_A \phi(1-\phi) + (p_A f_A \phi + c_{s,b})\ln(p_A f_A \phi + c_{s,b}) + c_{s,b}\ln c_{s,b} \quad (7.17)$$

with the last two terms accounting for the entropy of small ions. After Taylor expanding the last two terms and combine with the solvent block interaction term, the effective solvent quality for A block can be approximated by $\chi_{AS}^{eff} = \chi_{AS} - p_A^2 f_A / 2c_{s,b}$. As we discussed before, χ_{AS}^{eff} becomes smaller as p_A increases, and vanishes at $p_A = p_{A,\,c} = \sqrt{2c_{s,b}\chi_{AS}/f_A}$, which means that the B-like solvent becomes effectively neutral at this charge fraction. This value agrees well with the charge fraction obtained from SCF calculations when $\phi_A^{SL} = \phi_B^{SL}$, as shown in the Table 7.1.

$c_{s,b}$	$p_{A,\,c}$	p_A at $\phi_A^{SL} = \phi_B^{SL}$
0.002	0.063	0.076
0.02	0.20	0.22
0.2	0.63	0.70

Tab. 7.1: Comparison of $p_{A,\,c}$ calculated using Flory-Huggins theory and p_A (at $\phi_A^{SL} = \phi_B^{SL}$) from self-consistent field calculations at different bulk salt concentrations.

Table 7.1 and Fig. 7.1 also show that, at smaller salt concentration $c_{s,b}$, the charge fraction required to achieve the effective neutral solvent condition becomes smaller, as should be expected. Such a behavior could allow the salt concentration to be used as a stimulus to switch the surface layer composition when the polymer chains are weakly charged. However this tactic will only work when the brush is in B-like solvent. Fig. 7.1 then reveals the complicate interplay

and intricate balance of the effects of charge fraction, salt concentration (ionic strength) and solvent selectivity on switching the brush surface layer properties.

Fig. 7.2 shows the brush surface layer composition as a function of the charge fraction on the B block (A block being neutral) in A-like and B-like solvents and two different salt concentrations, again under neutral surface condition ($\sigma_{SF} = 0$). It's interesting to see that the surface layer composition of A segments increases with p_B in B-like solvent, which is the opposite to what is expected based on the argument of effective solvent quality just established. The brush segmental density profiles at $p_B = 0$ and $p_B = 1$ in B-like solvent are shown in Fig. 7.2. Comparing the two figures, it can be seen that at $p_B = 0$, A block collapses near to the substrate due to the poor solvent quality, and B block dominates the surface layer leading to a small ϕ_A^{SL}. At $p_B = 1$, A block still stays in the collapsed state, however, due to the electro-static repulsion among the charged B-type segments B block spreads out. The degree of block spreading defined by Eq. 7.15 becomes greater as the charge fraction on the B block increases, as shown in Fig. 7.3. Such spreading consequently reduces the volume fraction of the B block in the brush surface layer and thus lead to increased ϕ_A^{SL}.

In conclusion, the response of brushes to solvent treatment will be reduced by charging either A or B block. Such result reflects the two different effects of charges on DBC brushes, i.e., improving the effective solvent quality; spreading the charged block. Sometime the two effects play against each other.

7.3.2 Effect of Solution pH

Unlike the situation of strongly dissociating polymers where the charge fraction on the polymer is constant in solution, the degree of ionization of weakly dissociating polymers depends on the local dissociation equilibrium condition, and such equilibrium conditions will be affected by the solution pH value. As a potential stimulus, it is then of interest to investigate how the charged polymer brushes respond to solution pH changes.

Fig. 7.4 shows surface layer composition of brushes made of weakly dissociating polymer chains as a function of pH value in bulk solution. Because polymers are assumed to be negatively charged, the solution pH value and degree of ionization of polymer segments α_P are related by $pH - pK_P = \log(\alpha_P/(1-\alpha_P))$, where pK_P is the intrinsic dissociation constant of segment of type P. Therefore the increase in pH will increase the degree of ionization of polymer segments leading to more charges on polymer chains. As the result, the results shown in Fig. 7.4 are very similar to the effects of charge fraction in the cases of strongly dissociating polymers brushes. For weakly dissociating DBC brushes, in B-like solvent, a change of one unit in the bulk solution pH can switch surface layer composition significantly, suggesting that the solution pH can be used as a very effective stimulus.

7.3.3 Effect of Applied Electric Field

All of the discussion in the last two sections have been associated with neutral surface condition, where the grafting substrate does not carry any electric charges. For charged DBC brushes, however, applying electric potential on the

substrate is probably the most direct way to switch a brush surface. In this section we will investigate how the electric static potential at the substrate $\psi_{\mathrm{SF}} \equiv \psi(z=0)$ affects the surface layer composition of charged DBC brushes.

We only consider strongly dissociating polymer brushes in this section with only one block (either A or B) charged and the charge fraction $p_{\mathrm{A}} = 0.06$ and $p_{\mathrm{B}} = 0.4$ are chosen. According to Fig. 7.1 and Fig. 7.2, in a bulk salt solution of concentration $c_{s,b} = 0.002$, the brush surface switchability upon solvent treatment (characterized by $\phi^{SL}_{\mathrm{A,A-like}} - \phi^{SL}_{\mathrm{A,B-like}}$) is almost completely missing under the neutral surface condition. For convenience we denote the electric static potential at the substrate ψ_{SF} at neutral surface condition as ψ_0.

Fig. 7.5 and Fig. 7.6 show how the surface layer composition changes when ψ_{SF} is adjusted so that the substrate starts wearing charges. In Fig. 7.5, when $\psi_{\mathrm{SF}} < \psi_0$ the substrate becomes negatively charged. While the charges on the A-block keep the block spread out, the electric static repulsion between A-block and the substrate only keeps the charged block a bit further away from the substrate in both A-like and B-like solvents. Therefore not much changes in surface layer composition is observed in both cases and the surface switchability remains low. As $\psi_{\mathrm{SF}} > \psi_0$, the substrate becomes positively charged, in which situation the A block will be attracted by the grafting substrate. Therefore the A block will starts collapsing near to the substrate as ψ_{SF} increases. In B-like solvent, such collapse is accelerated by the poor solvent quality, therefore a deep drop in ϕ^{SL}_{A} is observed. In A-like solvent, however, the collapse is counteracted by the good solvent quality that keeps a tail part of the A block extended with the B block pushed inside it such that ϕ^{SL}_{A} slightly increases as shown in Fig. 7.7.

With the B block charged, Fig. 7.6 shows that when $\psi_{SF} < \psi_0$, the surface layer composition stays almost constant in both A-like and B-like solvents. To help to understand this Fig. 7.8 shows the comparison of brush density profiles at $\psi_{SF} = -7$ and $\psi_{SF} = \psi_0$ in A-like and B-like solvents respectively. The effects of negative charges on the grafting substrate is to push the B block away from the substrate, while the structures near the brush surface layer stays relatively unchanged. As $\psi_{SF} > \psi_0$ B block becomes attractive to the positively charged substrate, and collapses near to the substrate leaving the brush surface layer completely dominated by A segments as shown in Fig. 7.9. Therefore a sharp increase in ϕ_A^{SL} is observed.

7.4 Conclusion

We have performed 1D self-consistent field (SCF) calculations in continuum to study the stimuli-response of charged diblock copolymer A-B brushes. All copolymer chains are grafted by the same (A) end onto a flat and impenetrable substrate that has no preference for the two blocks, and immersed in a small-molecule solvent S. The system is in equilibrium with a bulk salt solution. We only considered monovalent systems with one of the two blocks charged. Our formalism explicitly accounts for the entropy of polymer chains, small ions and solvent molecules, and the short-range interactions between the polymer segments and solvent molecules (modeled by the Flory-Huggins interaction parameters χ_{AB}, χ_{AS}, and χ_{BS}), and the electro-static interactions in the system. An incompressibility constraint is also imposed, by neglecting the volume of ions this constraint requires the total volume fraction of A, B segments and S be one

everywhere in the system. In order to avoid the numerical problems associated with the δ-function initial condition specifying that all A-ends are grafted at a small distance from the impenetrable substrate, we numerically integrate the Chapman-Kolmogorov equations, rather than solving the modified diffusion equations. This gives much better numerical performance of SCF calculations in such cases.

The stimuli-response of the charged diblock copolymer brushes involves complicate interplay of the effects of different stimuli, namely, charge fraction on polymer chains (or solution pH value for weakly dissociating polymers), solution salt concentration, external electric field and solvent selectivity. We have studied the influence of these stimuli on the brush surface-layer composition ϕ_{A}^{SL} (i.e., relative fraction of A segments in the copolymers present in the region above the brush height, referred to as the brush surface layer) and we found that charges on polymer chains can improve the effective solvent quality for the charged block, while at the same time spread the block. Sometimes, these two effects play against each other in affecting the surface-layer composition. The effects of solution pH value for weakly dissociating polymer brushes are essentially those of the charge fraction for strongly dissociating polymer brushes. Sharp response in surface-layer composition can be achieved by adjusting solution pH. Oppositely charged grafting substrate can switch the brush surface-layer composition abruptly under certain solvent conditions, by attracting the charged block near to the substrate or pushing it away.

However all the influence of these stimuli are effective under certain conditions, it is therefore important to understand the underlying physics in order

to use them to switch the properties of brush surfaces. Our work reveals such subtle balance and can thus provide some guidance to the design of smart surfaces from charged diblock copolymer brushes for targeted applications.

List of Figures

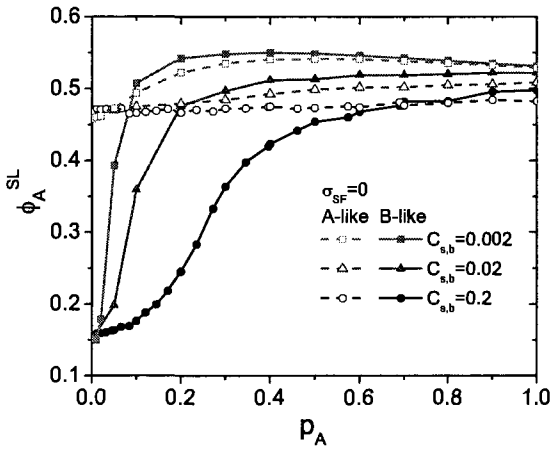

Fig. 7.1: Surface layer composition ϕ_A^{SL} as a function of the charge fraction on the A-block, under neutral surface condition ($\sigma_{SF} = 0$) at different bulk salt concentrations.

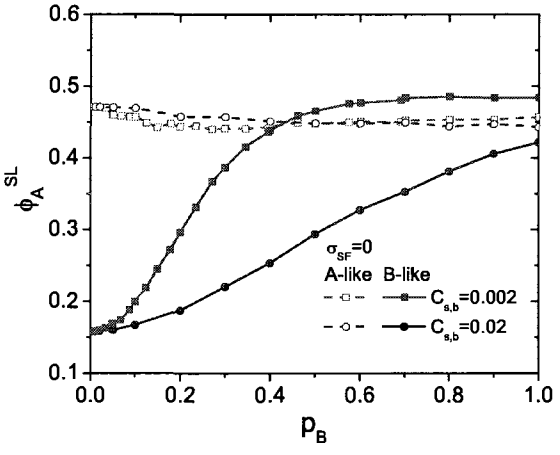

Fig. 7.2: Surface layer composition ϕ_A^{SL} as a function of the charge fraction on the B-block, under neutral surface condition ($\sigma_{SF} = 0$) at different bulk salt concentrations.

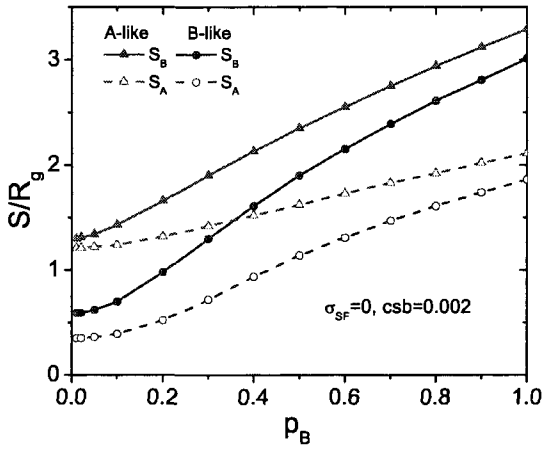

Fig. 7.3: The spreadness of the A and B-block calculated from Eq. 7.15 of DBC brushes as a function of the charge fraction on the B-block under neutral surface condition $\sigma_{SF} = 0$, at $c_{s,b} = 0.002$.

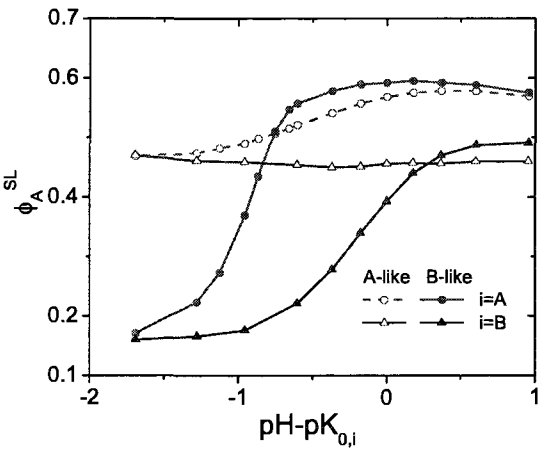

Fig. 7.4: Surface layer composition ϕ_A^{SL} of weakly dissociating DBC brushes as a function of the difference between pH value in bulk solution and intrinsic dissociation constant of the charged specie, under neutral surface condition ($\sigma_{SF} = 0$).

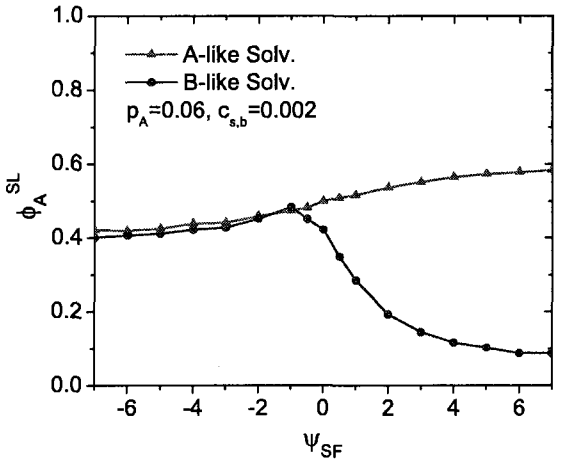

Fig. 7.5: Surface layer composition $\phi_{\mathrm{A}}^{\mathrm{SL}}$ of A-block charged ($p_{\mathrm{A}} = 0.06$) DBC brushes as a function of the electro static potential on the grafting substrate ψ_{SF}, at $c_{s,b} = 0.002$.

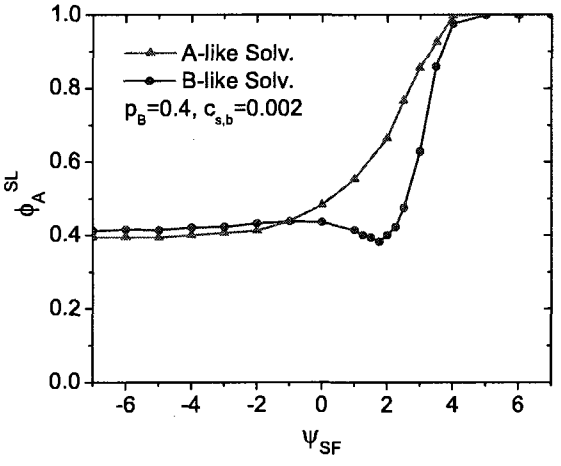

Fig. 7.6: Surface layer composition $\phi_{\mathrm{A}}^{\mathrm{SL}}$ of B-block charged ($p_{\mathrm{B}} = 0.4$) DBC brushes as a function of the electro static potential on the grafting substrate ψ_{SF}, at $c_{s,b} = 0.002$.

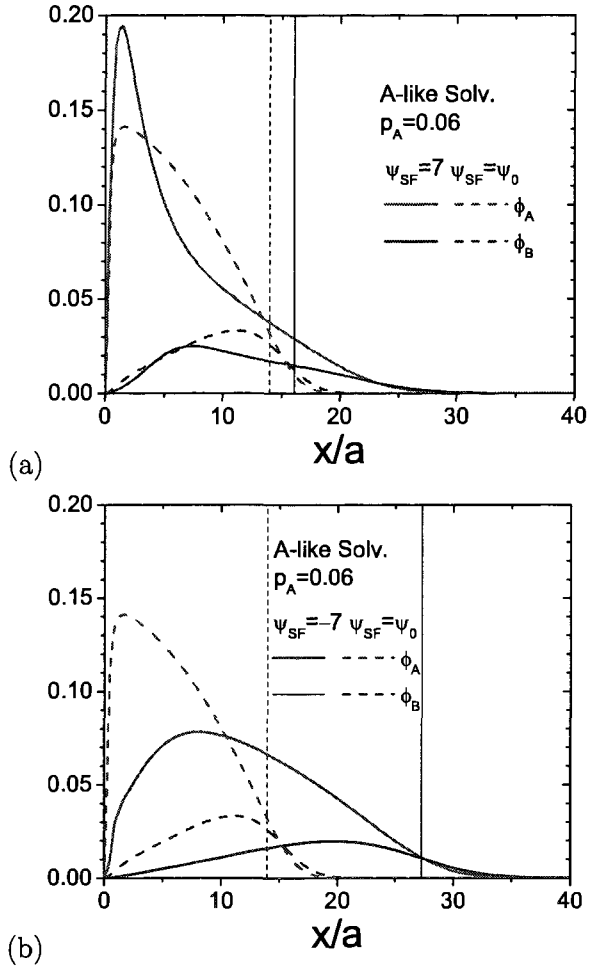

Fig. 7.7: Comparison of segmental density profiles of A-bock charged ($p_A = 0.06$) DBC brushes obtained at neutral surface $\sigma_{SF} = 0$ ($\psi_{SF} = \psi_0$) and (a) positively $\psi_{SF} = 7$ charged surface; (b) negatively charged surface $\psi_{SF} = -7$ in A-like solvent condition. The vertical dashed lines in the two plots indicate the position of brush height for $\psi_{SF} = \psi_0$. The vertical solid lines show the position of brush height for $\psi_{SF} = 7$ and $\psi_{SF} = -7$ in the two plots respectively.

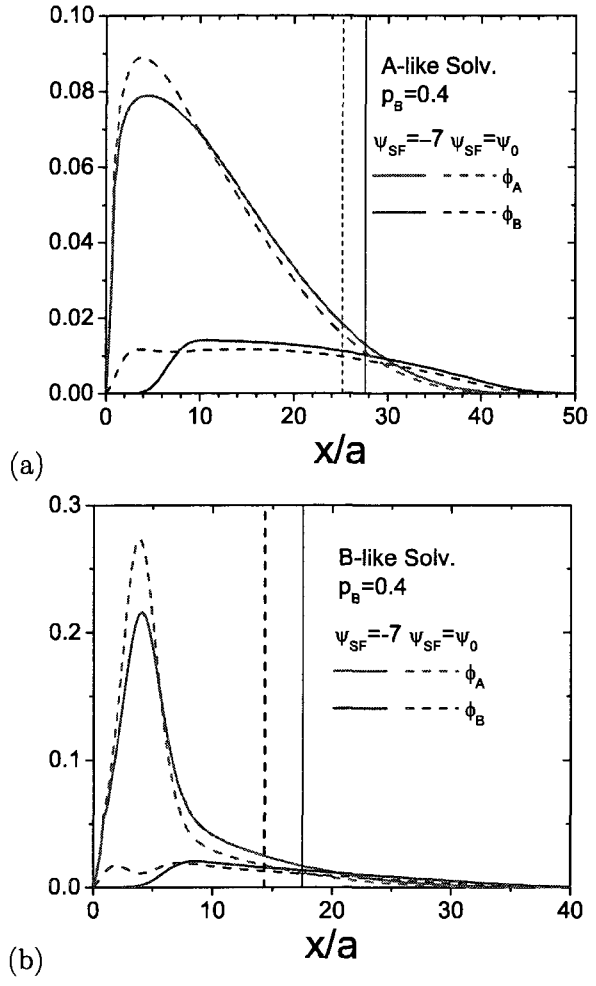

Fig. 7.8: Comparison of segmental density profiles of B-bock charged ($p_B = 0.4$) DBC brushes obtained at neutral surface $\sigma_{SF} = 0$ ($\psi_{SF} = \psi_0$) and negatively charged surface $\psi_{SF} = -7$ in (a) A-like solvent condition; (b) B-like solvent condition. The vertical dashed and solid lines in the two plots indicate the position of brush height for $\psi_{SF} = \psi_0$ and $\psi_{SF} = -7$ respectively.

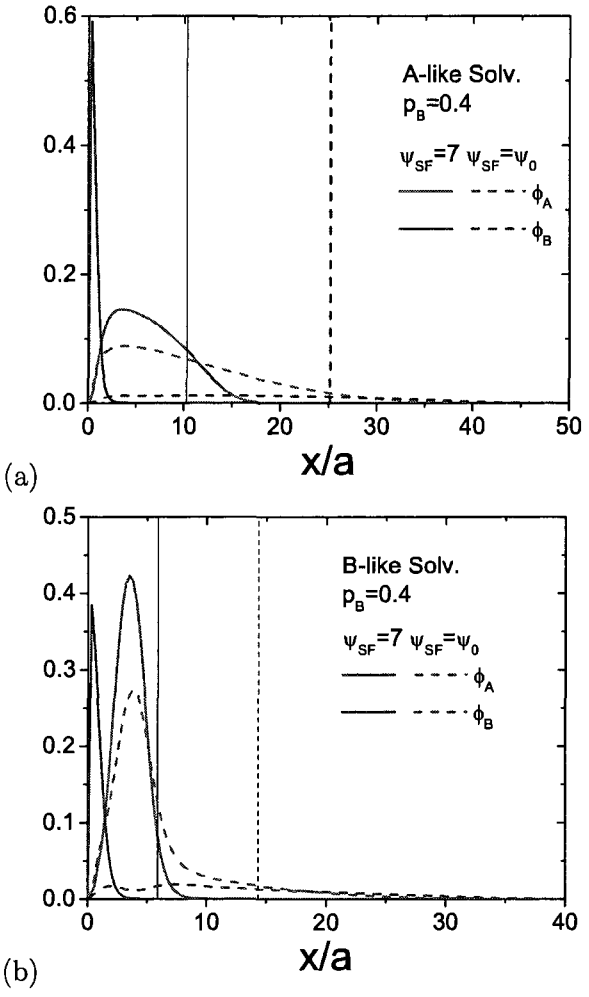

Fig. 7.9: Comparison of segmental density profiles of B-bock charged ($p_B = 0.4$) DBC brushes obtained at neutral surface $\sigma_{SF} = 0$ ($\psi_{SF} = \psi_0$) and positively charged surface $\psi_{SF} = 7$ in (a) A-like solvent condition; (b) B-like solvent condition. The vertical dashed and solid lines in the two plots indicate the position of brush height for $\psi_{SF} = \psi_0$ and $\psi_{SF} = 7$ respectively.

BIBLIOGRAPHY

[1] S. Miklavic and S. J. MarEelja: J. Phys. Chem. **92**, 6718 (1988).

[2] S. Misra, S. Varanasi, and P. P. Varanasi, Macromolecules **22**

[3] P. Pincus, Macromolecules **24**, 2912 (1991).

[4] R. S. Ross and P. Pincus, Macromolecules **25**, 2177 (1992).

[5] O. V. Borisov, T. M. Birshtein, and E. B. Zhulina, J. Phys. II **1**, 521 (1991).

[6] E. B. Zhulina, O. V. Borisov, and T. M. Birshtein, J. Phys. II **2**, 63 (1992).

[7] O. V. Borisov, E. B. Zhulina, and T. M. Birshtein, Macromolecules **27** 4795 (1994).

[8] E. B. Zhulina, O. V. Borisov, and T. M. Birshtein, Macromolecules **28** 521 (1991).

[9] E. B. Zhulina and O. V. Borisov, J. Chem. Phys. **107**, 5952 (1997).

[10] E. B. Zhulina, J. K. Wolterink, and O. V. Borisov, Macromolecules **33**, 4945 (2000).

[11] O. V. Borisov and E. B. Zhulina, J. Phys. II **7**, 449 (1997).

[12] H. Seki, Y. Y. Suzuki and H. Orland, J. Phys. Soc. Jpn. **76**, 104601 (2007).

[13] R. Israels, F. A. M. Leermakers, G. J. Fleer, and E. B. Zhulina, Macromolecules **27** 3249 (1994).

[14] Q. Wang, T. Taniguchi and G. H. Fredrickson, J. Phys. Chem. **108**, 6733 (2004).

[15] E. Helfand and Y. Tagami, J. Chem. Phys. **56**, 3592 (1972).

[16] F. Zhou and T. S. Huck, Phys. Chem. Chem. Phys. **8**, 3815 (2006).

[17] H. Watanabe, S. S. Patel, J. F. Argillier, E. E. Parsonnage, J. W. Mays, N. Dan-Brandon, and M. Tirrell, Mater. Res. Soc. Symp. Proc. **249**, 255 (1992).

[18] C. Amiel, M. Sikka, J. W. Schneider, Y. H. Tsao, M. Tirrell, and J. W. Mays, Macromolecules **28**, 3125 (1995).

[19] P. Guenoun, A. Schlachli, D. Sentenac, J. W. Mays, and J. J. Benattar, Phys. Rev. Lett. **74**, 3628 (1995).

[20] Y. Mir, P. Auroy, and L. Auvray, Phys. Rev. Lett. **75**, 2863 (1995).

[21] H. Ahrens, S. Forster, and C. A. Helm, Macromolecules **30**, 8447, (1997).

[22] H. Ahrens, S. Forster, and C. A. Helm, Phys. Rev. Lett. **81**, 4172 (1998).

[23] R. Hariharan, C. Biver, J. Mays, and W. B. Russel, Macromolecules **31**, 7506 (1998).

[24] R. Hariharan, C. Biver, and W. B. Russel, Macromolecules **31**, 7514, (1998).

[25] M. Biesalski and J. Ruhe, Macromolecules **32**, 2309 (1999).

[26] M. Biesalski, J. Ruhe, and D. Johannsmann, J. Chem. Phys. **111**, 7029 (1999).

[27] Y. Tran, P. Auroy, L.-T. Lee, and M. Stamm, Phys. Rev. E **60**, 6984 (1999).

[28] Y. Tran, P. Auroy, and L.-T. Lee, Macromolecules **32**, 8952 (1999).

[29] Y. Tran and P. Auroy, Eur. Phys. J. E **5**, 65 (2001).

[30] F. Muller, P. Fontaine, M. Delsanti, L. Belloni, J. Yang, Y. J. Chen, J. W. Mays, P. Lesieur, M. Tirrel, and P. Guenoun, Eur. Phys. J. E **6**, 109 (2001).

[31] M. Balastre, F. Li, P. Schorr, J. Yang, J. W. Mays, and M. V. Tirrell, Macromolecules **35**, 9480 (2002).

[32] P. Kaewsaiha, K. Matsumoto, and H. Matsuoka, Langmuir **20**, 6754 (2004).

[33] G. Romet-Lemonne, J. Daillant, J. Guenoun, J. Yang, and J. W. Mays, Phys. Rev. Lett. **93**, 148301 (2004).

[34] H. Ahrens, S. Frster, C. A. Helm, N. A. Kumar, A. Naji, R. R. Netz, and C. Seidel, J. Phys. Chem. B **108**, 16870 (2004).

[35] D. Meng and Q. Wang, J. Chem. Phys. **130**, 134904 (2009).

[36] W. H. Press, S. A. Teukolsky, W. T. Vetterling, and B. P. Flannery, Chap. 4.3 in Numerical Recipes in C: the Art of Scientific Computing, 2nd Ed., Cambridge University Press, 2002.

[37] W. H. Press, S. A. Teukolsky, W. T. Vetterling, and B. P. Flannery, Chap. 9.7 in Numerical Recipes in C: the Art of Scientific Computing, 2nd Ed., Cambridge University Press, 2002.

Part III

PROSPECTIVES

8. CONCLUDING REMARKS AND FUTURE WORK

In this section we will conclude briefly all the studies in this dissertation, and then point out some extensions that can be possibly made based on the current work.

8.1 Diblock Copolymer under Nano-Confinement

Our investigations begin from the simplest case: symmetric diblock copolymer under planner confinement of two homogeneous surfaces. The effects of surface preference and film thickness are both studied. Much richer phase behaviors are observed compared to that in bulk condition where only one dimensional lamellar structure can be formed. In particular, complex three dimensional structures are found under certain surface conditions and their stabilities against other candidate structures are proved. We further extend our study to situations where the confining surfaces are not flat but of geometrical shapes, i.e., elbows formed by two side walls angled to each other. Lamellae formed under such conditions exhibit bend and arc structures. The correlations between the elbow angle and the lamellar tilting angle with respect to the side walls are identified from our calculations and agree well with experimental observations. As to the asymmetric diblock copolymers, we studied the directed assembly of cylinder forming DBC on chemically patterned substrates with pattern stripes preferring the minor block. By adjusting the stripe spacing to be incommensurate with bulk

cylinder periods, the cylinders are observed to be alternately oriented parallel to the surface on preferential stripes and perpendicular to the surface on neutral stripes, constituting a novel complex morphology. Our calculations agree with experiment data and further provide insightful information on the complex three dimensional structures that are otherwise difficult to be completely resolved in experiments.

Besides all these achievements in our efforts to study diblock copolymer under nano-confinement using the self-consistent field theory, some improvements can be made in the following aspects.

Numerical scheme: The crux of SCF calculation is in solving the modified diffusion equation (MDE). In our study, the Fourier transform based schemes have been used in the spacial dimension, which requires a rectangular system volume. In studies of systems on geometrically patterned substrate, for example in Chapter 4, in order to create substrate with elbow patterns we imposed generalized incompressibility conditions at all positions to keep polymers out of the side walls. Such approach is simple to be implemented and in principle can be designed to produce geometrical patterns of any shapes. However, it has some draw backs. First, computational power is wasted since the computation domain includes the polymer depleted regions where solutions are of no interest. Second, the narrow interface between polymer occupied region and polymer depleted region leads to numerical difficulties in converging the self-consistent field equations. In order to solve the two problems polymer depleted region needs to be excluded from the computation domain, possibly leaving the system in a irregular shape. In this situation, the finite element

scheme becomes a ideal choice to be implemented in solving the MDE for its flexibility in dealing with irregular volume and boundary conditions.

Chain structures: All of our studies so far are concerned with flexible polymer chains whose chain energy depends only on the bond length. The SCF calculations can surely be extended to other chain models such as semiflexible, rigid rod, or rigid-coil chains. These models are important because they represent systems that are of practical interests, such as lipids, DNA molecules and liquid crystals. In these situations the chain rigidity also needs to be considered, as the result the modified diffusion equation will have different forms and new numerical methods needs to be developed.

8.2 Smart Surfaces of Polymer Brushes

Polymer brushes can be used to make the so called "smart" surfaces that can exhibit configurational and/or compositional change in response to external stimuli. The second part of this dissertation is devoted to answering the question of what stimuli can be used and how polymer brushes respond to them.

We have first studied one-component brushes, i.e., a homopolymer brushes, the PNIPAM brushes in water solution. Due to the hydrogen bonding of PNIPAM segments with water molecules, the PNIPAM brushes show configurational changes with temperature that can be characterized by the thermal response of brush height. Our SCF calculations show that the temperature at which such thermal response is maximized is determined by the grafting density, while the chain length controls the magnitude of change in brush height. We then

extended our interests to the study of diblock copolymer (DBC) brushes where the grafted polymer chains consists of two chemically distinct blocks (A and B). By setting the solvent selectivity, both configurational and compositional responses can be achieved through solvent treatments. Our studies show that among all the factors that may affect the solvent response of DBC brushes, copolymer composition ($N_A/(N_A + N_B)$)is by far the most important one. There exists a optimum value of copolymer composition at which brush surface layer exhibit largest compositional switching when treated by A-like and B-like solvents successively. Finally, we investigated the stimuli-response of charged DBC brushes. Given the vast parameter space encountered here, we conducted our study based on the uncharged DBC brushes and explored the effects of charge fraction on polymer chains, solution pH and ionic strength, and applied electric fields on the brush surface-switching; the work in this dissertation reveals the complex interplay between different stimuli in such systems. At last two possible extensions from the current work on polymer brushes can be made in the following two aspects.

Mixed homopolymer brushes: Another type of two-component brushes are mixed homopolymer brushes where two types of homopolymer chains are randomly grafted onto substrates at a certain volume fraction. While there have been a few studies on the solvent response of neutral mixed homopolymer brushes, the charged mixed homopolymer brushes are largely left unstudied, which becomes a natural extension of the current work.

Multi-dimensional calculations: All of our studies on polymer brushes so far are through one dimensional calculations where lateral homogeneity is

always assumed. However in situations such as in bad solvent condition, the lateral inhomogeneous structures are usually formed and the surface roughness from this lateral inhomogeneity becomes important in many applications. As importantly, the assumption of lateral homogeneity also limits our ability to study polymer brushes of grafting patterns. To release this lateral homogeneity assumption three dimensional calculations then become necessary to provide us fully resolved brush structures.

LIST OF PUBLICATIONS

1. *S. O. Kim, B. H. Kim, D. Meng, D. O. Shin, C. M. Koo, H. H. Solak, and Q. Wang*, "Novel Complex Nanostructure from Directed Assembly of Block Copolymers on Incommensurate Surface Patterns" **Adv. Mater.**, **19**(20), 3271-3275 (2007)

2. *D. Meng and Q. Wang*, "Hard-Surface Effects in Polymer Self-Consistent Field Calculations" **J. Chem. Phys.**, **126**, 234902 (2007)

3. *D. Meng and Q. Wang*, "Solvent-Response of Diblock Copolymer Brushes" **J. Chem. Phys.**, **130**, 134904 (2009)

4. *D. Meng and Q. Wang*, "Complex Morphologies in Thin Films of Symmetric Diblock Copolymers" Submitted.

5. *D. Meng and Q. Wang*, "Thermal-Response of Poly-NIPAM Brushes in Water" in preparation.

6. *D. Meng and Q. Wang*, "Stimuli-Response of Charged Diblock Copolymer Brushes" in preparation.

7. *S. M. Park, D. Meng, C. T. Rettner, D. S. Dandy, Q. Wang, and H. C. Kim*, "Bending of Lamellar Microdomains of Symmetric Diblock Copolymers on Topologically Nano-Patterned Surfaces" in preparation.